論文 / 著書情報
Article / Book Information

題目(和文)	
Title(English)	Synthesis of novel Li-Co-Mn-O epitaxial thin-film electrode using layer-by-layer deposition process : its structure and electrochemical properties
著者(和文)	LimJaemin
Author(English)	Jaemin Lim
出典(和文)	学位:博士（理学）, 学位授与機関:東京工業大学, 報告番号:甲第9735号, 授与年月日:2015年3月26日, 学位の種別:課程博士, 審査員:菅野　了次,大坂　武男,川路　均,中村　二朗,平山　雅章
Citation(English)	Degree:, Conferring organization: Tokyo Institute of Technology, Report number:甲第9735号, Conferred date:2015/3/26, Degree Type:Course doctor, Examiner:,,,,
学位種別(和文)	博士論文
Type(English)	Doctoral Thesis

Synthesis of novel Li-Co-Mn-O epitaxial thin-film electrode using layer-by-layer deposition process : its structure and electrochemical properties

by

Jaemin Lim

A dissertation submitted to Tokyo Institute of Technology in accordance with
the requirements for the degree of doctor of science

Department of Electronic Chemistry
Interdisciplinary Graduate School of Science and Engineering
Tokyo Institute of Technology

January 2015

Acknowledgements

First and foremost, praise and thank to God, the Almighty, for being my strength and the Good Shepherd in the writing of this thesis. Without Him, I would not have had the wisdom or the physical ability to do so.

My deepest gratitude goes to thesis advisor Prof. Ryoji Kanno for his considerate guidance, motivation and valuable discussion on this thesis. His vision and enthusiasm have been inspiring and kept me going through the ups and downs of research. I express sincere gratitude to Associate Prof. Masaaki Hirayama, for his guidance, support and valuable discussion. I also would like to thank Prof. Takeo Ohsaka, Prof. Hitoshi Kawaji and Prof. Jiro Nakamura for their important contributions to this thesis and the development of my scientific approach with serious review and valuable discussion.

I wish to thank Junior Associate Prof. Kota Suzuki for devoting much time to valuable discussion and support at various stages of this research.

I am grateful to Dr. Jin-Young Son of Japan Synchrotron Radiation Research Institute for helping Hard X-ray Photoelectron Spectroscopy measurements at SPring-8 and considerate discussion. I would like to show great appreciation to Prof. Kunio Takayanagi, Dr. Soyeon Lee of Tokyo Institute of Technology and Prof. Yoshifumi Oshima of Japan Advanced Institute of Science and Technology for helping Scanning Transmission Electron Microscopy observation and instructive discussion.

Throughout PhD, I had the privilege of researching with excellent and kind members. I wish to make sincere gratitude to all the former and present members of Kanno-Hirayama laboratory for their kind support and discussion. A special thank to all the thin film group members, especially Dr. Kyungsu Kim, Dr. Sou Taminato, Dr. Sangryun Kim, Dr. Yueming Zheng, Hidenori Fujita, Takeshi Kobayashi and Ryo Yamaguchi.

I am truly thankful to Sehoon Jeong, Hyunbo Shim and Joonho Bang for being good friend and counselor during the long and hard PhD journey. Wish them all the best in their future endeavors. Many thank to my long-time friends, Joonhee Han, Sung-In Seo and Kyunghee Lee, for their continued support and friendship. I would like to appreciate to my girl friend Yujeong Choi, for her continued encouragement and love.

I would like to express my deepest gratitude to Epson International Scholarship Foundation for their financial support during the PhD.

This study was supported in part by a Grant-in-Aid for Scientific Research on Innovative Areas “Exploration of nanostructure-property relationships for materials innovation” (No. 25106009) and Grant-in-Aid for scientific Research (A) (No. 25248051) from the Japan Society for the Promotion of Science. The synchrotron radiation experiments were carried out as projects approved by the Japan Synchrotron Radiation Research Institute (JASRI) (Proposal No. 2014A1801).

Finally, I would like to express sincere gratitude to my parent, Mr. Chul-Soo Lim and Mrs. Myung-Ok Moon, and my brother Mr. Jaehyung Lim, for their support, understanding, dedication and encouragement.

January 2015
Jaemin Lim

Table of Contents

This chapter contains contents of the below article published in Journal of Power Sources.

Synthesis, structure and electrochemical properties of novel Li-Co-Mn-O epitaxial thin-film electrode using layer-by-layer deposition process, *Journal of Power Sources*, **279**, 502-509 (2015)
Jaemin Lim, Soyeon Lee, Kota Suzuki, KyungSu Kim, Sangryun Kim, Sou Taminato, Masaaki Hirayama, Yoshifumi Oshima, Kunio Takayanagi, and Ryoji Kanno

List of Tables

List of Figures and Illustrations

Chapter 1: Introduction

1.1 Lithium batteries

Batteries have an ability of converting the stored chemical energy directly into the electrical energy and are applied to various electrical devices. The batteries are systematically divided into two categories in accordance with their reversibility. One is primary battery that provides one-way energy convergence from the chemical to electrical energy. The other is secondary battery that has ability to restore the chemical energy by the electrochemical charging. Among various types of the secondary batteries, lithium batteries have been widely used as power sources for portable devices such as a mobile phone, a laptop computer and music players due to their high energy and power densities [1, 2]. Recently, the lithium batteries are expected to be a possible candidate as energy storage system of electric vehicles (EV) and plug in hybrid electric vehicles (PHEV) with replacing the internal combustion engine [3]. However, there are still further requirements to improve the characteristics such as power, energy density, safety, reliability and rate capability [4].

A history of the lithium rechargeable battery began from a report of Whittingam in 1976; electrochemical Li (de)intercalation phenomena of TiS_2 was discovered [5]. The initial lithium battery consisted of TiS_2 layered chalcogenides as the cathode, Li metal as the anode and lithium perchlorate ($LiClO_4$) in dioxolane as electrolyte. However, the invented battery were not launched into the market due to serious problems including dendritic growth of Li at the anode during charge-discharge process and low energy density owing to its low operation voltage. Therefore, a lot of researches to find solutions for the problems were continuously carried out. In 1980s, Yazami *et al.* and Kanno *et al.* reported carbonaceous materials that provide highly reversible (de)intercalation of Li at the anode [6, 7]. This new anode became a fascinating suggestion to prevent the formation of Li dendrites. Accordingly, the lithium battery was developed in ways that use intercalation materials as both in anode and cathode sides. Since then, Goodenough *et al.* demonstrated a cathode family: $\mathrm{Li}M\mathrm{O_2}$ (M = Mn, Co, Ni) with a layered rock salt structure, which enables stable Li (de)intercalation with resulting in a high redox potential (*ca.* 4.0 V) [8-10]. The proposed cathode materials provided much more enhanced energy density comparing to that of chalcogenides. On the basis of these researches that achieved a breakthrough, the first commercialized lithium ion battery was released by Sony Corporation in 1991 [11].

1.2 Principles of lithium batteries

Figure 1.1 depicts intercalation reaction of a conventional lithium ion rechargeable battery during charge-discharge process. $LiCoO_2$ and graphite are used as the cathode and anode materials, respectively. Electrolyte solutions consisting of an organic solvent such as ethylene carbonate (EC), diethyl carbonate (DEC), dimethyl carbonate (DMC) and propylene carbonate (PC) with lithium salt such as $LiPF_6$ and $LiClO_4$, are applied to support the lithium transportation in the lithium battery. A porous polymeric material is inserted as a separator to prevent direct contact between the two electrodes, which causes an internal short circuit.

The details of charge and discharge reactions can be illustrated as follows;

Positive electrode : $\mathrm{LiCoO_2} \rightleftarrows x\mathrm{Li}^+ + x\mathrm{e}^- + \mathrm{Li}_{1-x}\mathrm{CoO_2}$

Negative electrode : $x\mathrm{Li}^+ + x\mathrm{e}^- + \mathrm{C} \rightleftarrows \mathrm{Li}_x\mathrm{C}$

Overall reaction : $\mathrm{LiCoO_2} + \mathrm{C} \rightleftarrows \mathrm{Li}_{1-x}\mathrm{CoO_2} + \mathrm{Li}_x\mathrm{C}$

In charge process, lithium ions are extracted from a host lattice of cathode material and transported to an anode material through an organic electrolyte. Then, lithium ions are inserted into a host lattice of anode material, in which released electrons are migrated from the cathode to anode materials through external circuit. During discharge process, a reverse reaction happens; the lithium ions are extracted from the anode and inserted into the lattice of cathode material. The electrolyte that supports the lithium diffusion between two electrodes during intercalation reaction is ideally a perfect insulator. Moreover, a solid electrolyte interface (SEI) layer, which is formed by oxidation and/or reduction of organic solvent, also plays a significant role in maintain a stability of lithium battery [12, 13]. Once a stable SEI layer is created, spontaneous oxidation and reduction of the organic electrolyte are restricted. For these reason, the intercalation reaction is highly reversible and guarantees long life of lithium batteries.

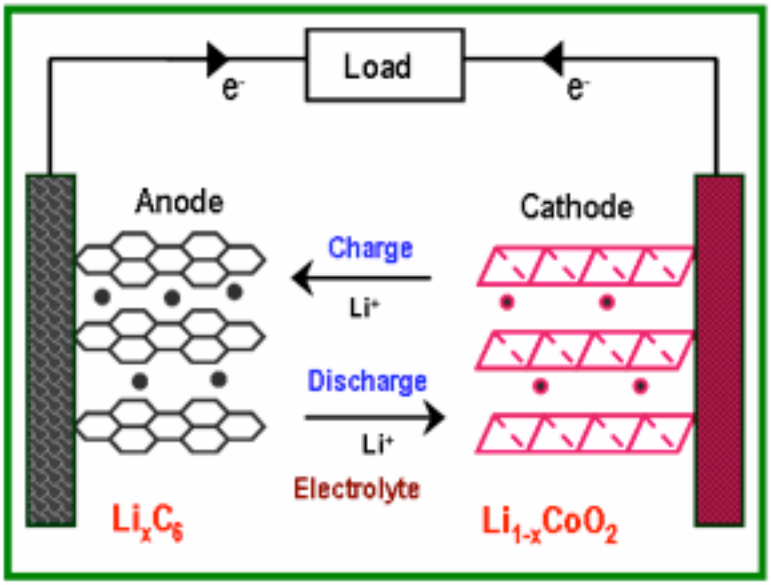

Figure 1.1 Schematic representation and operating principles of rechargeable lithium battery.

1.3 Electrode materials

Electrode materials occupying largest portion in the battery system directly determines the theoretical maximal abilities of the lithium rechargeable battery although the optimized performance could be achieved by cell design and constructions. The capacity and reaction voltage of the battery are related to the electrochemical capacity and Gibbs free energy of each material, respectively. This fact indicates that innovation of electrode materials is necessary to develop next generation battery system. Figure 1.2 displays the operation voltage and capacity of the cathode and anode materials, which are used and researched currently [14]. To obtain the high performance battery with large energy density, a combination of a cathode with high potential and an anode with low potential is demanded. In addition, the large capacity also should be regarded as significant factor for the combination. The anode materials, especially carbon and lithium metal, show low operation voltages near to 0 V (*vs.* Li/Li^+) and high capacity of 650 and 3800 mAh g^{-1}, respectively. However, there are no noticeable cathode materials showing high potential and large capacity in comparison with those of anode materials. In particular, the small capacity of a cathode material is a significant issue to be solved. Accordingly, much larger amount of the cathode material than that of the anode material is required to secure the large capacity, which results low energy density per unit weight and disproportionate packing of the cathode and anode in battery cells. Therefore, a novel cathode material with large capacity and high operation voltage is required to achieve high energy density of lithium batteries. Moreover, recent tremendous interests in PHEV and EV call on various characteristics such as high rate capability, stability, reliability, long life time and low cost, as well as the large capacity. In the following part, structural and electrochemical properties of several representative intercalation compounds are reviewed.

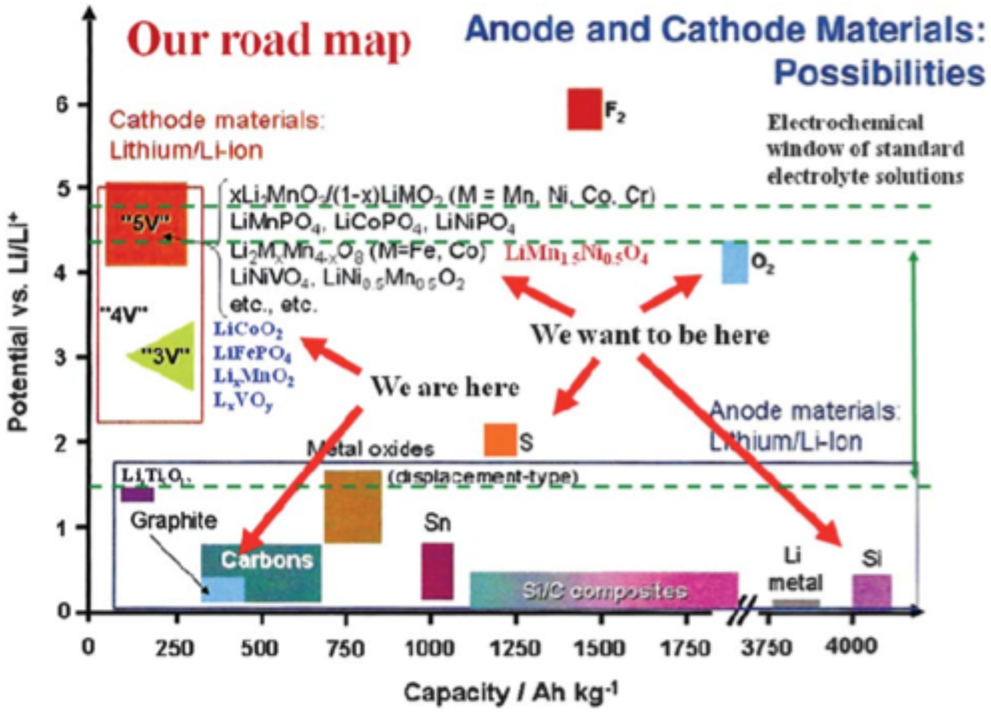

Figure 1.2 A review of advanced and practical lithium battery materials [14].

1.3.1 Layered rock salt type $LiMO_2$ (M = transition metal)

The first layered rock salt type oxides that could be intercalated with lithium is $LiCoO_2$ reported in 1980s by Goodenough *et al.* [8]. Owing to its high redox potential (*ca.* 3.9 V *vs.* Li/Li^+), good cyclability, easy handling and synthesis, $LiCoO_2$ is widely used in present since it was applied to the cathode of the first commercialized rocking chair type lithium battery. In spite of a large theoretical capacity of *ca.* 274 mAh g^{-1}, only a half of the capacity is reversible and available in a practical rechargeable battery. This is because $LiCoO_2$ gives rise to phase transition from hexagonal to monoclinic when an amount of extracted lithium exceeds 0.5 [15-17]. In this process, $LiCoO_2$ shows significant structural instability in which oxidation and decomposition of electrolyte takes place with dissolution of cobalt ion from the interface between electrode and electrolyte. As a result, a serious capacity fading occurs.

Figure 1.3 depicts a structure diagram of $LiCoO_2$ with layered rock salt type structure (space group: R-3m) of rhombohedral symmetry. Examining the structure closely, cobalt and lithium respective occupy 3a and 3b sites with octahedral coordination and oxygen forms cubic closed packing (ccp) layer. Then, the cobalt and lithium layers are alternately stacked up along [111] direction, which results in two-dimensional plane. In the layered rock salt type structure, transition metal layer is composed of edge sharing of MO_6 octahedra and lithium layer (LiO_6) is located on the transition metal slab. The lithium is expected to diffuse from and into the lithium layer through an interstitial tetrahedral site (6c) forming plane sharing with MO_6 octahedra [16]. The layered rock salt type structure generally has higher lithium ion diffusion coefficient than that of the other structures, spinel and olivine, due to the two-dimension planar lithium diffusion pathway composed of only lithium layer. Despite of these advantages, several issues for drawback of $LiCoO_2$, structural instability at high potential, high toxicity, high cost and scarcity, have restrained an application of $LiCoO_2$ for large-scale storage system. Hence, a lot of studies to resolve the problems also have been performed. Substitution of Co by other cations and/or solid solution formation with other $LiMO_2$ phase systems such as $LiNiO_2$ [18], $LiNi_xCo_{1-x}O_2$ [19] and $Li(Ni, Co, Mn)O_2$ [20] systems are actively researched.

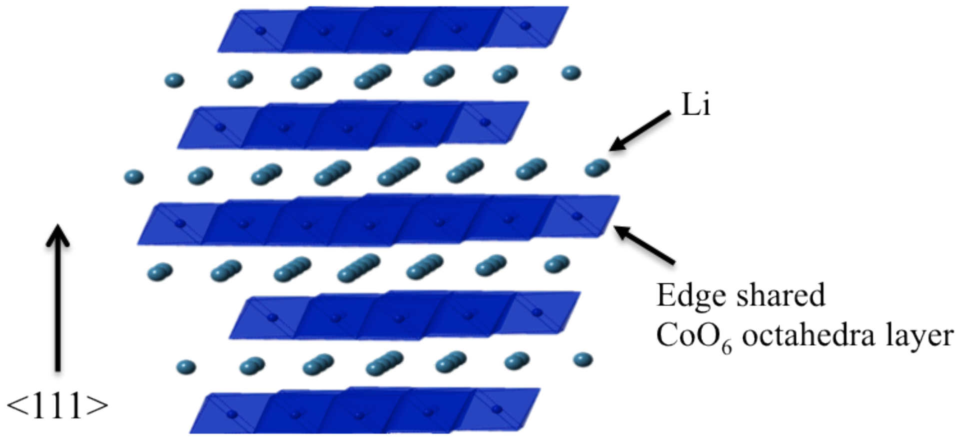

Figure 1.3 Crystal structure of $LiCoO_2$ with layered rock salt type structure.

1.3.2 Spinel type LiM_2O_4 (M = transition metal)

$LiMn_2O_4$ that has attracted a lot of attention as one of the most promising alternative cathode material is a representative material of a cubic spinel type structure (space group: *Fd*-3*m*) [21]. The $LiMn_2O_4$ shows a high operation voltage of *ca.* 4 V (*vs.* Li/Li^+) and good thermal stability with 148 mAh g^{-1} of theoretical capacity in a specific range ($0 < x < 1$ in $Li_xMn_2O_4$) [22]. In addition, it is known that intercalation reaction is also possible at *ca.* 3 V region ($0 < y < 1$ in $Li_{1+y}Mn_2O_4$). Therefore, a high discharge capacity of 250 mAh g^{-1} could be obtained by utilizing both reactions in a voltage range between 3 and 4 V. However, the spinel type $LiMn_2O_4$ is transformed to $Li_2Mn_2O_4$ of tetragonal structure in the 3 V region accompanying a large scale of volume expansion (*ca.* 6 %). The volume expansion gives rises to structural degradation with reducing a cycle retention property [23]. As a result, charge-discharge of $LiMn_2O_4$ is performed only in the 4 V region.

Figure 1.4(a) shows crystal structure diagram of $LiMn_2O_4$ indicating relative positions of lithium and manganese atoms. The lithium is located at tetrahedral (8*a*) site and the manganese occupies octahedral (16*d*) site. Oxygen positioned on 32*e* site is forming cubic closed packing (ccp). Figure 1.4(b) illustrates a diffusion pathway of lithium ion in the spinel type structure. Lithium (8*a*) migrates in three-dimensions through an interstitial tetrahedral site (16*c*) which forms face sharing with octahedral 16*d* site in the Mn_2O_4 framework. In the spinel structure, MO_6 octahedra organizes consecutive three-dimensional cubic array with sharing its edge, which provides structural intensity to the Mn_2O_4 framework. The charge process of spinel $LiMn_2O_4$ is described as two step reaction divided into single-phase and two-phase reactions [23];

$LiMn_2O_4 \rightarrow Li_{1-x}Mn_2O_4 + xLi^+ + xe^-$ $(0 < x < 0.5)$

$Li_{0.5}Mn_2O_4 \rightarrow Li_{0.5-y}Mn_2O_4 + y\lambda\text{-}MnO_2 + yLi^+ + ye^-$ $(0 < y < 0.5)$

The most fatal problem of the $LiMn_2O_4$ is capacity fading during the charge-discharge process, though the charge-discharge is carried out at the 4 V region ($0 < x < 1$ in $Li_xMn_2O_4$). In particular, the capacity fading is obviously severe at high temperature [24-26]. The main reasons for capacity fading are known as structural instability and dissolution of manganese ion into organic electrolyte, which are caused by tri-valent Mn ion [27-29]. The tri-valent manganese ion causes Jahn-Teller distortion of MnO_6 octahedron in $LiMn_2O_4$ and decomposition with disproportional reaction; $2Mn^{3+} \rightarrow Mn^{4+} + Mn^{2+}$ [30]. Therefore, a lot of researches in terms of eliminating the Jahn-Teller effect and enhancing the cycle retention property have been advanced by means of substituting partial Mn^{3+} to various different transition metals [31-38]. Nevertheless, further researches are required to solve a problem of capacity reduction, which is caused by the substitution of electrochemically inert materials.

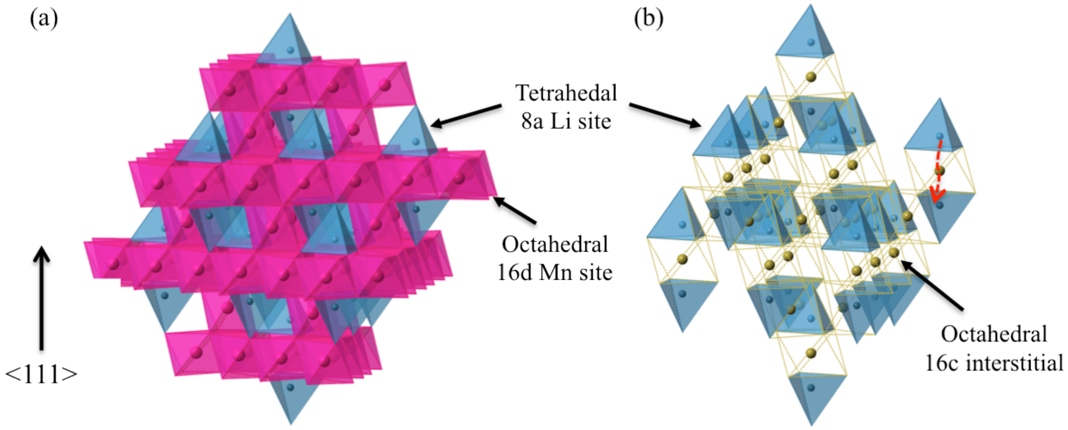

Figure 1.4 (a) Crystal structures of $LiMn_2O_4$ with spinel type structure and (b) lithium diffusion pathway from 8*a* to 8*a* through interstitial 16*c* site.

1.4 New concept to develop electrode materials

1.4.1 Limitation of conventional synthesis method

As described in previous content, development of a novel electrode material with new characteristics have been required urgently. In the developing of electrode materials, significant parameters to be considered are crystal structure and chemical composition, which directly affect electrochemical characteristics of the electrode. This is because three critical phenomena take place with charge-discharge reactions for most of electrode materials, which are closely related to their crystal structure and composition.

First, the charge-discharge reaction of lithium battery is regarded as (de)intercalation process of lithium. The (de)intercalation process indicates the diffusion process of lithium along a diffusion path way, which entirely relies on the crystal structures and compositions of electrode materials [39-48]. Figure 1.5 shows three different intercalation compounds with different composition and crystal structure. Red lines indicate lithium diffusion pathways in each material, and it can be clearly seen that lithium migrates different manner in the crystal structure especially in diffusion dimensional aspect. The different diffusion pathways are attributed to the crystal structures. The crystal structure forms a framework and determines diffusion direction of lithium. When a crystal structure is determined, the composition is considered as a critical component to influence on the intercalation process. The lithium diffusion process is described as a hopping from a site to an adjacent site through a space surrounded by ions, which is so-called a bottle-neck. Therefore, a size of the bottle-neck has largely effect on the diffusion speed. The composition controls the bottle-neck size and consequently affects the lithium diffusivity in the structure.

Second, a phase transition of the crystal structure is shown during charge-discharge reactions. The phase transition is an important phenomenon since its reversibility could affect stabilities of electrochemical reactions. The phase transition entirely depends on crystal structures because the phenomenon occurs due to changing of lithium amount in the structure. For example, the spinel structure transforms from cubic to tetragonal structure when amount of lithium exceeds 1.0. However, the layered rock salt structure shows a phase transition from hexagonal to orthorhombic structure. The variation of amount of lithium changes electrical forces between atoms occupying crystallographic sites in frameworks then it results in the phase transition. Therefore, it can be considered that the phase transition is attributed to crystal structures [33, 45, 49-51].

At last, redox of transition metals in the electrode material proceeds during charge discharge reactions. The oxidation and reduction of the transition metals determines a redox potential of electrochemical reactions. The redox potential largely depends on a kind and oxidation states of transition metals, since the potentials are affected from a relation between a redox energy of the transition metals and Fermi level of anode materials. That is, a composition and an oxidation state of the transition metal, contributing to the electrochemical reaction, controls the reaction voltages. Therefore, layered rock salt, olivine and spinel structure having different compositions and oxidation states of transition metals reveal different reaction voltages. Furthermore, the variation of redox potentials in accordance with compositions can be elucidated by inductive effect. The inductive effect indicates an charge transmission effect through a chain of atoms in a molecule, resulting in a permanent dipole in a bond. For a $Li_xFe(MO_4)$ (M = P, Mo, W, S etc.) with olivine structure, the counter cation, which shares a common oxygen nearest neighbor with Fe in an Fe-O-M linkage, determines the strength of the Fe-O covalency through the inductive effect, then the strength of the Fe-O bonding influences on the reaction voltages [52-58].

For these reasons, the development of new electrode materials has been performed with focusing on exploration of novel crystal structures and compositions. Therefore, a variety of synthesis techniques such as solid-state reaction, sol-gel method, hydrothermal and co-precipitation methods have been applied to control the crystal structures and compositions of the electrode materials [50, 56, 59-64]. However, conventional synthesis methods have a significant limitation for designing the crystal structure and selecting the composition because these factors are strongly dominated by Gibbs phase rule, which depends on the ionic radius of the constituent elements and thermodynamic stability of the structure. The phase rule is given by the equation; $P + F = C + 2$, where P is the number of phases in equilibrium, C is the number of constituent element and F is the number of degrees of freedom or intrinsic variables. The relationship between phase and component clearly explains the limitation in number of structures and compositions. Furthermore, this rule reveals that the characteristics of electrode materials are also restricted. Therefore, a new technique, which provide exceptional structure and composition into the electrode materials are necessary to develop new electrode materials.

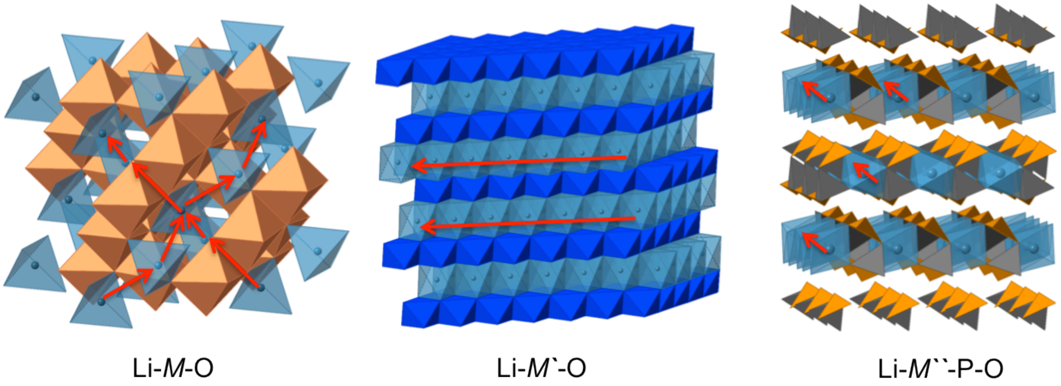

Figure 1.5 Intercalation compounds with different composition and crystal structure. The red lines indicate lithium diffusion pathways.

To obtain novel structures and phases that can not be realized by the conventional methods, metastable phases are also need to be considered with avoiding general stable phases. The metastable phases require different synthesis environments such as high temperature, quenching process, nano-scale particle and high level of vacuum. For the novel structures, a super-lattice structure should be considered. New structures and phases never have been existed can be obtained by forming the artificial super-lattice using several conventional structures. A thin film deposition is a most ideal approach to satisfy the both concepts metastable phase and super-lattice structure.

1.4.2 Layer-by-layer deposition process

A new concept of layer-by-layer deposition that staking layers one by one was applied to the lithium battery electrode for obtaining novel crystal structures and compositions.

1.4.2.1 Inspiration for layer-by-layer deposition process

An inspiration of layer-by-layer deposition was originated from crystal structure of β-Al_2O_3. The β-Al_2O_3 is the representative name for the family expressed with general formula of $M_2O \cdot nX_2O_3$, where the n is between 5 and 11, the M and X are monovalent and trivalent cations, respectively. Among them, the most representative member is sodium β-Al_2O_3 (M = Na^+, X = Al^{3+}). The β-Al_2O_3 began to attract interest as a solid state ion conductor with a significant discovery that the Na ion of β-Al_2O_3 is greatly mobile at and above room temperature. Accordingly, a conduction mechanism was researched with structural analysis of the β-Al_2O_3 structure. Figure 1.6 displays the crystal structure of β-Al_2O_3 where Na_2O is doped. The β-Al_2O_3 is formed with three-dimensional stacking of cubic packing of oxygen ion, where every fifth packing layer has three quarters of oxygen missing. The Na ion, which has smaller ion radius than oxygen ion, could migrate along the site where oxygen ion is lost. That we have paid attention is the stacking order and structure of β-Al_2O_3. The conductivity of the β-Al_2O_3 entirely relies on the characteristics of crystal structure that the fifth closed packing layer losses the oxygen ion. Based on the perspective, it would be possible to give an ionic conductivity for a material with no ion conduction by inserting the oxygen lost layer artificially. In a word, novel structures, regularities and compositions could be obtained by building up the layers one by one artificially. Novel characteristics are expected from the combination of the layers with different structures and compositions.

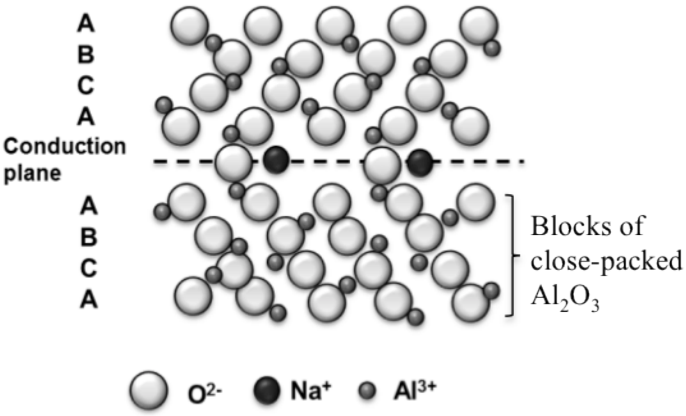

Figure 1.6 Crystal structure of β-Al_2O_3 with Na_2O doped.

1.4.2.2 Application for developing electrode materials

Along with the kind of development, the new technique was applied to develop a new lithium ion battery electrode using layer-by-layer deposition by pulsed laser deposition (PLD) [65, 66]. As depicted in figure 1.7, several materials with different crystal structure and/or composition are continuously stacked on single crystal substrate. Regarding each material as one basic block, complex crystal structure and/or composition could be obtained by depositing several blocks of different materials with various deposition ways. There have been a number of studies on magnetic, dielectric and super conducting materials; the various deposition routs provided a formation of new structures such as super-lattice, gradation and metastable structures, and those properties were drastically changed or unexpected from the mother materials characteristics [66-74]. The diversity of deposition methods of the layer-by-layer deposition such as repeating number, thickness of each layer and combinations of materials is attractive and promising to develop new electrode materials with new properties for lithium batteries. In a word, a variety of new materials could be designed using conventional electrodes materials.

In this study, layer-by-layer process was carried out with PLD on $SrTiO_3(111)$ substrates using two of representative electrode materials: $LiCoO_2$ with a layered rock-salt structure, and $LiMn_2O_4$ with a cubic spinel structure. In order to compare the structure and electrochemical performance, a single-step Li-Co-Mn-O film and a $LiMn_2O_4$ film were also synthesized. The crystal structure, electronic structure, cation distribution and charge-discharge characteristics of the different films were investigated using X-ray diffraction (XRD), X-ray absorption spectroscopy (XAS), high resolution scanning transmission electron microscope (HR-STEM) and electrochemical measurements.

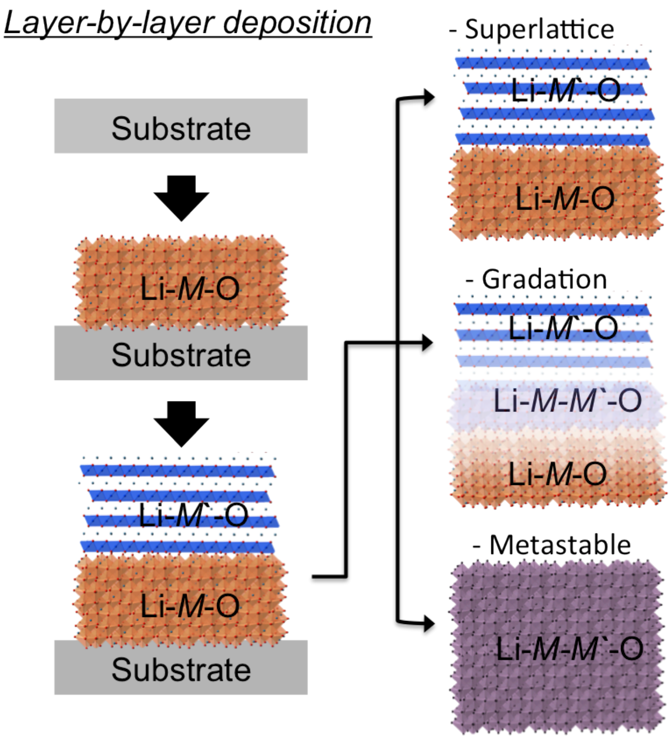

Figure 1.7 Illustration of layer-by-layer deposition process.

1.5 Epitaxial thin film electrode

In previous studies, a series of epitaxial thin films for electrodes and solid electrolytes was synthesized by PLD. These films were used to investigate reactions at the interface between an electrode and a liquid electrolyte, nanoscale effects, anisotropic lithium diffusion in the crystal structure and surface coating effects [30, 45, 46, 75-80]. In this study, the epitaxial thin films are selected to perform layer-by-layer deposition with PLD. This research aims to develop a novel electrode material with new crystal structures and compositions. The epitaxial thin film is an exceptional suggestion for the purpose.

(1) Layer-by-layer deposition technique with epitaxial thin films minimizes the formation of interface among layers and effects of morphology and impurities, which could provide a new structure with long-range order [81, 82].

(2) A top layer stacked onto a bottom is influenced prominently by a crystal structure and orientation that the bottom layer has [83]. The crystal orientation of the bottom epitaxial thin film can be easily controlled with varying the substrate and synthesis conditions. This influence of bottom layer could provide a various formation of top layer with unexpected and distorted new structures.

(3) Further, it is believed that the epitaxial thin film becomes a unique item to investigate critical phenomena of the developed electrode materials: a structural variation during charge-discharge process, a formation of interface phase, lithium diffusion mechanism in the crystal structure, reactions at the interface and their effects on electrochemical characteristics of the electrode material [45].

A final step of this study is that directly designing the new crystal structures by stacking atomic scale layers one by one. Herein, as a first step of the study, nanoscale epitaxial thin films were utilized and stacked up to reveal effects of the layer-by-layer deposition on the structural and electrochemical characteristics. Generally, it is necessary to consider nanoscale effect in various ways to deal with nanoscale thin films. Many researches have been revealed the nanoscale effects on capacities, cycle retention properties and structural stabilities of electrode materials. Reduced diffusion pathway of nanoscaled electrode materials provided fast lithium migrations and high electric conductivities but several serious problems such as decrease of structural stability and cycle retention property were also reported, which are attributed to high portion of surface region and high reactivity of nanoscale electrode materials [61].

However, there are a lot of component that should be considered in the epitaxial thin film electrode except the electrode material. Those are electric current collector with thin film type, substrate and Au current collector. Although these components occupy a large portion in battery, researches have not been performed in respect to effects of the components on battery performances. Since the epitaxial thin films have ideal flat surface with two-dimensional structure, the films have a higher surface energy and reactivity. Furthermore, a behavior of nanoscale materials is completely different with that of bulk materials. Therefore, the components that contact with epitaxial thin film electrode would give electrochemical influences to electrode materials although the electric conductor, substrate and gold current collector are electrochemically in-active materials. In this study, electrochemical characteristics of the components in the epitaxial thin film electrode are investigated to clarify the electrochemical performance of the new electrode material, synthesized by layer-by-layer deposition.

1.6 Purpose of this study

The purpose of this study is to develop novel electrode materials using the new technique of layer-by-layer deposition and to investigate its structural and electrochemical characteristics.

In this study, a novel electrode material is synthesized using layer-by-layer process. The novel electrode material could have unique structure and electrochemical properties, thus electrochemical characterization in wide voltage range is necessary to evaluate the novel electrode. However, electrochemical properties of the current collectors and substrate, consisting of epitaxial thin film electrode, are still unclear for a low voltage region. In order to clearly observe electrochemical characteristics of the only electrode material, electrochemical properties of the constituent components are investigated by charge-discharge and cyclic voltammetry measurements.

Amount of phase, structure and composition that could be obtained with conventional synthesis methods are obviously restrained. On the other hand, the new synthesis technique of the layer-by-layer deposition enables to design numerous electrode materials with novel structures and electrochemical characteristics. A unique structural characteristic of the Li-Co-Mn-O thin film electrode synthesized by layer-by-layer deposition is investigated and confirmed by thin film X-ray diffraction and high resolution scanning transmission microscopy. Electrochemical performances and reaction mechanisms of the new Li-Co-Mn-O thin film electrode are researched and compared with those of Li-Co-Mn-O thin film electrode prepared by a conventional deposition method. Relationship between the unique structure and electrochemical characteristics of the synthesized thin film electrode is discussed.

These results reveal the layer-by-layer deposition technique can be an exceptional alternative to design novel electrode materials with new structures and electrochemical characteristics for development of the next generation lithium battery.

References

[1] J.M. Tarascon, M. Armand, Nature, 414 (2001) 359-367.

[2] A.S. Arico, P. Bruce, B. Scrosati, J.M. Tarascon, W. Van Schalkwijk, Nat Mater, 4 (2005) 366-377.

[3] D. Tang, Y. Sun, Z. Yang, L. Ben, L. Gu, X. Huang, Chem Mater, 26 (2014) 3535-3543.

[4] N.S. Choi, Z.H. Chen, S.A. Freunberger, X.L. Ji, Y.K. Sun, K. Amine, G. Yushin, L.F. Nazar, J. Cho, P.G. Bruce, Angew Chem Int Edit, 51 (2012) 9994-10024.

[5] M.S. Whittingham, Science, 192 (1976) 1126-1127.

[6] R. Yazami, P. Touzain, J Power Sources, 9 (1983) 365-371.

[7] R. Kanno, Y. Takeda, T. Ichikawa, K. Nakanishi, O. Yamamoto, J Power Sources, 26 (1989) 535-543.

[8] K. Mizushima, P.C. Jones, P.J. Wiseman, J.B. Goodenough, Mater Res Bull, 15 (1980) 783-789.

[9] M.M. Thackeray, W.I.F. David, P.G. Bruce, J.B. Goodenough, Mater Res Bull, 18 (1983) 461-472.

[10] A.R. Armstrong, P.G. Bruce, Nature, 381 (1996) 499-500.

[11] T. Nagaura, M. Tozawa, Progress in Batteries and Solar Cells, 1990.

[12] K. Edstrom, T. Gustafsson, J.O. Thomas, Electrochim Acta, 50 (2004) 397-403.

[13] P. Lu, S.J. Harris, Electrochem Commun, 13 (2011) 1035-1037.

[14] R. Marom, S.F. Amalraj, N. Leifer, D. Jacob, D. Aurbach, J Mater Chem, 21 (2011) 9938-9954.

[15] Z.H. Chen, Z.H. Lu, J.R. Dahn, J Electrochem Soc, 149 (2002) A1604-A1609.

[16] A. Van der Ven, M.K. Aydinol, G. Ceder, G. Kresse, J. Hafner, Phys Rev B, 58 (1998) 2975-2987.

[17] T. Ohzuku, A. Ueda, J Electrochem Soc, 141 (1994) 2972-2977.

[18] T. Ohzuku, A. Ueda, M. Nagayama, J Electrochem Soc, 140 (1993) 1862-1870.

[19] A.W. Moses, H.G.G. Flores, J.-G. Kim, M.A. Langell, Applied Surface Science, 253 (2007) 4782-4791.

[20] K.M. Shaju, G.V.S. Rao, B.V.R. Chowdari, Electrochim Acta, 48 (2002) 145-151.

[21] J.M. Tarascon, W.R. Mckinnon, F. Coowar, T.N. Bowmer, G. Amatucci, D. Guyomard, J Electrochem Soc, 141 (1994) 1421-1431.

[22] M.Y. Saidi, J. Barker, R. Koksbang, Electrochim Acta, 41 (1996) 199-204.

[23] M.M. Thackeray, M.F. Mansuetto, J.B. Bates, J Power Sources, 68 (1997) 153-158.

[24] M.J. Lee, S. Lee, P. Oh, Y. Kim, J. Cho, Nano letters, 14 (2014) 993-999.

[25] J. Cho, G.B. Kim, H.S. Lim, C.S. Kim, S.I. Yoo, Electrochem Solid St, 2 (1999) 607-609.

[26] S.H. Ma, H. Noguchi, M. Yoshio, J Power Sources, 97-8 (2001) 385-388.

[27] J.M. Tarascon, E. Wang, F.K. Shokoohi, W.R. Mckinnon, S. Colson, J Electrochem Soc, 138 (1991) 2859-2864.

[28] H. Yamaguchi, A. Yamada, H. Uwe, Phys Rev B, 58 (1998) 8-11.

[29] R.J. Gummow, A. Dekock, M.M. Thackeray, Solid State Ionics, 69 (1994) 59-67.

[30] M. Hirayama, N. Sonoyama, M. Ito, M. Minoura, D. Mori, A. Yamada, K. Tamura, J. Mizuki, R. Kanno, J Electrochem Soc, 154 (2007) A1065-A1072.

[31] H. Kawai, M. Nagata, H. Tukamoto, A.R. West, Electrochem Solid St, 1 (1998) 212-214.

[32] P. Aitchison, B. Ammundsen, D.J. Jones, G. Burns, J. Roziere, J Mater Chem, 9 (1999) 3125-3130.

[33] H. Shigemura, M. Tabuchi, H. Kobayashi, H. Sakaebe, A. Hirano, H. Kageyama, J Mater Chem, 12 (2002) 1882-1891.

[34] K.M. Shaju, G.V.S. Rao, B.V.R. Chowdari, J Mater Chem, 13 (2003) 106-113.

[35] K.M. Shaju, G.V.S. Rao, B.V.R. Chowdari, Solid State Ionics, 148 (2002) 343-350.

[36] M.V. Reddy, S.S. Manoharan, J. John, B. Singh, G.V.S. Rao, B.V.R. Chowdari, J Electrochem Soc, 156 (2009) A652-A660.

[37] R. Chen, M. Knapp, M. Yavuz, R. Heinzmann, D. Wang, S. Ren, V. Trouillet, S. Lebedkin, S. Doyle, H. Hahn, H. Ehrenberg, S. Indris, The Journal of Physical Chemistry C, 118 (2014) 12608-12616.

[38] K.R. Ragavendran, L. Lu, B.J. Hwang, K. Bärner, A. Veluchamy, The Journal of Physical Chemistry C, 117 (2013) 3812-3817.

[39] K. Sakamoto, M. Hirayama, H. Konishi, N. Sonoyama, N. Dupre, D. Guyomard, K. Tamura, J. Mizuki, R. Kanno, Phys Chem Chem Phys, 12 (2010) 3815-3823.

[40] L.J. Liu, L.Q. Chen, X.J. Huang, X.Q. Yang, W.S. Yoon, H.S. Lee, J. McBreen, J Electrochem Soc, 151 (2004) A1344-A1351.

[41] M. Anicete-Santos, L. Gracia, A. Beltran, J. Andres, J.A. Varela, E. Longo, Phys Rev B, 77 (2008) 085112.

[42] N. Ishizawa, K. Tateishi, J Ceram Soc Jpn, 117 (2009) 6-14.

[43] B. Xu, S. Meng, J Power Sources, 195 (2010) 4971-4976.

[44] K. Sakamoto, M. Hirayama, N. Sonoyama, D. Mori, A. Yamada, K. Tamura, J. Mizuki, R. Kanno, Chem Mater, 21 (2009) 2632-2640.

[45] M. Hirayama, H. Ido, K. Kim, W. Cho, K. Tamura, J. Mizuki, R. Kanno, J Am Chem Soc, 132 (2010) 15268-15276.

[46] S. Taminato, M. Hirayama, K. Suzuki, K. Kim, Y.M. Zheng, K. Tamura, J. Mizuki, R. Kanno, J Mater Chem A, 2 (2014) 17875-17882.

[47] D.V. Safronov, S.A. Novikova, A.M. Skundin, A.B. Yaroslavtsev, Inorg Mater, 48 (2012) 57-61.

[48] W.C. Chueh, F. El Gabaly, J.D. Sugar, N.C. Bartelt, A.H. McDaniel, K.R. Fenton, K.R. Zavadil, T. Tyliszczak, W. Lai, K.F. McCarty, Nano letters, 13 (2013) 866-872.

[49] H. Chang, K. Kubota, G. Kobayashi, M. Hirayama, R. Kanno, J Power Sources, 252 (2014) 1-7.

[50] K. Kubota, T. Kaneko, M. Hirayama, M. Yonemura, Y. Imanari, K. Nakane, R. Kanno, J Power Sources, 216 (2012) 249-255.

[51] Y. Gao, J.N. Reimers, J.R. Dahn, Phys Rev B, 54 (1996) 3878-3883.

[52] M. Okada, Y.S. Lee, M. Yoshio, J Power Sources, 90 (2000) 196-200.

[53] Y. Yagi, Y. Hideshima, M. Sugita, H. Noguchi, M. Yoshio, Electrochemistry, 68 (2000) 252-253.

[54] C.H. Shen, R.S. Liu, R. Gundakaram, J.M. Chen, S.M. Huang, J.S. Chen, C.M. Wang, J Power Sources, 102 (2001) 21-28.

[55] D. Pasero, S. de Souza, N. Reeves, A.R. West, J Mater Chem, 15 (2005) 4435-4440.

[56] K.F. Chiu, H.C. Lin, K.M. Lin, C.C. Chen, J Electrochem Soc, 153 (2006) A1992-A1997.

[57] A. Manthiram, J.B. Goodenough, J Power Sources, 26 (1989) 403-408.

[58] A.K. Padhi, K.S. Nanjundaswamy, J.B. Goodenough, J Electrochem Soc, 144 (1997) 1188-1194.

[59] S. Shiraki, H. Oki, Y. Takagi, T. Suzuki, A. Kumatani, R. Shimizu, M. Haruta, T. Ohsawa, Y. Sato, Y. Ikuhara, T. Hitosugi, J Power Sources, 267 (2014) 881-887.

[60] H.W. Chan, J.G. Duh, S.R. Sheen, J Power Sources, 115 (2003) 110-118.

[61] M. Okubo, E. Hosono, J. Kim, M. Enomoto, N. Kojima, T. Kudo, H.S. Zhou, I. Honma, J Am Chem Soc, 129 (2007) 7444-7452.

[62] M. Jo, Y.S. Hong, J. Choo, J. Cho, J Electrochem Soc, 156 (2009) A430-A434.

[63] M. Okubo, Y. Mizuno, H. Yamada, J. Kim, E. Hosono, H.S. Zhou, T. Kudo, I. Honma, Acs Nano, 4 (2010) 741-752.

[64] A. Caballero, L. Hernan, J. Morales, E.R. Castellon, J. Santos, J Power Sources, 128 (2004) 286-291.

[65] H.U. Krebs, M. Weisheit, J. Faupel, E. Suske, T. Scharf, C. Fuhse, M. Stormer, K. Sturm, M. Seibt, H. Kijewski, D. Nelke, E. Panchenko, M. Buback, Adv Solid State Phys, 43 (2003) 505-517.

[66] B. Mercey, P.A. Salvador, W. Prellier, T.D. Doan, J. Wolfman, J.F. Hamet, M. Hervieu, B. Raveau, J Mater Chem, 9 (1999) 233-242.

[67] R. Mishra, Y.M. Kim, J. Salafranca, S.K. Kim, S.H. Chang, A. Bhattacharya, D.D. Fong, S.J. Pennycook, S.T. Pantelides, A.Y. Borisevich, Nano letters, 14 (2014) 2694-2701.

[68] B.B. Chen, P.F. Chen, H.R. Xu, X.L. Tan, F. Jin, Z. Guo, B.W. Zhi, W.B. Wu, Appl Phys Lett, 104 (2014) 242416.

[69] N. Sata, K. Eberman, K. Eberl, J. Maier, Nature, 408 (2000) 946-949.

[70] R.V.K. Mangalam, J. Karthik, A.R. Damodaran, J.C. Agar, L.W. Martin, Adv Mater, 25 (2013) 1761-1767.

[71] S. Das, A. Herklotz, E.J. Guo, K. Dorr, J Appl Phys, 115 (2014).

[72] A. Gupta, Curr Opin Solid St M, 2 (1997) 23-31.

[73] D.P. Norton, D.H. Lowndes, J.D. Budai, B.C. Chakoumakos, Mat Sci Eng B-Solid, 41 (1996) 374-378.

[74] C. Bhardwaj, B.S.S. Daniel, D. Kaur, Mater Lett, 87 (2012) 172-175.

[75] K. Kim, T. Toujigamori, K. Suzuki, S. Taminato, K. Tamura, J. Mizuki, rsquo, ichiro, M. Hirayama, R. Kanno, Electrochemistry, 80 (2012) 800-803.

[76] Y. Zheng, S. Taminato, Y. Xu, K. Suzuki, K. Kim, M. Hirayama, R. Kanno, J Power Sources, 208 (2012) 447-451.

[77] M. Komo, A. Hagiwara, S. Taminato, M. Hirayama, R. Kanno, Electrochemistry, 80 (2012) 834-838.

[78] S. Kim, M. Hirayama, S. Taminato, R. Kanno, Dalton T, 42 (2013) 13112-13117.

[79] S. Kim, M. Hirayama, K. Suzuki, R. Kanno, Solid State Ionics, 262 (2014) 578-581.

[80] M. Hirayama, M. Yonemura, K. Suzuki, N. Torikai, H. Smith, E. Watkinsand, J. Majewski, R. Kanno, Electrochemistry, 78 (2010) 413-415.

[81] M. Gilbert, P. Zubko, R. Scherwitzl, J. Iniguez and J. Triscone, Nat Mater, 11 (2012) 195-198.

[82] F. Cuccureddu, S. Murphy, I.V. Shvets, M. Porcu, H.W. Zandbergen, N.S. Sidorov, S.I. Bozhko, Surf Sci, 604 (2010) 1294-1299.

[83] J. Chakhalian, A.J. Millis, J. Rondinelli, Nat Mater, 11 (2012) 92-94.

Chapter 2: Experimental

2.1 Synthesis

2.1.1 Pulsed laser deposition (PLD) method

Synthesis of epitaxial thin film electrodes and layer-by-layer deposition process were carried out using a pulsed laser deposition (PLD) method. The PLD, a kind of physical vapor deposition (PVD) methods, is widely known as an effective method to fabricate multi-component oxide thin film due to easy control of composition and physical property. The specific composition of thin film could be realized from a target of desired composition without loss of elements and the control of thickness and crystallinity are also facile [1-3]. Figure 2.1 illustrates the schematic diagram of the PLD system equipped with a laser ablation system in a vacuum chamber. The PLD system is simply composed of a target with a desired composition, a substrate and a high power pulsed laser beam. When the high pulsed laser is focused on the target, the energy of laser converted to thermal, chemical and mechanical energy. These pulsed energies vaporize and/or ablate a small amount of the target material, then the ejected materials form a plume of plasma state including many energetic species such as atoms, molecules, electrons, ions, clusters, particulates and molten globules [4]. Lastly, the evaporated materials are adhered to the heated substrate facing to the substrate and condensed on the substrate, in which thin films are grown. For the PLD process, many kind of laser beam can be applied but excimer lasers are usually preferred. Among them, a krypton-fluoride (KrF) laser is a particular type of excimer laser, which is sometimes called an exciplex laser. With its 248 nm wavelength, it is used in the production of semiconductor circuits and high-resolution photolithography, the critical technologies requires accurately controlled thin film. The KrF laser could provide a high quality thin film.

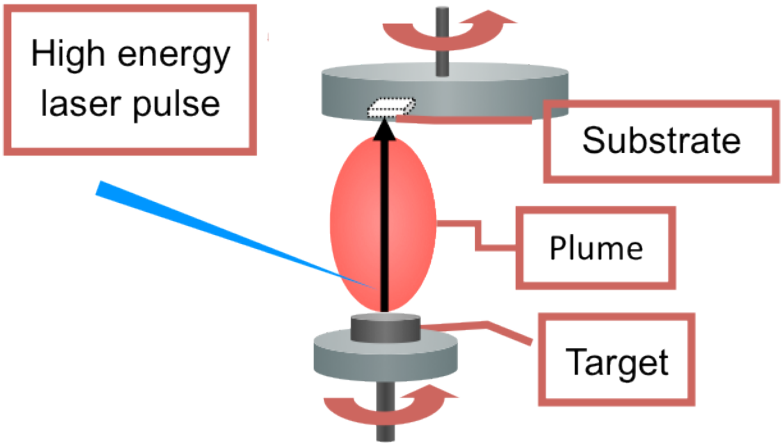

Figure 2.1 Schematic diagram of a PLD system.

In order to obtain a high quality thin film, it is necessary to understand parameters of the PLD method that effects on thin film characteristics such as crystallinity, stoichiometry, roughness and orientation. A relationship between each PLD parameter and characteristics of thin films is represented in table 2.1 [5-17]. A stoichiometric thin film with well alignment can be obtained by optimization of the parameters listed on the table. However, the PLD method has an inherent drawback that light atoms such as lithium, oxygen and nitrogen show larger scattering degree in the plasma plume and low sticking coefficients [18, 19]. This results in a thin film of distorted composition that light element are insufficient, comparing to that of the target material. It is a quite serious problem, but it can be overcome by adjusting synthesis conditions adequately.

Table 2.1 Relationship between PLD parameters and characteristics of thin films.

Component	Parameter	Characteristics
Substrate	Composition	Orientation, Distortion
	Orientation (*h k l*)	Orientation, Distortion
	Temperature (°C)	Crystallinity, Roughness
Laser	Energy (mJ)	Thickness, Roughness
	Frequency (Hz)	Thickness, Roughness
	Duration time (min.)	Thickness
	Focus lens distance (mm)	Thickness, Roughness
Target	Composition	Composition
	Distance to substrate (cm)	Roughness, Thickness, Composition
Atmosphere	Kind of gas	Oxidation state, Composition
	Pressure (Pa)	Thickness, Composition

2.1.2 Synthesis of epitaxial thin film electrode

In the present study, epitaxial thin film electrodes were synthesized on the 10 x 10 x 0.5 mm size of Nb-doped (0.5 wt.%) single crystal $SrTiO_3$ substrate with cubic perovskite structure (space group *Pm*-3*m*). The deposition was performed by a PLD system (AOV Inc.) equipped with a KrF excimer laser at a wavelength of 248 nm. The pre-treatment of the substrate was carried out by washing with ultra pure water and annealing at 1000 °C under oxygen flow. The target and substrate were rotated during the deposition process to obtain uniform ablation of the target and homogeneous composition on the entire surface of the substrate. The specific electrical resistance of the $SrTiO_3$ substrate is 5.28×10^{-3} Ω cm, which is slight high to secure electric current for electrochemical reaction of the thin film electrode. Therefore, a gold film was sputtered on the back and lateral side of substrate using a QUICK COATER SC-701 (Sanyu Electron Co., Ltd.). Then, a $SrRuO_3$ buffer layer was deposited on the substrate to form an electrical contact between the semiconducting electrodes and the gold current collector [20]. The

$SrRuO_3$ layer was synthesized with $SrRuO_3$ target (Toshima Manufacturing Co., Ltd.) using the PLD system. The synthesis conditions of $SrRuO_3$ thin film was summarized in table 2.2.

Table 2.2 PLD conditions for epitaxial $SrRuO_3$ thin film deposited on $SrTiO_3$ substrate.

Target	E (J cm^{-2})	T (°C)	P_{O2} (Pa)	d (mm)	t (min.)	f (Hz)
$SrRuO_3$	0.56	600	10	60.6	20	5

2.1.2.1 Fabrication of $LiCoO_2$ epitaxial thin film

Table 2.3 shows the PLD conditions of epitaxial $LiCoO_2$ thin film. The $LiCoO_2$ epitaxial thin film was grown on the (100) plane of the $SrTiO_3$ single crystal substrate where the $SrRuO_3$ buffer layer is pre-deposited as a current collector. The desired thickness of $LiCoO_2$ thin film was obtained by adjusting the parameter of duration time.

Table 2.3 PLD conditions for epitaxial $LiCoO_2$ thin film deposited on $SrTiO_3$ (100) substrate.

Target	E (J cm^{-2})	T (°C)	P_{O2} (Pa)	d (mm)	t (min.)	f (Hz)
$Li_{1.4}CoO_2$	0.42	600	3.3	60.6	20	10

2.1.2.2 Layer-by-layer deposition with $LiMn_2O_4$ and $LiCoO_2$ epitaxial thin films

The PLD conditions of each film used for layer-by-layer deposition are summarized in Table 2.4. The layer-by-layer deposition began with a $LiMn_2O_4$ layer, followed by a $LiCoO_2$ layer. This is henceforth referred to as the 2-step film. A 4-step film was also produced by repeating the 2-step deposition process; after the deposition of the $LiMn_2O_4$ and $LiCoO_2$, another $LiMn_2O_4$ and $LiCoO_2$ layers were deposited again in the same manner with the 2-step film. The deposition times of $LiMn_2O_4$ and $LiCoO_2$ were adjusted to half of those of the 2-step film to keep comparable total thickness each other. Between each deposition step, the substrate was cooled down to room temperature and then heated to the temperature required for the next step. A single-step Li-Co-Mn-O thin film, henceforth referred to as the 1-step film and a $LiMn_2O_4$ film are also prepared for comparison. The $LiMn_2O_4$ epitaxial thin film was synthesized with the same PLD conditions to that of the $LiMn_2O_4$ applied into layer-by-layer deposition process. The PLD conditions of the 1-step film were shown in table 2.5.

Table 2.4 PLD conditions of $LiMn_2O_4$ and $LiCoO_2$ epitaxial thin films deposited on $SrTiO_3$ (111) substrate for layer-by-layer deposition.

Target	*E* (J cm^{-2})	*T* (°C)	P_{O2} (Pa)	*d* (mm)	*t* (min.)	*f* (Hz)
$Li_{1.2}Mn_2O_4$	0.56	650	6.6	60.6	22	10
$Li_{1.4}CoO_2$	0.51	650	6.6	60.6	10	10

Table 2.5 PLD conditions of 1-step epitaxial thin film deposited on $SrTiO_3$ (111) substrate.

Target	*E* (J cm^{-2})	*T* (°C)	P_{O2} (Pa)	*d* (mm)	*t* (min.)	*f* (Hz)
$Li_{1.4}Co_{0.65}Mn_{1.35}O_4$	0.50	650	6.6	60.6	30	10

2.1.3 Target synthesis

2.1.3.1 $LiCoO_2$ target

The lithium cobalt oxide, $LiCoO_2$, target was prepared by solid state reactions of lithium hydroxide monohydrate ($LiOH \cdot H_2O$, Nacalai, 99.0%) and cobalt (II,III) oxide (Co_3O_4, Kojundo Chemical Lab. Co., Ltd., 99.9%). Excess lithium composition (Li:Co = 1.4:1) was adjusted to compensate lithium loss during the PLD process. Precursor powders were put into an alumina container with alumina balls (10 x 10 mm*ϕ*, 15 x mm*ϕ*) and 50 mL of acetone. Mixing and grinding were performed by planetary milling apparatus (Itoh LA-PO4) for 1 hour. Then, the powders were dried at room temperature for 12 hours and formed into a disk type pellet with 30 MPa. Lastly, the pellet was sintered at 750 °C for 6 hours under ambient atmosphere [21]. The heating program is illustrated in figure 2.2.

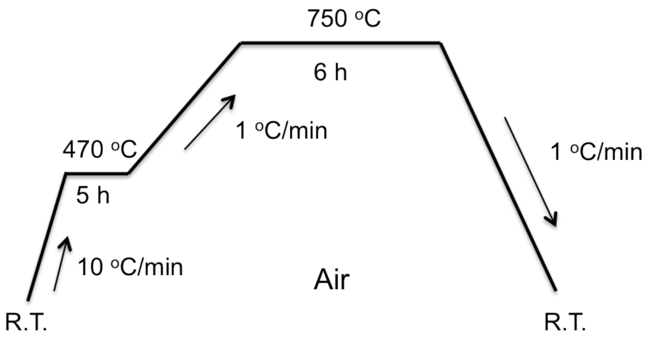

Figure 2.2 The sintering program of $LiCoO_2$ target.

2.1.3.2 $LiMn_2O_4$ target

The lithium manganese oxide, $LiMn_2O_4$, target was synthesized by solid state reactions of lithium hydroxide monohydrate ($LiOH \cdot H_2O$, Nacalai, 99.0%) and manganese dioxide (MnO_2, Kojundo Chemical Lab. Co., Ltd., 99.99%). The composition was lithium rich (Li:Mn = 1.2:2) in order to compensate for lithium loss during the PLD process. The precursor powders were mixed and ground in a mortar for 30 minutes to obtain homogeneous mixture. The powders were pelletized with 30 MPa then annealed at 800 °C for 12 hours under oxygen atmosphere. The obtained pellet was ground again then sintered at 900 °C for 24 hours in oxygen gas flow condition [22]. The synthesis process is shown in figure 2.3.

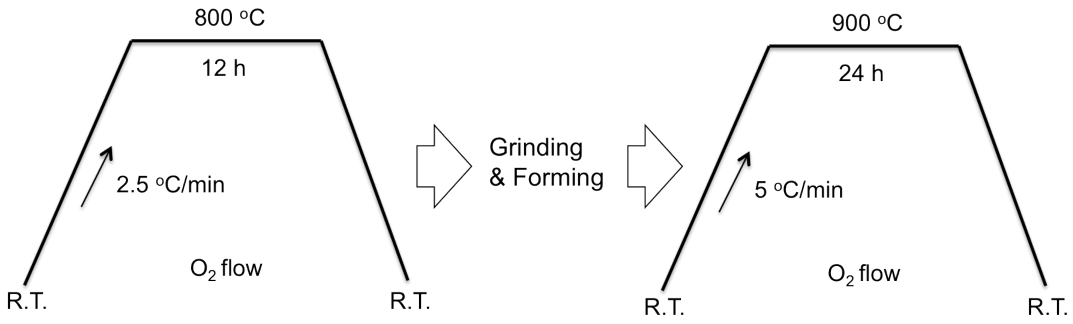

Figure 2.3 The synthesis process of $LiMn_2O_4$ target.

2.1.3.3 Li-Co-Mn-O target

The PLD target of 1-step film, Li-Co-Mn-O, was synthesized by solid state reaction of lithium hydroxide monohydrate ($LiOH \cdot H_2O$, Nacalai, 99.0%), manganese dioxide (MnO_2, Kojundo Chemical Lab. Co., Ltd., 99.99%) and cobalt (II,III) oxide (Co_3O_4, Kojundo Chemical Lab. Co., Ltd., 99.9%). The composition of the 1-step film was adjusted to that of the 2-step film with excess lithium amount (Li:Co:Mn = 1.4:0.65:1.35) for compensating lithium loss during PLD process. The precursor powders were ground and mixed using a mortar for 30 minutes then pelletized with 30 MPa and sintered at 800 °C for 24 hours under oxygen atmosphere. [23] The sintering program is displayed in figure 2.4.

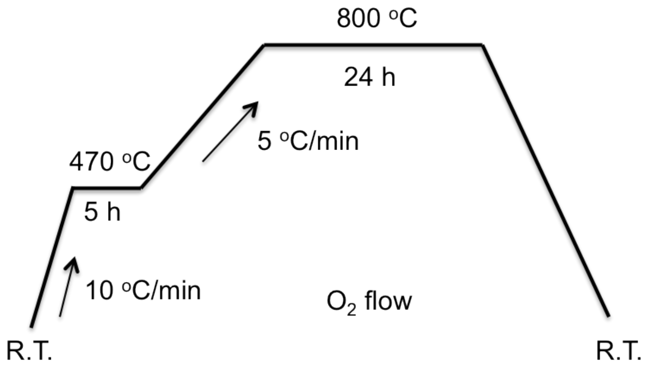

Figure 2.4 The sintering program of 1-step film target.

2.2 Characterization by X-ray

2.2.1 X-ray diffraction (XRD) method

Diffraction refers to physical phenomena that occur when a wave encounters a periodic obstacle array, producing constructive interference at specific position [24]. Crystals have periodic atom arrangement with long-range order, which deserves to diffract waves. X-ray is used to investigate diffraction of crystals and to obtain the information for atomic arrangement since its wavelength is comparable with the interatomic distance and bond length. The interference must occur following Bragg`s law, as illustrated in figure 2.5.

$$\lambda = 2d_{hkl} \sin \theta$$

where d is the distance between the parallel *hkl* plane, λ is the wavelength of X-ray, θ is the incident angle of X-rays.

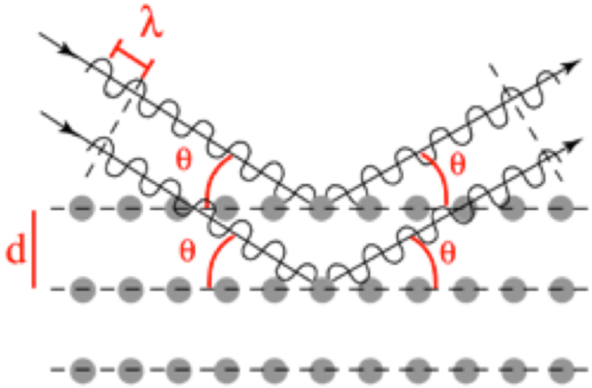

Figure 2.5 Principles of X-ray diffraction.

The obtained results, position of peaks, shape and relative intensities from X-ray diffraction (XRD) patterns provide crystallographic information such as phase, crystallinity, orientation, lattice parameters and grain size. In particular, intensity in diffraction peaks is a good indicator of atomic arrangement in a crystal structure. In the present study, the synthesized PLD targets were characterized by XRD technique. X-ray diffractometers (Rigaku Ru-200B, SmartLab) with Cu Kα radiation was used for collecting the data of XRD patterns. The measurements were performed in the 2θ range from 10 to 100°.

2.2.2 Thin film X-ray diffraction method

Orientations and crystallinity of the synthesized thin films were characterized by the out-of-plane and in-plane measurements using a thin film X-ray diffractometer (Rigaku, ATX-G) installed with monochromatic Cu $K\alpha_1$ radiation. The measurements were performed with conditions, a scan rate of 5°/min. and a step width of 0.02° in a 2θ or $2\theta\chi$ range from 10 to 100°.

Out-of-plane and in-plane XRD measurements are methods to evaluate the thin films characteristics along perpendicular and parallel directions to the substrate surface plane. The measurement directions are displayed by figure 2.6.

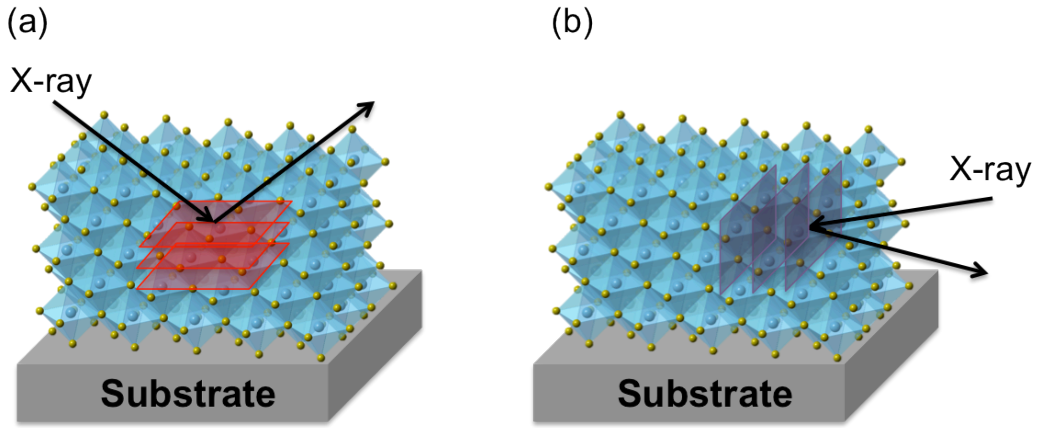

Figure 2.6 Schematic illustrations of (a) out-of-plane and (b) in-plane X-ray diffraction measurement.

The in-plane measurement is conducted by lowering the incident X-ray angle to the X-ray critical angle where a total reflection occurs. The critical angles are determined by the refractive index of the materials and the energy of X-rays. When the incident angle of X-ray is adjusted to lower angle than the critical angle, the X-ray can penetrate the materials within 10 mm of depth. Then, the X-ray goes through the surface of the material along parallel direction to surface of the substrate when the incident angle is same to the critical angle. Therefore, when the crystal plane normal to surface plane of the sample agrees with the Braggs law, the diffraction takes place on the surface and crystallographic information of the lattice plane aligned along perpendicular direction of the substrate plane can be obtained. The ϕ scan measurement was performed with fixing a detector at spontaneous $2\theta\chi$ angle and rotating the thin film along parallel direction of its surface plane. With the ϕ scan measurement, it is possible to confirm the rotation symmetry of the lattice plane perpendicular to the substrate plane. The data were collected with 24°/min of scan rate, 0.05° of measurement step and range from -169 to 180°.

2.2.3 X-ray reflectivity (XRR)

The density, thickness and surface roughness of synthesized films were characterized by X-ray reflectivity (XRR) measurement using a thin film X-ray diffractometer (Rigaku, ATX-G) with Cu kα_1 radiation. The measurement conditions were a scan rate of 0.2°/min., a step width of 0.02° of step width and 2θ range from 0.2 to 4°. The obtained XRR spectra were analyzed based on fast Fourier transform (FFT) and simulated using the Parratt32 software to obtain the information of the film characteristics [25, 26]. The density of each layer was evaluated by real part of scattering length density (SLD) with the following equation;

$$d = (M \cdot SLD) / (r_0 \mathrm{N_a} Z)$$

where a M is the molecular weight, r_0 is the Bohr atomic radius, $\mathrm{N_a}$ is the Avogadro constant and Z is overall atomic weight.

2.2.4 Hard X-ray photoelectron spectroscopy (HAXPES)

X-ray photoelectron spectroscopy (XPS) is a representative surface-sensitive quantitative spectroscopic technique that examines electronic state, empirical formula and chemical state of the elements in a material. A principle of XPS is based on photoelectric law of photoemission phenomena, suggested by Albert Einstein in 1905s [27]. Figure 2.7 summarizes the photoemission phenomena and relation between the energy levels and electron energy distribution divided by incident X-ray with energy of $h\nu$. When a material is irradiated by X-ray, photoelectrons are emitted from the surface of material. During the process, a contribution of the incident X-ray energy ($h\nu$) for a photoelectron is divided into three components, binding energy (E_b) of an electron bound in core level, work function (ϕ) to remove the electron from the material to a point in the vacuum and kinetic energy (E_k) of the electron escaped from the material. The kinetic energy (E_k) has a relationship with the other electron energies as follows;

$$E_k = h\nu - E_b - \phi$$

The feasible depth of XPS measurement is determined by inelastic mean free path (IMFP) of the photoelectrons within the material [28]. These IMFP values are known as a few nanometers at around 50 - 100 eV, thus the XPS is used for mainly analyzing the surface. However, the use of synchrotron radiation (Hard X-rays) provides the ability to tune the excitation photon energy over a wide range, and third generation synchrotron radiation facilities offer opportunities for high-resolution, high-throughput photoemission spectroscopy. With the hard X-ray, over 30 nm of depth is apparently investigated.

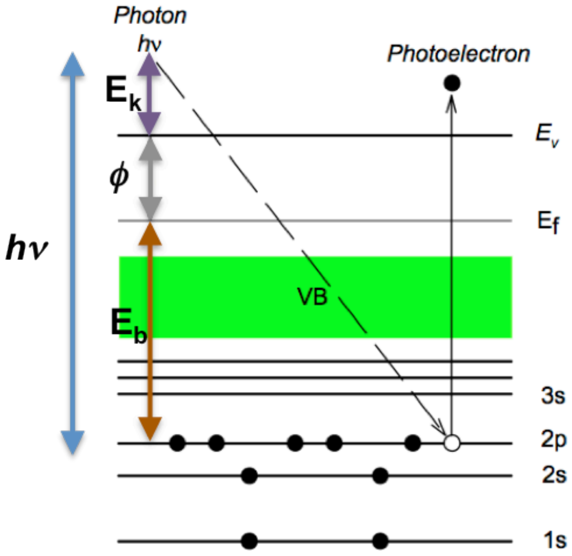

Figure 2.7 Photoemission effect showing relation between the energy levels and electron energy distribution divided by incident X-ray with an energy of $h\nu$.

2.2.5 In situ X-ray absorption fine structure spectroscopy (XAFS)

X-ray absorption fine structure (XAFS) utilizes the X-ray absorption for an atom at energies near and above the core-level binding energies of the atom. Since XAFS spectra are sensitive to the oxidation state, coordination chemistry, and the distances, coordination number and species of atoms surrounding the selected element, XAFS is regarded as a practical and effective way to determine the chemical state and local atomic structure of the selected atom. In particular, *in situ* XAFS measurement enables to detect the electronic structural changes of transition metals in the electrode materials according to lithium (de)intercalation during the charge-discharge process. Figure 2.8 displays principle of XAFS measurement. The binding energy of a specific core level for the selected atom should be less than the energy of the incident

X-ray to result in absorption of the core level and measure the XAFS. When the irradiated X-ray with higher energy than that of the binding energy of electron, the electron is removed from the core level. In this process, the X-ray is absorbed and the remained excess energy is given to a photoelectron, escaped from the atom. The total implications of this process result in XAFS spectra. When the X-ray absorption phenomena are considered, an absorption coefficient (μ), showing the probability of X-ray absorption, should be concerned. The absorption coefficient (μ) has a relationship with following Beer`s law [29];

$$I = I_0 e^{-\mu t}$$

where I_0 is the X-ray intensity incident on a sample, t is the sample thickness, and I is the intensity transmitted through the sample. The I_0 and I are measured with varying the incident X-ray energy to reveal the relationship between the absorption coefficient μ and the X-ray intensity transmitted through sample for obtaining the XAFS spectra. Generally, the absorption coefficient μ shows a smooth function for most X-ray energies. However, when the incident X-ray has an energy equal to that of the binding energy of a core-level electron, a sharp rise in absorption coefficient is represented. The abrupt increase of energy is defined as an absorption edge, attributed to the promotion of the core level to the continuum. Since the energy of absorption edge is absolutely determined by atom species, information of the atom species and their chemical states can be simply acquired by observing the absorption edge energy. The X-ray absorption spectrum is typically separated into two regimes for the purpose of interpretations: X-ray absorption near-edge spectroscopy (XANES) and extended X-ray absorption fine structure spectroscopy (EXAFS). The XANES spectrum is XAFS spectrum at near absorption edge region, which is strongly sensitive to oxidation state and coordination chemistry of the absorbing atom. On the other hand, the EXAFS indicates the region with higher X-ray energy, which is used to determine the distances, coordination number, and species of the neighbors of the absorbing atom.

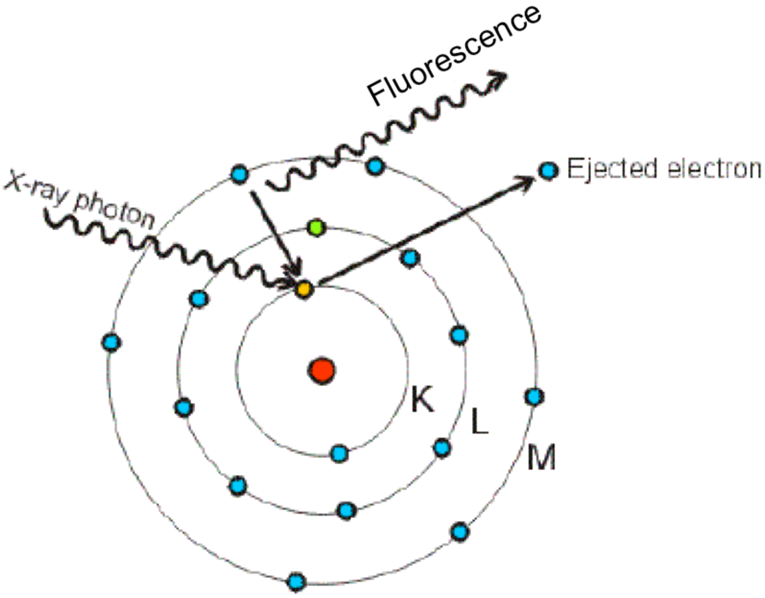

Figure 2.8 Principle of XAFS measurement.

In situ X-ray absorption near edge structure (XANES) measurements are performed to evaluate the dynamic electronic structural changes for a thin film electrode. Figure 2.9 shows schematic diagram of *in situ* XAFS measurement with fluorescence mode. A kind of the designed *in situ* spectroelectrochemical cell [30] is used to investigate continuous electronic structural changes according to electrochemical lithium intercalation and deintercalation. The lithium metal is used as the counter electrode, and EC/DEC with a molar ratio of 3:7 in 1M $LiPF_6$ is employed as electrolyte solution. A control of the voltage was performed by potentiostatic mode with a potentiostat/galvanostat (Hokuto Denko, HA-501).

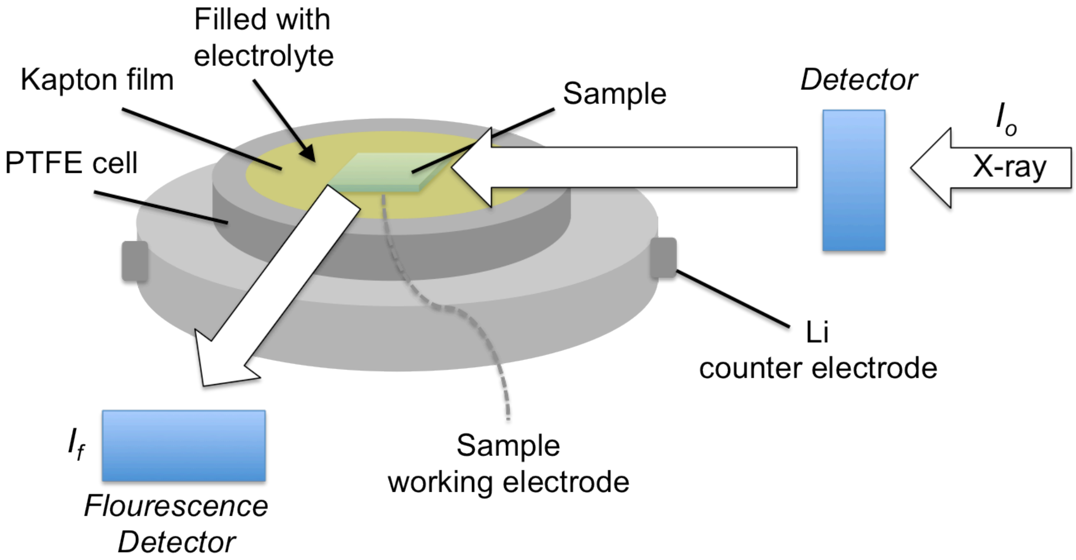

Figure 2.9 Two electrodes cell for *in situ* XAFS measurement with fluorescence mode.

2.3 High resolution transmission electron microscope (HRTEM) observation

Local crystal structure of the 2-step thin film was observed by scanning transition electron microscopy (STEM), using an aberration corrected-STEM (R005 electron microscope [31]) and high angle annular dark field (HAADF) images were obtained. The film was observed with the cross-sectional geometry along the [1-10] direction of the substrate with 300 kV of accelerating voltages. The sample was cut along the (1-10) planes of the $SrTiO_3$ substrate and ground until a hundred nanometer of thickness by a mechanical polishing method. Finally, the ground samples were thinned to electron transparency using a Ga-ion beam (FEI Co., Dual Beam System Nova-200 Nanolab) at 30 kV. Information for a distribution of components were obtained by electron energy loss spectroscopy (EELS) mapping in STEM.

2.4 Electrochemical property

2.4.1 Cell preparation

Electrochemical properties of the thin film electrodes were characterized using CR2032 cells fabricated in a glove box under Ar atmosphere. Figure 2.10 depicts assembling of the cell with constituent components. The thin film electrodes and lithium metal were used as a working electrode and a reference electrode, respectively. A supporting solvent of 1 M $LiPF_6$ included ethylene carbonate (EC)/diethyl carbonate (DEC) mixture with a volume ratio of 3:7 was used as an electrolyte. The fabricated cells were kept at room temperature for 24 hours before electrochemical measurements in order to make preferred state that electrolyte perfectly soaked into the electrode material.

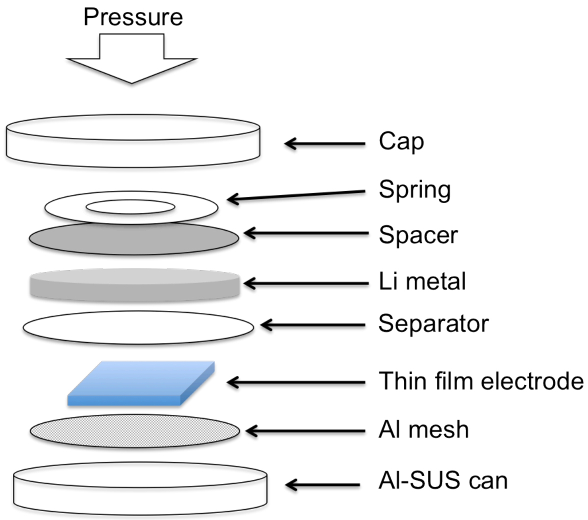

Figure 2.10 Assembling of CR2032 cell with constituent components.

2.4.2 Cyclic voltammetry

Cyclic voltammetry (CV), well known as a potentiodynamic electrochemical test, are utilized to confirm the phenomena dominating charge storage for complex reaction systems. The CV measurement provides data not only for the semi-infinite linear diffusion but also for the surface-controlled phenomena [32, 33]. A peak of current-potential curve, obtained by CV measurement, contains contributions of both phenomena semi-infinite linear diffusion and surface-controlled reaction. A principal phenomenon affects to the reaction can be estimated by measuring current (i) at fixed potential with varying scan rate (v). The variation of current with scan rate is expressed by as follows;

$$i = av^b$$

where the a and b are adjustable parameters.

Among the two charge storage phenomena, the surface-controlled reaction is resulted from charges stored on the surface of electrode with obeying the interaction formula as follows [32, 33];

$$i = Cv$$

where the C is capacitance.

On the other hand, the semi-infinite linear diffusion, bulk diffusion, is resulted from charges stored on the bulk of electrode in which the relation between current and scan rate is expressed by Randles-Sevcik equation [32];

$$i_p = (2.69 \text{ x } 10^5)\, n^{3/2} ACD^{1/2} v^{1/2} \quad \text{at room temperature}$$

where the i_p is current maximum in amperage, n is a number of electron, A is a reaction surface area, C is a surface density and D indicates a chemical diffusion coefficient. As illustrated above, the capacitive current has a linear dependency on the scan rate. Therefore, near 1.0 of the b value is revealed in the formula obtained from CV measurement when the surface-controlled phenomenon strongly dominates the reaction system. On the other hand, the current caused by bulk diffusion is proportional to the scan rate power 0.5. That is, the b value approaches to 0.5 under the domination of intercalation process. Analysis for relationship between the scan rate and current using CV is a very simple and powerful tool to investigate the major component dominates the charge storage since the scan rate is varied only slightly more than one order of magnitude.

A potential of electrode material is controlled by external potentiostat. The potential is varied from a specific initial potential to final potential with a constant scan rate. The potential change is performed along both forward and reverse directions. Various conditions, scan range, speed and a number of cycles, are adjusted according to the purpose of experiments. The CV measurements fundamentally provide information in terms of oxidation and reduction potentials of electrodes, the reversibility of the reaction and the diffusion coefficient.

2.4.3 Galvanostatic charge discharge

Charge-discharge characteristics such as capacity and rate capability of the synthesized thin films were examined by galvanostatic constant current charge-discharge measurements using a TOSCAT-3100 (Toyo System) cycler. The test was conducted under the wide range from 1.6 and 4.5 V. Rate capability is an effective technique to evaluate the electrochemical performance of an electrode material. The amount of discharge capacity is measured for the electrode with varying experimental conditions, cycle numbers and values of constant current. In the results, the specific current is expressed by means of C-rate, which is the theoretical amount of charge that can extract the amount of corresponding lithium from the electrode material within one hour. In this study, the rate capabilities of the thin film electrodes were investigated by varying the applied currents from 0.5 to 10 μA.

References

[1] H.U. Krebs, M. Weisheit, J. Faupel, E. Suske, T. Scharf, C. Fuhse, M. Stormer, K. Sturm, M. Seibt, H. Kijewski, D. Nelke, E. Panchenko, M. Buback, Adv Solid State Phys, 43 (2003) 505-517.

[2] B. Mercey, P.A. Salvador, W. Prellier, T.D. Doan, J. Wolfman, J.F. Hamet, M. Hervieu, B. Raveau, J Mater Chem, 9 (1999) 233-242.

[3] G.J.H.M.R. Dave H. A. Blank, Gertjan Koster, Horst Rogalla, Applied Surface Science, (1994).

[4] H.M. Christen, G. Eres, J Phys-Condens Mat, 20 (2008).

[5] T. Ohnishi, K. Takada, Appl Phys Express, 4 (2011) 025501.

[6] M. Komo, A. Hagiwara, S. Taminato, M. Hirayama, R. Kanno, Electrochemistry, 80 (2012) 834-838.

[7] N. Sonoyama, K. Iwase, H. Takatsuka, T. Matsumura, N. Imanishi, Y. Takeda, R. Kanno, J Power Sources, 189 (2009) 561-565.

[8] K. Dimmler, M. Parris, D. Butler, S. Eaton, B. Pouligny, J.F. Scott, Y. Ishibashi, J Appl Phys, 61 (1987) 5467-5470.

[9] R.K. Singh, J. Narayan, Phys Rev B, 41 (1990) 8843-8859.

[10] H.W. Bergmann, K. Schutte, E. Schubert, A. Emmel, Applied Surface Science, 86 (1995) 259-265.

[11] S. Metev, M. Ozegowski, G. Sepold, S. Burmester, Applied Surface Science, 96-8 (1996) 122-125.

[12] J.D. Perkins, C.S. Bahn, J.M. McGraw, P.A. Parilla, D.S. Ginley, J Electrochem Soc, 148 (2001) A1302-A1312.

[13] X.J. Huang, S.Y. Xu, C.K. Ong, Z. Yang, L. Si, Y. Li, J Appl Phys, 91 (2002) 4666-4671.

[14] M. Liu, X.Q. Wei, Z.G. Zhang, G. Sun, C.S. Chen, C.S. Xue, H.Z. Zhuang, B.Y. Man, Applied Surface Science, 252 (2006) 4321-4326.

[15] A. Rousseau, V. Laur, M. Guilloux-Viry, G. Tanne, F. Huret, S. Deputier, A. Perrin, F. Lalu, P. Laurent, Thin Solid Films, 515 (2006) 2353-2360.

[16] X.H. Xu, R.Q. Zhang, X.Z. Dong, G.A. Gehring, Thin Solid Films, 515 (2006) 2754-2759.

[17] Z.G. Zhang, F. Zhou, X.Q. Wei, M. Liu, G. Sun, C.S. Chen, C.S. Xue, H.Z. Zhuang, B.Y. Man, Physica E, 39 (2007) 253-257.

[18] S. Canulescu, T. Lippert, H. Grimmer, A. Wokaun, R. Robert, D. Logvinovich, A. Weidenkaff, A. Doebeli, Applied Surface Science, 252 (2006) 4599-4603.

[19] R. Perez-Casero, J. Perriere, A. Gutierrez-Llorente, D. Defourneau, E. Millon, W. Seiler, L. Soriano, Phys Rev B, 75 (2007).

[20] K. Suzuki, K. Kim, S. Taminato, M. Hirayama, R. Kanno, J Power Sources, 226 (2013) 340-345.

[21] R. Huang, T. Hitosugi, C.A.J. Fisher, Y.H. Ikuhara, H. Moriwake, H. Oki, Y. Ikuhara, Mater Chem Phys, 133 (2012) 1101-1107.

[22] M. Hirayama, N. Sonoyama, M. Ito, M. Minoura, D. Mori, A. Yamada, K. Tamura, J. Mizuki, R. Kanno, J Electrochem Soc, 154 (2007) A1065-A1072.

[23] H. Kawai, M. Nagata, H. Tukamoto, A.R. West, Electrochem Solid St, 1 (1998) 212-214.

[24] A. Plancon, C. Tchoubar, Clay Clay Miner, 25 (1977) 430-435.

[25] L. Parratt, Physical Review, 95 (1954) 359-369.

[26] B. Jerliu, L. Dorrer, E. Huger, G. Borchardt, R. Steitz, U. Geckle, V. Oberst, M. Bruns, O. Schneider, H. Schmidt, Phys Chem Chem Phys, 15 (2013) 7777-7784.

[27] A. Einstein, Ann Phys-Berlin, 17 (1905) 132-148.

[28] S. Tanuma, T. Shiratori, T. Kimura, K. Goto, S. Ichimura, C.J. Powell, Surf Interface Anal, 37 (2005) 833-845.

[29] M. Newville, Rev Mineral Geochem, 78 (2014) 33-74.

[30] M. Hirayama, M. Yonemura, K. Suzuki, N. Torikai, H. Smith, E. Watkinsand, J. Majewski, R. Kanno, Electrochemistry, 78 (2010) 413-415.

[31] H. Sawada, Y. Tanishiro, N. Ohashi, T. Tomita, F. Hosokawa, T. Kaneyama, Y. Kondo, K. Takayanagi, J Electron Microsc, 58 (2009) 357-361.

[32] H. Lindstrom, S. Sodergren, A. Solbrand, H. Rensmo, J. Hjelm, A. Hagfeldt, S.E. Lindquist, J Phys Chem B, 101 (1997) 7717-7722.

[33] V. Augustyn, J. Come, M.A. Lowe, J.W. Kim, P.L. Taberna, S.H. Tolbert, H.D. Abruna, P. Simon, B. Dunn, Nat Mater, 12 (2013) 518-522.

Chapter 3: Analysis for low voltage reactions of multi-layer epitaxial thin film electrode

3.1 Introduction

Epitaxial thin film electrodes have been used for reaction analysis of the lithium battery electrodes [1-6]. The restricted two-dimensional surface and crystal orientation with atomically smooth surface provide well-defined reaction field to be analyzed by X-ray/neutron scattering techniques. However, there is also a disadvantage of the epitaxial electrodes. Because, epitaxial growth proceeds on single crystal substrate surface, lattice strain, chemical reaction and physical/electrochemical properties affects the epitaxial electrodes especially electrochemical performance. Representative single crystal substrate, $SrTiO_3$ has a large resistance over 10^7 Ω cm and Nb-doped $SrTiO_3$ also does not have enough electric conductivity compared to those of practical current collectors (Al: 2.66×10^{-6} Ω cm; Cu: 1.67×10^{-6} Ω cm). Therefore, electric conductive $SrRuO_3$ has introduced between the substrate and the electrode materials to compensate the electric conductivity for battery reactions [5, 7, 8]. Furthermore, Au sputtering was carried out for back and lateral side of the substrates. According to the previous reports, these conductive materials are inactive for electrochemical reaction at a voltage range between 3.0 to 5.0 V. However, electrochemical properties of these materials under 3.0 V region is still unclear. In this study, a novel electrode material is developed using layer-by-layer process. The novel electrode material could have unique structure and electrochemical properties, thus electrochemical characterization in wide voltage range is necessary to evaluate the novel electrode. In addition, nano-sizing effect and/or unexpected electrochemical reaction at the low voltage region have been reported [9-11]. Therefore, to improve the accuracy for electrochemical characterization, multi-layer epitaxial thin film electrode was subjected to electrochemical analysis at low voltage region.

There are several components to be considered in the multi-layer epitaxial electrode, electrode material, current collectors: $SrRuO_3$, Au, and $SrTiO_3$ substrate. To observe electrochemical characteristics and contributions of the $SrTiO_3$, $SrRuO_3$ and Au in epitaxial thin film electrode during charge-discharge, an electrode material with low electrochemical activity at low voltage region is required. Among several representative electrode materials, $Li_4Ti_5O_{12}$ and TiO_2 showed unknown reactions [33] and $LiMn_2O_4$ shows electrochemical reactions around 3 V [34]. Therefore, $LiCoO_2$ with low electrochemical activities below 3 V was selected for epitaxial thin film electrode.

In this study, $SrTiO_3$ (100) substrate where gold is coated on the backside and $SrRuO_3$ of electric current collector were used for synthesis of the epitaxial $LiCoO_2$ thin film electrode. First, the $SrRuO_3$ layer was deposited onto the $SrTiO_3$ (100) substrate with epitaxial growth then $LiCoO_2$ epitaxial thin film was synthesized on the $SrRuO_3$ layer. $LiCoO_2$, the representative intercalation compound, has been widely used as a cathode material of lithium batteries due to its remarkable reversibility and high electrochemical potential. With the stability and high energy density, the $LiCoO_2$ epitaxial thin film has been also utilized for the research of surface and interface. A crystal orientation of the $LiCoO_2$ epitaxial thin film can be controlled by orientations of the used substrate. In present study, the $LiCoO_2$ aligned along [104] direction was synthesized using $SrTiO_3$ (100) substrate since migration of lithium is not prohibited in the crystal structure of $LiCoO_2$ (104) during the (de)intercalation process [20]. The electrochemical characteristics of $LiCoO_2$ / $SrRuO_3$ / $SrTiO_3$ epitaxial thin film electrode below 3 V is investigated. The perovskite $SrTiO_3$ (space group: $Pm\text{-}3m$) and orthorhombic $SrRuO_3$ (space group: *Pbnm*) are known as electrochemically in-active materials with no ion conductivity. Electrochemical characteristics of the $SrTiO_3$ substrate and $SrRuO_3$ deposited on the $SrTiO_3$ are examined to distinguish the electrochemical contribution for each component at low voltage of below 3 V. Furthermore, electrochemical properties of the bare $SrTiO_3$ and the gold-coated $SrTiO_3$ were compared to reveal the effect of the gold current collector.

3.2 Results and discussion

3.2.1 Electrochemical properties of $LiCoO_2$/$SrRuO_3$ multi-layer thin film electrodes

3.2.1.1 Characterization of the $LiCoO_2$ target for PLD

Figure 3.1 shows XRD patterns of $Li_{1.4}CoO_2$ target for the PLD. The observed diffraction peaks are indexed as a layered rock salt type structure (space group: *R*-3*m*) of rhombohedral unit cell. Lattice parameters were calculated from the identified peaks and expressed with hexagonal lattice as a = 2.8144, c = 14.0388 Å. The calculated lattice parameters are comparable to those of reported $LiCoO_2$ (ICSD No. 1809989): a = 2.8137, c = 14.0783 Å. Small peaks, indicated by asterisks, correspond to impurity of Li_2CO_3, which is attributed to the excess lithium composition and synthesis under ambient atmosphere. These results verify that $LiCoO_2$ with lithium rich composition was successfully synthesized.

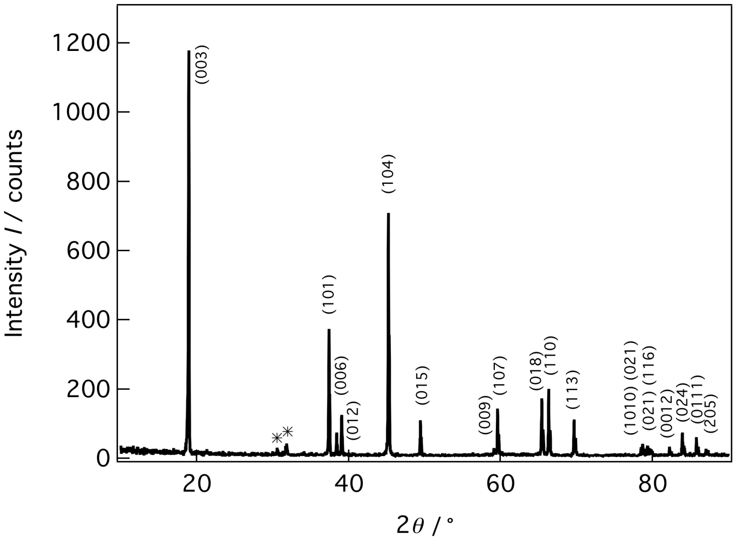

Figure 3.1 XRD patterns of $LiCoO_2$ target for PLD. Asterisks indicate impurity phases of Li_2CO_3.

3.2.1.2 Synthesis and structure characterization of $LiCoO_2/SrRuO_3$ epitaxial thin film

The epitaxial $LiCoO_2/SrRuO_3/SrTiO_3$ epitaxial multi-layer thin film was synthesized and its detailed structure was analyzed by thin film XRD measurements. Information of thickness, density and surface roughness were obtained by XRR and their fitting process.

The PLD synthesis condition of $SrRuO_3$ epitaxial thin film was optimized as follows: laser energy density, 0.56 J cm^{-2}; substrate temperature, 600 °C; oxygen pressure 10.0 Pa; laser frequency, 5 Hz; distance between substrate and target, 60.6 mm. Figure 3.2(a) shows out-of-plane XRD pattern of the $SrRuO_3$ thin film synthesized on the $SrTiO_3$ (100) substrate. The ovserbed diffraction peaks of the $SrRuO_3$ thin film are indexed using a pseudo cubic unit cell [35]. The *h*00 reflection was observed in the out-of-plane XRD measurement without impurity peaks. This result illustrates the $SrRuO_3$ thin film was grown with a (100) orientation on the $SrTiO_3$ (100) substrate. The lattice parameter of the $SrRuO_3$ thin film calculated by the 100 and 200 diffraction with a cubic system was 3.972 Å. The obtained lattice parameter indicates formation of a perovskite structure with a slightly larger unit cell than the $SrTiO_3$ substrate: a = 3.911 Å. Figure 3.2(b) shows a magnification of the out-of-plane XRD pattern between the 2θ range of 17 and 29°. Pendellösung interference fringes are detected around the 100 diffraction lines of the thin film. The fringes are used to occur from XRD measurement of thin films with highly oriented crystallinity [36-38]. Observation of the fringes in the diffraction peaks indicates a formation of high crystalline $SrRuO_3$ thin film. In-plane XRD diffraction lines of the $SrRuO_3$ synthesized on the $SrTiO_3$ substrate are not detected due to extremely similar unit cell sizes of the $SrRuO_3$ thin film along in-plane direction due to strong strain form the $SrTiO_3$ substrate [27].

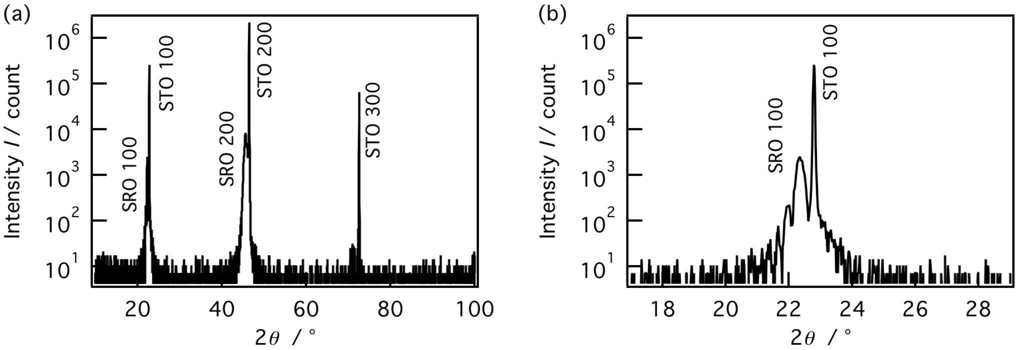

Figure 3.2 (a) Out-of-plane XRD patterns of $SrRuO_3$ epitaxial thin film. (b) Magnified of the pattern between the 2θ range between 17 and 29 °.

Figure 3.3 shows the observed XRR spectra with calculated curves of the $SrRuO_3$ thin film deposited on the $SrTiO_3$ substrate. Reflectivity spectra are plotted as a function of the scattering vector $Q_z = 4\pi\sin\theta/\lambda$ [39], where λ is the wavelength (1.541 Å) and θ is the incident angle of the X-ray. The refined parameters of thickness, density and roughness were summarized in table 3.1. The fitting was carried out with fixing the density of the $SrTiO_3$ substrate as 5.12 g cm^{-3}. A two-layer model, $SrRuO_3$ layer and $SrTiO_3$ substrate, provided the best fitting result of the observed spectra. The thickness and roughness of the $SrRuO_3$ thin film were determined as 30.7 and 0.6 nm, respectively.

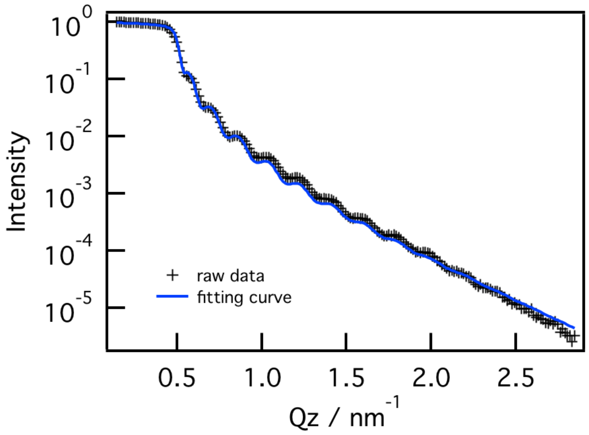

Figure 3.3 X-ray reflectivity analysis of $SrRuO_3$ thin film deposited on $SrTiO_3$ (100) substrate.

Table 3.1 XRR analysis results for the $SrRuO_3$ / $SrTiO_3$ (100) thin film.

	Thickness *l* (nm)	Density *ρ* (g cm^{-3})	Roughness *r* (nm)
$SrRuO_3$	30.7	6.33	0.6
$SrTiO_3$	-	5.10	1.2

$LiCoO_2$ epitaxial thin film was synthesized on the $SrTiO_3$ substrate, where $SrRuO_3$ buffer layer is pre-deposited. The PLD synthesis condition of $LiCoO_2$ epitaxial thin film was optimized as follows: laser energy density, 0.42 J cm^{-2}; substrate temperature, 600 °C; oxygen pressure 3.3 Pa; laser frequency, 10 Hz; distance between substrate and target, 60.6 mm. The specific condition, optimized for $SrRuO_3$ single layer, was applied for the synthesis of $SrRuO_3$ in multi-layer thin film. Figures 3.4(a) and 3.4(b) show XRD patterns of out-of-plane and its magnification between the 2θ range of 41 and 50° for $LiCoO_2$ (104) / $SrRuO_3$ thin film. The out-of-plane XRD displays a 104 reflection of $LiCoO_2$ nearby 200 diffraction line of $SrRuO_3$ at around 45°. Although, two diffraction lines are located on similar 2θ due to similar interplanar spacing, it can be distinguished from the magnified XRD patterns. Diffraction lines of the multi-layer thin film are detected on almost same positions to those of XRD patterns for the $SrRuO_3$ and $LiCoO_2$ single layers. This indicates crystal structure of the $LiCoO_2$ thin film is not varied when it is deposited on the $SrRuO_3$ layer. Figures 3.4(c) and 3.4(d) illustrate in-plane XRD patterns along [010] and [011] directions of the $SrTiO_3$ (100) substrate, respectively. The (1-1-4) and (1-20) plane of $LiCoO_2$ are identified from the in-plane XRD measurement along [010] and [011] direction of $SrTiO_3$ (100) substrate, respectively. Lattice parameter calculation of the $LiCoO_2$ thin film on the $SrRuO_3$ layer was performed with the diffraction lines identified from the out-of-plane and in-plane XRDs. The lattice parameter of the $LiCoO_2$ thin film is calculated to be a = 2.8120, c = 14.0427 Å. The lattice parameters can be compared with those of $LiCoO_2$ epitaxial thin film synthesized on $SrTiO_3$ substrate, showed a lattice parameter: a = 2.8120, c = 14.0323 Å. These parameters show that the unit cell is extended along c-axis when the $SrRuO_3$ buffer layer is introduced between the substrate and $LiCoO_2$ thin film. That only the c-axis expansion occurs would be attributed to that the lattice mismatch between the $SrRuO_3$ and the

$LiCoO_2$ thin film aligned along [104] direction extends oxygen slabs. However, the difference of the lattice parameter between the $LiCoO_2$ and $LiCoO_2$ / $SrRuO_3$ thin films is 0.0104 Å, which is a comparable value to an error range (0.0073 Å) obtained from the lattice parameter calculation for $LiCoO_2$. To confirm the symmetry of the $LiCoO_2$ synthesized on the $SrRuO_3$ layer, the ϕ scan was measured at a fixed $2\theta\chi$ value for the 1-20 reflection. Figure 3.4(e) displays the ϕ scan XRD pattern for $LiCoO_2$ on the $SrRuO_3$ / $SrTiO_3$, showing four diffraction lines with an interval of 90° despite of two-fold symmetery for 1-20 reflection. It is considered that there is a domain diverged from 1-20 reflection with 90^o. As a result, the XRD investigation reveals that the epitaxial $LiCoO_2$ thin film was successfully synthesized on the $SrRuO_3$ buffer layer without a serious structural transform.

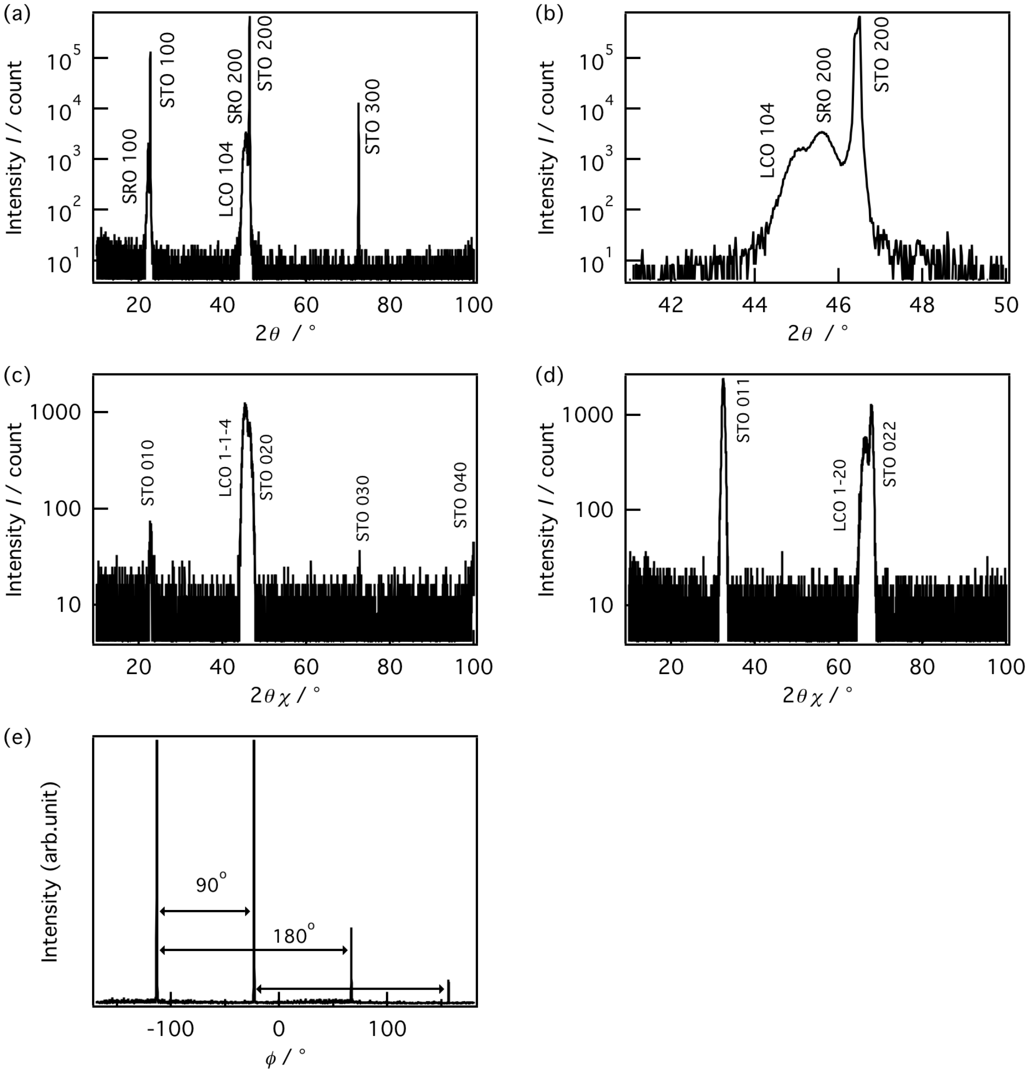

Figure 3.4 XRD patterns of (a) out-of-plane and its (b) magnification between the 2*θ* range of 41 and 50° for $LiCoO_2$ (104) / $SrRuO_3$ thin film. In-plane XRD patterns along (c) [010] and (d) [011] directions. (e) *ϕ* scan XRD of (1-20) reflection for $LiCoO_2$ on the $SrRuO_3$ / $SrTiO_3$ thin film.

Figure 3.5 displays the observed XRR spectra with calculated curves of the $LiCoO_2$ / $SrRuO_3$ thin film deposited on $SrTiO_3$ substrate. The obtained data, thickness, density and roughness for calculated curve were illustrated in table 3.2. The density of $SrTiO_3$ substrate of 5.12 g cm^{-3} was determined as an immovable parameter during the fitting process. The fitting was carried out with a three-layer model consisting of $LiCoO_2$ thin film, $SrRuO_3$ layer and $SrTiO_3$ substrate, which provided the most accurate fitting curve tailored to the observed spectra. Another unexpected surface impurity and/or interface among layers were not detected, indicating the multi-layer thin film was clearly synthesized without a serious diffusion into each other. The thicknesses of thin films were determined as 47.8 and 25.0 nm for $LiCoO_2$ and $SrRuO_3$ thin films, respectively. The densities of each film were adjusted to 5.11 g cm^{-3} for $LiCoO_2$ and 6.33 g cm^{-3} for $SrRuO_3$. These values are completely coincident with the density of the $LiCoO_2$ thin film deposited on $SrTiO_3$ substrate, illustrating compositions of $LiCoO_2$ and $SrRuO_3$ are unchanged when they are applied to multi-layer thin film. The roughness for the $LiCoO_2$ and $SrRuO_3$ are exhibited as 0.5 and 1.0 nm, respectively. In particular, the small roughness of $SrRuO_3$ layer deserves to result in $LiCoO_2$ epitaxial thin film, deposited onto the $SrRuO_3$ layer.

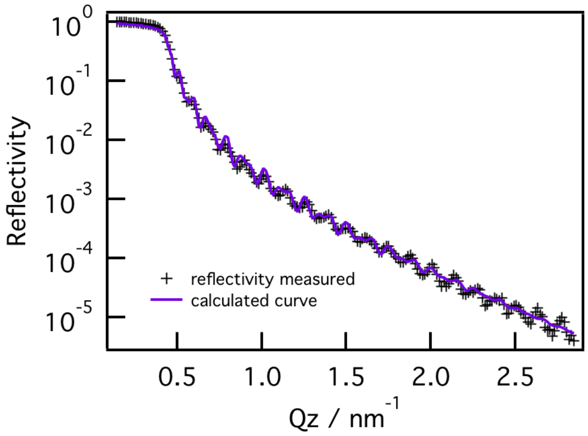

Figure 3.5 X-ray reflectivity analysis of $LiCoO_2$ / $SrRuO_3$ thin film on $SrTiO_3$ (100) substrate.

Table 3.2 XRR analysis results for the $LiCoO_2$ / $SrRuO_3$ / $SrTiO_3$ (100) thin film.

	Thickness *l* (nm)	Density *ρ* (g cm^{-3})	Roughness *r* (nm)
$LiCoO_2$	47.8	5.11	0.5
$SrRuO_3$	25.0	6.33	1.0
$SrTiO_3$	-	5.10	1.0

3.2.1.3 Electrochemical characteristics of $LiCoO_2$/$SrRuO_3$ epitaxial thin film

Electrochemical characteristics of synthesized $LiCoO_2$ / $SrRuO_3$ epitaxial thin film electrode were examined by charge-discharge measurements for two voltage window: 3 - 4.3 V and 2 - 4.3 V. Applied currents for both measurements were adjusted to 0.5 C-rate, respectively. The specific charge discharge capacities of the $LiCoO_2$ / $SrRuO_3$ thin film electrodes were obtained based on the amount of the thin films, calculated by the deposition area (0.7 mm^2), density (5.11 g cm^{-3}) and thickness (47.8 nm for the $LiCoO_2$ / $SrRuO_3$). Figures 3.6(a) and 3.6(b) show charge-discharge curves of $LiCoO_2$ / $SrRuO_3$ epitaxial thin film electrodes for voltage ranges from 3 to 4.3 V and from 2 to 4.3 V, respectively. Figure 3.6(a) indicates the second discharge capacity is 136 mAh g^{-1}, near to theoretical capacity of $LiCoO_2$ reported previously [40]. The average voltages of the $LiCoO_2$ / $SrRuO_3$ thin film are 3.93 and 3.87 V for charging and discharging process at second cycle, those values are well agreed with the potential of conventional $LiCoO_2$ [40]. Moreover, the average voltages were almost maintained during 20 cycles. This result indicates the $LiCoO_2$ / $SrRuO_3$ epitaxial thin film electrode shows conventional electrochemical characteristics with respect to the discharge capacity and reversibility in the voltage window between 3 to 4.3 V.

Figure 3.6(b) indicates a rapid capacity fading, which are attributed to the phase transition of $LiCoO_2$ from *R-3m* to *Immm* structure [41]. The layered rock salt type structure undergoes structural change when the amount of lithium is excessed over 1.0, corresponded to a voltage range below 3.0 V. The irreversibility of crystal structural changes between original rhombohedral and low voltage triclinic promoted the serious capacity fading. The $LiCoO_2$ / $SrRuO_3$ thin film electrode exhibits 162 mAh g^{-1} of discharge capacity at second cycle. This value indicates *ca.* 25 mAh g^{-1} of discharge capacities increased comparing with that in the range between 3.0 and 4.3 V. This result implies existence of additional lithium insertion into $LiCoO_2$ below 3.0 V. However, there are still other possibilities which contribute electrochemical capacity under 3.0 V since electrochemical reactions of $SrTiO_3$ substrate and $SrRuO_3$ layer under 3.0 V have not reported. In the following contents, the origin of the extra capacity is examined by investigating electrochemical properties of $SrTiO_3$ substrate and $SrRuO_3$ electronic conductor in a wide window of voltage.

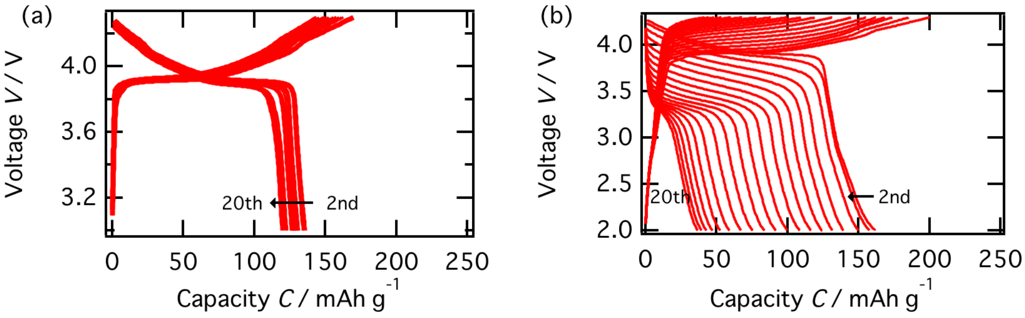

Figure 3.6 Charge-discharge curves of $LiCoO_2$ / $SrRuO_3$ thin film electrodes for measurement ranges (a) from 3.0 to 4.3 V and (b) from 2.0 to 4.3 V.

3.2.2 Characterization of $SrTiO_3$ substrate

3.2.2.1 Cyclic voltammetry of $SrTiO_3$ (100) substrate

Figure 3.7(a) shows the CV curves of the $SrTiO_3$ (100) substrate between 1.6 and 4.5 V under various scan rates. The scan rates of 0.3, 0.6, 1.2, 2.5, 5.0 and 10.0 mV s^{-1} were selected for the measurements. Obvious oxidation peaks were observed from neither anodic nor cathodic scans, indicating there are no certain electrochemical reaction behaviors of the $SrTiO_3$ (100) substrate. However, broad oxidation and reduction peaks were detected at *ca.* 3.0 and 2.5 V for anodic and cathodic scans, respectively, when the scan rates exceeded 1.2 mV s^{-1}. The currents of the indistinct peaks increase according to the increase of the scan rate. To reveal the phenomenon that dominates the charge storage in $SrTiO_3$ (100) substrate, peak currents as a function of scan rates were investigated at various potentials and calculated with the interaction formula: $i = av^b$. Figure 3.7(b) shows an example, plotting of peak currents measured at 3.0 V as a function of scan rates and its fitting curve. The b value is obtained from the calculated curve.

Likewise, the plotting and calculation were performed at various voltages. Figure 3.7(c) illustrates the *b* values obtained at various potentials between 1.6 and 4.5 V. The *b* values obtained at over 2.5 V were larger than 0.8 and approaching to 1.0, illustrating reactions over 2.5 V are mainly contributed by the surface-controlled phenomenon. On the other hand, the *b* values at 2.0 and 2.5 V were 0.612 and 0.746, respectively, which are near to 0.5. These values are indicative of the probability that reactions under the 2.5 V are affected by the bulk diffusion phenomenon. This result is coincident with the voltage of the vague reduction peak. As a result, the reactions of $SrTiO_3$ are contributed by both surface and bulk reactions. Especially, the relatively large contribution of bulk diffusion component was observed under 3 V. However, that the obvious oxidation and reduction peaks were not detected is considered to be due to similar reaction voltages between the bulk diffusion and surface-controlled reactions. Therefore, the electrochemical reaction might be covered by the surface-controlled reaction. Since it is difficult to analyze the electrochemical reactions with only these results, the charge discharge measurement was performed to reveal the contribution of the bulk diffusion phenomenon for the $SrTiO_3$ reactions.

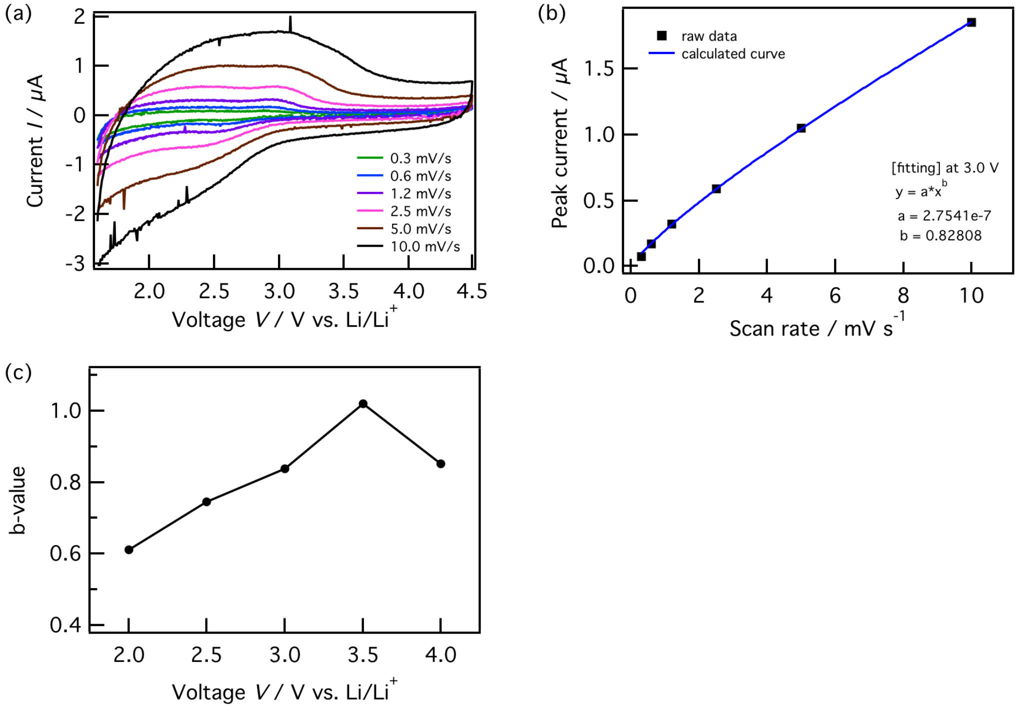

Figure 3.7 (a) Cyclic voltammograms of $SrTiO_3$ (100) substrate with varying scan rates. (b) Plotting of peak currents measured at 3.0 V as a function of scan rates and its fitting curve. (c) Variation of *b* values calculated using current value at each potential.

3.2.2.2 Charge-discharge measurement of $SrTiO_3$ (100) substrate

To confirm the capacity of redox reaction for $SrTiO_3$ substrate, charge-discharge measurement was conducted. Figures 3.8(a) and 3.8(b) show respective charge-discharge curves and their dQ/dV curves of $SrTiO_3$ (100) substrate at a range between 2.0 and 4.3 V. Reactions are displayed from second cycle since the first cycle contains a lot of side reactions that is not necessary to evaluate the reaction system. A tiny amount of capacity of 1 μAh g^{-1} was observed from the second discharge curve. The dQ/dV curves are investigated to search reversible reactions of $SrTiO_3$ substrate. First, an oxidation and reduction peaks were detected at over 4.0 V and at 2.2 V, respectively. However, these reactions disappeared rapidly according to increase of the cycle, indicating those reactions are not resulted from the $SrTiO_3$ substrate but are attributed to some side reactions in battery cell including decomposition of an electrolyte. Second, the oxidation and reduction peaks were observed at 2.9 and 2.6 V, respectively. Obvious plateaus did not appear in the charge-discharge curves and the capacity fading depending on cycles are not serious. The capacity identified in the $SrTiO_3$ substrate is supposed to be due to the contribution of the reactions at 2.9 and 2.6 V. However, the small capacity suggests that the reactions occur restrictively on the surface of $SrTiO_3$ substrate and there are hardly effects on the entire capacity of battery [42, 43].

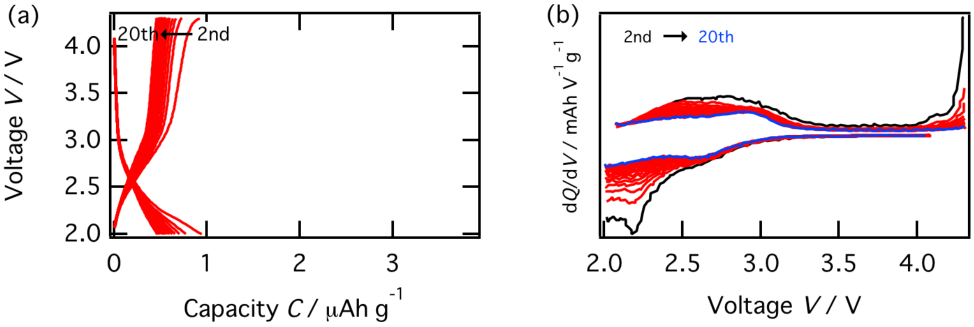

Figure 3.8 (a) Charge-discharge and (b) dQ/dV curves of $SrTiO_3$ (100) substrate at a range between 2.0 and 4.3 V.

3.2.2.3 Charge-discharge measurement of gold-coated $SrTiO_3$ (100) substrate

A $SrTiO_3$ (100) substrate coated with gold is used to epitaxial thin film batteries. To complement low electric conductivity of the semiconducting substrate and collect electrons generated on the process of electrochemical reaction, the lateral and back of $SrTiO_3$ substrate were coated with gold. Accordingly, effects of gold coating are analyzed with the electrochemical performances of the $SrTiO_3$ (100) substrate where gold is coated to a thickness of *ca.* 150 nm.. Figures 3.9(a) and 3.9(b) exhibit charge-discharge and dQ/dV curves of the $SrTiO_3$ (100) substrate where gold is deposited. The discharge capacity was observed with 7 $\mu Ah\ g^{-1}$ of small capacity at second cycle but the capacity is 7 times larger than that of the bare-$SrTiO_3$ substrate. Furthermore, the gold-coated $SrTiO_3$ substrate shows relatively apparent reaction plateaus. For examining reactions in detail, dQ/dV curves were illustrated from the charge-discharge curves. Above all, an oxidation and reduction peaks were identified at 2.0 V of cathodic scan and at over 4.0 V of anodic scan, respectively. However, these reactions shrank steeply according to cycle, which is analogous to the reactions of $SrTiO_3$ substrate without gold coating. It is expected to be due to side reactions such as decomposition of electrolyte and unidentified reactions in cell. Next, a distinct reduction and oxidation were observed at 2.5 and 3.4 V, respectively. Capacities of the reactions did not decline largely depending on increase of cycle. These reactions are regarded as main contribution to electrochemical performance of the gold-coated $SrTiO_3$ substrate. It is expected that the surface of $SrTiO_3$ substrate, which acquired enough electric conductivity by gold coating on the back and lateral sides is contributing to obvious electrochemical reactions. In a word, the gold coating facilitates the migration of electrons and stimulates the 2.5 and 3.4 V reactions of $SrTiO_3$ substrate. At last, the reduction and oxidation peaks observed at 2.6 and 2.9 V of bare-$SrTiO_3$ substrate vanished in the gold-coated $SrTiO_3$ substrate. The reactions are supposed to be screened by the obvious reactions of 2.5 and 3.4 V. Consequently, the surface reaction of $SrTiO_3$ substrate is motivated with gold coating but the capacity is too small that the effects of the $SrTiO_3$ substrate and gold can be ignored.

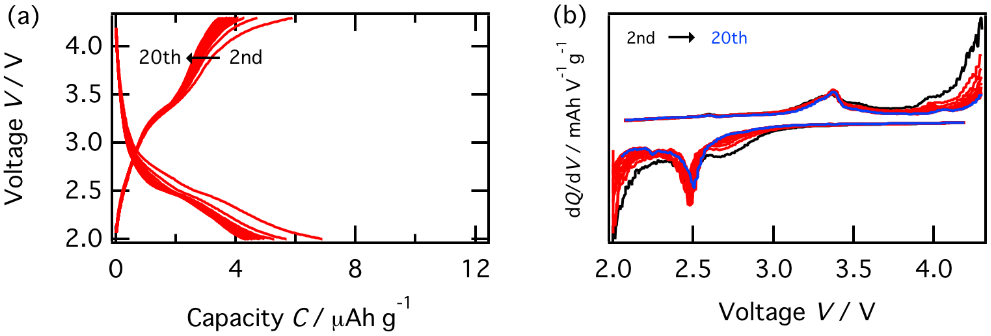

Figure 3.9 (a) Charge-discharge and (b) dQ/dV curves of $SrTiO_3$ (100) substrate where gold is coated.

3.2.3 Characterization of $SrRuO_3$ current collector

$SrRuO_3$, an electric conductive material, plays a role as a bridge between gold current collector and semiconducting electrode materials by transferring electrons generated during electrochemical reaction from electrode to current collector. In this content, charge storage phenomena and electrochemical characteristics of the $SrRuO_3$ were demonstrated.

3.2.3.1 Cyclic voltammetry of $SrRuO_3$ / $SrTiO_3$ (100) thin film

Figure 3.10(a) illustrates CV curves of $SrRuO_3$ thin film deposited on gold-coated $SrTiO_3$ (100) substrate in a range between 1.6 and 4.5 V. Scan rates applied to the CV measurements were varied from 0.1 to 10 mV s^{-1}. Apparent reaction peaks were not detected from anodic nor cathodic scans. Only a faint reduction peak is observed at around 2.5 V. At several voltages, variation of current as a function of scan rate was examined and calculated with the general formula: $i = av^b$. The b values obtained from the fitting process were depicted in figure 3.12 (b). In contrast with $SrTiO_3$ substrate, the $SrRuO_3$ showed smaller b values than 0.8 for entire potential region. In particular, 0.503 and 0.465 of b values were obtained at 2.0 and 2.5 V, which illustrates charge storage at 2.0 and 2.5 V are much strongly taken place in the bulk regions. The CV analysis suggests that the dim reduction peak of 2.5 V would implicate a bulk diffusion, which implies a reversible capacity in the $SrRuO_3$. However, since it is difficult to observe the electrochemical reaction peaks in the CV measurement, the charge discharge measurement was conducted to investigate the reversible reaction for the $SrRuO_3$.

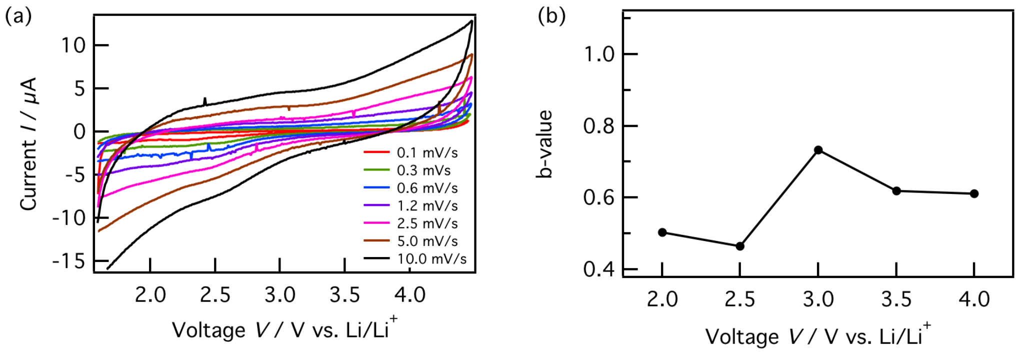

Figure 3.10 (a) Cyclic voltammogram of $SrRuO_3$ / $SrTiO_3$ (100) thin film with varying scan rates. (b) Variation of b values depending on potentials.

3.2.3.2 Charge-discharge measurement of $SrRuO_3$ / $SrTiO_3$ (100) substrate

A specific capacity of the $SrRuO_3$ was investigated by charge-discharge measurement. Figure 3.11(a) shows charge-discharge curves of the $SrRuO_3$ thin film deposited on gold-coated $SrTiO_3$ (100) substrate in a range between 2.0 and 4.3 V. The cycle curves were represented from the second measurement to exclude the first cycle that incorporates a plenty of unnecessary side reactions. As expected in CV measurement, obvious plateaus were not observed. On the other hand, a considerable discharge capacity of 34 mAh g^{-1} was obtained at the second cycle. Figure 3.11(b) exhibits dQ/dV curves to investigate reversible reactions of $SrRuO_3$ thin film. Oxidation peaks at 3.9 and 4.3 V, and a reduction peak at 2.0 V stand out with strong intensity but these peaks largely decreased upon cycling. These reactions are considered to be due to side reactions such as decomposition of electrolyte and unidentified reactions in cell. Second, weak reduction and oxidation peaks were observed at 2.6 V of cathodic scan and 2.9 V of anodic scan, respectively. These reactions are coincident with electrochemical reactions identified in the dQ/dV curves of the bare-$SrTiO_3$ substrate. However, a slight capacity fading was shown and the reaction peaks were not obvious. Finally, the obvious reduction and oxidation detected at 2.5 and 3.4 V of the gold-coated $SrTiO_3$ substrate completely disappeared when the $SrRuO_3$ is deposited on the $SrTiO_3$ substrate. This is because the $SrRuO_3$ thin film is covering the surface of the $SrTiO_3$ substrate, resulting in restriction of the surface reaction of the $SrTiO_3$ substrate. As a result, reaction plateaus of the $SrRuO_3$ were not identified even at low voltage of less than 3 V. However, the *b* values of near 0.5 for all potentials and the considerable capacity of *ca.* 30 mAh g^{-1} with reversibility suggest that a slight amount of lithium can be stored on the a few nanometers of surface of the $SrRuO_3$ thin film under 3 V. Although the reactions of $SrTiO_3$ substrate show scarce capacity contribution under 3 V, the $SrRuO_3$ surface reactions reveal the considerable capacity that can not be ignored. Therefore, the amount of capacity for $SrRuO_3$ should be subtracted when the capacities of epitaxial thin film electrode are investigated under 3 V.

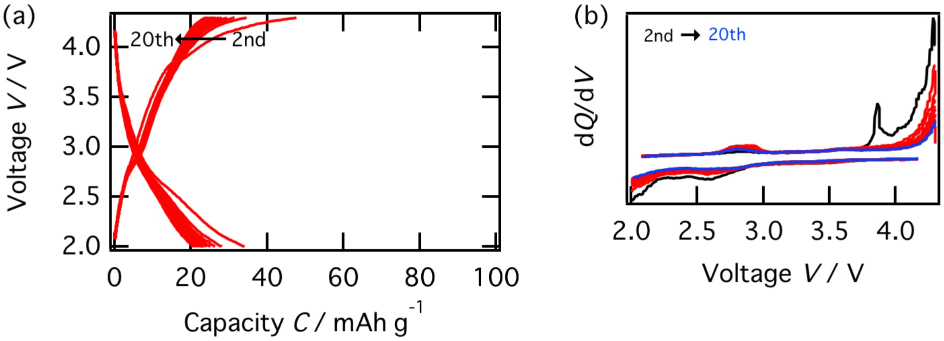

Figure 3.11 (a) Charge-discharge and (b) dQ/dV curves of $SrRuO_3$ / $SrTiO_3$ (100) thin film at a range between 2.0 and 4.3 V.

3.3 Conclusion

Epitaxial $LiCoO_2$ thin films were prepared on the $SrTiO_3$ (100) substrate and $SrRuO_3$ / $SrTiO_3$ (100) substrate, in which gold is deposited on the backside of $SrTiO_3$ (100) substrate. Thin film XRD and XRR demonstrated an growth of $LiCoO_2$ (104) with a highly oriented and flat surface of the $SrRuO_3$ buffer layer, which deserves to provide an appropriate bottom layer for epitaxial growth of $LiCoO_2$ without structural distortion and degradation. Reaction systems and electrochemical performances for constituent of battery, $SrRuO_3$ electric conductor, $SrTiO_3$ substrate and gold current collector, were examined using CV and charge-discharge test in order to reveal an origin of extra capacity for $LiCoO_2$ / $SrRuO_3$ / $SrTiO_3$ in a wide range between 2.0 and 4.3 V. Although $SrTiO_3$ substrate shows a bulk diffusion below 3.0 V and the reaction is stimulated by gold, there are few capacities affecting performance of battery. Deposition of a $SrRuO_3$ buffer layer restrains the surface reaction of $SrTiO_3$ substrate but the $SrRuO_3$ itself indicates a reaction system thoroughly dominated by bulk diffusion phenomenon in a range below 3.0 V with a considerable capacity of *ca.* 30 mAh g^{-1}. To conclude, the capacity contribution of $SrRuO_3$ should be considered when a charge-discharge measurement is performed at below 3.0 V for an electrode where the $SrRuO_3$ is introduced as buffer layer.

Reference

[1] M. Hirayama, K. Sakamoto, T. Hiraide, D. Mori, A. Yamada, R. Kanno, N. Sonoyama, K. Tamura, J. Mizuki, Electrochim. Acta, 53 (2007) 871-881.

[2] K. Sakamoto, H. Konishi, N. Sonoyama, A. Yamada, K. Tamura, J. Mizuki, R. Kanno, J. Power Sources, 174 (2007) 678-682.

[3] M. Hirayama, H. Ido, K. Kim, W. Cho, K. Tamura, J. Mizuki, R. Kanno, J. Am. Chem. Soc., 132 (2010) 15268-15276.

[4] M. Hirayama, M. Yonemura, K. Suzuki, N. Torikai, H. Smith, E. Watkinsand, J. Majewski, R. Kanno, Electrochemistry, 78 (2010) 413-415.

[5] H. Konishi, K. Suzuki, S. Taminato, K. Kim, Y. Zheng, S. Kim, J. Lim, M. Hirayama, J.-Y. Son, Y. Cui, R. Kanno, J. Power Sources, 269 (2014) 293-298.

[6] S. Taminato, M. Hirayama, K. Suzuki, K. Kim, Y. Zheng, K. Tamura, J.i. Mizuki, R. Kanno, J. Mater. Chem. A, 2 (2014) 17875-17882.

[7] K. Suzuki, K. Kim, S. Taminato, M. Hirayama, R. Kanno, J. Power Sources, 226 (2013) 340-345.

[8] H. Konishi, K. Suzuki, S. Taminato, K. Kim, S. Kim, J. Lim, M. Hirayama, R. Kanno, J. Power Sources, 246 (2014) 365-370.

[9] P. Balaya, H. Li, L. Kienle, J. Maier, Adv. Funct. Mater., 13 (2003) 621-625.

[10] W.J.H. Borghols, M. Wagemaker, U. Lafont, E.M. Kelder, F.M. Mulder, J. Am. Chem. Soc., 131 (2009) 17786-17792.

[11] M. Wagemaker, F.M. Mulder, Acc. Chem. Res., (2012).

[12] J.M. Tarascon, M. Armand, Nature, 414 (2001) 359-367.

[13] A.S. Arico, P. Bruce, B. Scrosati, J.M. Tarascon, W. Van Schalkwijk, Nat Mater, 4 (2005) 366-377.

[14] N.S. Choi, Z.H. Chen, S.A. Freunberger, X.L. Ji, Y.K. Sun, K. Amine, G. Yushin, L.F. Nazar, J. Cho, P.G. Bruce, Angew Chem Int Edit, 51 (2012) 9994-10024.

[15] J.W. Fergus, J Power Sources, 195 (2010) 939-954.

[16] B. Scrosati, J. Garche, J Power Sources, 195 (2010) 2419-2430.

[17] M.K. Song, S. Park, F.M. Alamgir, J. Cho, M.L. Liu, Mat Sci Eng R, 72 (2011) 203-252.

[18] K. Edstrom, T. Gustafsson, J.O. Thomas, Electrochim. Acta, 50 (2004) 397-403.

[19] P. Lu, S.J. Harris, Electrochem Commun, 13 (2011) 1035-1037.

[20] M. Hirayama, N. Sonoyama, T. Abe, M. Minoura, M. Ito, D. Mori, A. Yamada, R. Kanno, T. Terashima, M. Takano, K. Tamura, J.i. Mizuki, J Power Sources, 168 (2007) 493-500.

[21] K. Sakamoto, M. Hirayama, H. Konishi, N. Sonoyama, N. Dupre, D. Guyomard, K. Tamura, J. Mizuki, R. Kanno, PCCP, 12 (2010) 3815-3823.

[22] Y. Zheng, S. Taminato, Y. Xu, K. Suzuki, K. Kim, M. Hirayama, R. Kanno, J Power Sources, 208 (2012) 447-451.

[23] S. Taminato, M. Hirayama, K. Suzuki, K. Kim, Y.M. Zheng, K. Tamura, J. Mizuki, R. Kanno, J Mater Chem A, 2 (2014) 17875-17882.

[24] M. Hirayama, K. Kim, T. Toujigamori, W. Cho, R. Kanno, Dalton T, 40 (2011) 2882-2887.

[25] H. Konishi, K. Suzuki, S. Taminato, K. Kim, S. Kim, J. Lim, M. Hirayama, R. Kanno, J Power Sources, 246 (2014) 365-370.

[26] S. Kim, M. Hirayama, K. Suzuki, R. Kanno, Solid State Ionics, 262 (2014) 578-581.

[27] K. Suzuki, K. Kim, S. Taminato, M. Hirayama, R. Kanno, J Power Sources, 226 (2013) 340-345.

[28] M. Komo, A. Hagiwara, S. Taminato, M. Hirayama, R. Kanno, Electrochemistry, 80 (2012) 834-838.

[29] M. Okubo, E. Hosono, J. Kim, M. Enomoto, N. Kojima, T. Kudo, H.S. Zhou, I. Honma, J. Am. Chem. Soc., 129 (2007) 7444-7452.

[30] C. Delmas, M. Maccario, L. Croguennec, F. Le Cras, F. Weill, Nat Mater, 7 (2008) 665-671.

[31] G. Kobayashi, S.I. Nishimura, M.S. Park, R. Kanno, M. Yashima, T. Ida, A. Yamada, Adv. Funct. Mater., 19 (2009) 395-403.

[32] A. Van der Ven, M. Wagemaker, Electrochem. Commun., 11 (2009) 881-884.

[33] K. Kim, Ph.D. dissertation, Tokyo Insitute of Technology, (2012).

[34] R. Koksbang, J. Barker, M.Y. Saidi, K. West, B. ZachauChristiansen, S. Skaarup, Solid State Ionics, 83 (1996) 151-157.

[35] A. Ito, H. Masumoto, T. Goto, S. Sato, J. Eur. Ceram. Soc., 30 (2010) 435-440.

[36] N. Kato, A.R. Lang, Acta Crystallogr, 12 (1959) 787.

[37] D. Rubi, A.H.G. Vlooswijk, B. Noheda, Thin Solid Films, 517 (2009) 1904-1907.

[38] K.J. Choi, S.H. Baek, H.W. Jang, L.J. Belenky, M. Lyubchenko, C.B. Eom, Adv Mater, 22 (2010) 759-762.

[39] B. Jerliu, L. Dorrer, E. Huger, G. Borchardt, R. Steitz, U. Geckle, V. Oberst, M. Bruns, O. Schneider, H. Schmidt, Phys Chem Chem Phys, 15 (2013) 7777-7784.

[40] C.J. Patridge, C.T. Love, K.E. Swider-Lyons, M.E. Twigg, D.E. Ramaker, J Solid State Chem, 203 (2013) 134-144.

[41] K. Kang, C.H. Chen, B.J. Hwang, G. Ceder, Chem Mater, 16 (2004) 2685-2690.

[42] P. Blennow, K.K. Hansen, L.R. Wallenberg, M. Mogensen, Solid State Ionics, 180 (2009) 63.

[43] E.E. Mori, M. Kamaratos, J Phys-Condens Mat, 19 (2007).

Chapter 4: Novel Li-Co-Mn-O epitaxial thin-film electrode using layer-by-layer deposition process

4.1 Introduction

Lithium batteries are now widely used as power sources for electric vehicles (EVs), plug in hybrid vehicles (PHEV) and portable electric devices [1]. However, the performance of the present lithium batteries still can not satisfy the strong requirements for energy sources; the improvements of power characteristics, safety, energy density and reliability are agendas to be solved. Since the electrode is one of the important components affecting lithium battery performance, many studies have focused on the material used for the electrodes [2-5]. The electrochemical performance of the electrode is strongly dependent on the crystal structure and composition of the material used. This is because phenomena of lithium migration along diffusion pathways, phase transition due change of lithium amount and redox reactions with transition metals mainly take place with charge-discharge reaction, and they are largely influenced by the crystal structure and composition [6-8]. Therefore, a variety of synthesis techniques have been used in an attempt to develop novel electrode materials with controlled compositions and crystal structures, including solid-state reaction, sol-gel, hydrothermal and co-precipitation methods [9-16]. However, conventional synthesis methods have limitations in that the structural characteristics of the material are dominated by the Gibbs phase rule, and depend on the ionic radius of the constituent elements and the thermodynamic stability of the structure. Therefore, we have been developing a new approach for fabricating lithium battery electrodes based on layer-by-layer process using pulsed laser deposition (PLD). The layer-by-layer deposition process is progressed by stacking several materials of different crystal structure and/or composition continuously on single crystal substrate. By varying the materials used and the stacking patterns, films with complex crystal structures and compositions can be fabricated. Such a layer-by-layer approach has been applied to magnetic, dielectric and superconducting materials, allowing the formation of new structures such as superlattice, graded and metastable structures, whose properties were drastically different to those of the constituent materials [17-25]. Since this method allows a large number of deposition conditions to be varied, such as the number of layers and repetitions, the layer thicknesses, the stacking sequence, and the types of constituent materials (including conventional electrode materials), it is highly promising for developing novel electrode materials for lithium batteries.

In previous studies, PLD was used to deposit a series of epitaxial thin films for electrodes and solid electrolytes. These films were used to investigate reactions at the interface between an electrode and a liquid electrolyte, nanoscale effects, anisotropic lithium diffusion in the crystal structure and surface coating effects [6, 26-28]. In the present study, layer-by-layer process with PLD was performed on $SrTiO_3$ (111) substrates using two of these materials: $LiCoO_2$ with a layered rock-salt type structure, and $LiMn_2O_4$ with a cubic spinel type structure. For comparison, a single-step Li-Co-Mn-O and a $LiMn_2O_4$ films with the spinel type structure were also fabricated. The crystal structure, electronic structure, cation distribution and charge-discharge characteristics of the different films were investigated using X-ray diffraction (XRD), X-ray absorption spectroscopy (XAS), high resolution scanning transmission electron microscope (HR-STEM) and electrochemical measurements.

4.2 Results and discussion

4.2.1 Characterization of target materials for PLD

4.2.1.1 Characterization of the $LiMn_2O_4$ target

Figure 4.1 shows XRD patterns of $Li_{1.2}Mn_2O_4$ target for PLD. The diffraction peaks are clearly indexed as $LiMn_2O_4$ of a cubic spinel structure (space group: *Fd*-3*m*). The lattice parameter was calculated from the identified peaks of $Li_{1.2}Mn_2O_4$ and obtained as a = 8.2440 Å. The calculated value is comparable to that of reported $LiMn_2O_4$ (ICSD No. 89985): a = 8.2483 Å. Small peaks, illustrated by asterisks, are well agreed with phases of Li_2MnO_3 (ICSD No. 166861), which is ascribed to the 20 % excess lithium composition of starting materials. These results verify that $LiMn_2O_4$ target with lithium excess composition was successfully synthesized. The lithium rich $LiMn_2O_4$ target deserves to compensate a lithium loss during the PLD process.

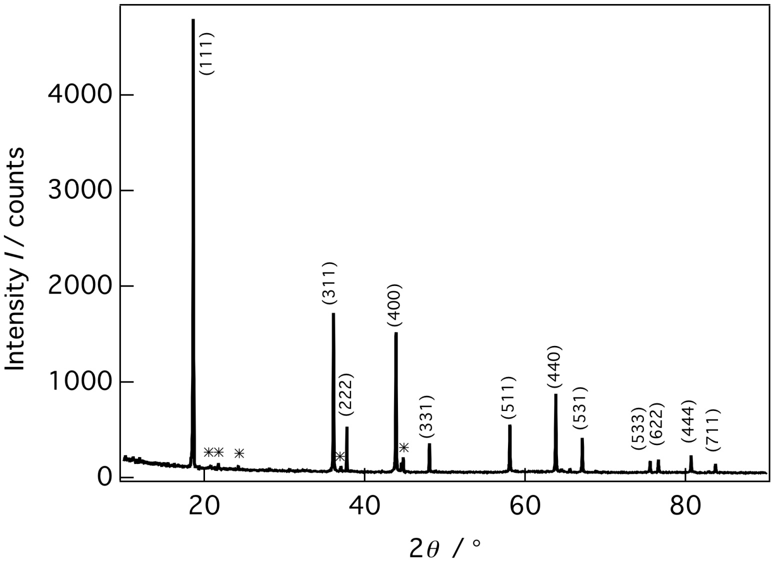

Figure 4.1 XRD patterns of $LiMn_2O_4$ target for PLD. Asterisks indicate impurity phase of Li_2MnO_3.

4.2.1.2 Characterization of the $Li_{0.92}Co_{0.65}Mn_{1.35}O_4$ target

The composition of 1-step film was adjusted to that of 2-step film investigated by inductively coupled plasma mass spectrometry (ICP-MS). 1-step film target for PLD was prepared with lithium excess composition of starting materials to compensate a lithium loss during PLD process. ICP-MS analysis demonstrated the Li:Co:Mn molar ratio for the 1-step film target to be 1.087:0.522:1. Figure 4.2 shows XRD patterns of the $Li_{1.4}Co_{0.65}Mn_{1.35}O_4$ target for PLD of 1-step film. The diffraction peaks are indexed based on a cubic spinel structure (space group: *Fd*-3*m*) since the diffraction patterns are well agreed with that of $LiMn_2O_4$, known as conventional spinel structure. The lattice parameter was evaluated from the all detected peaks of $Li_{1.4}Co_{0.65}Mn_{1.35}O_4$ and calculated as a = 8.0911 Å. The lattice constant is comparable to that of a reported $LiCo_{0.66}Mn_{1.34}O_4$: a = 8.10 Å [29]. Impurity phase, indicated by asterisk, is detected at 20.8° with a small peak, which corresponds to Li_2MnO_3 (ICSD No. 166861). The impurity phase occurred due to the 40 % excess lithium composition of starting material. These results show that $Li_{0.92}Co_{0.65}Mn_{1.35}O_4$ target with lithium rich composition was successfully prepared.

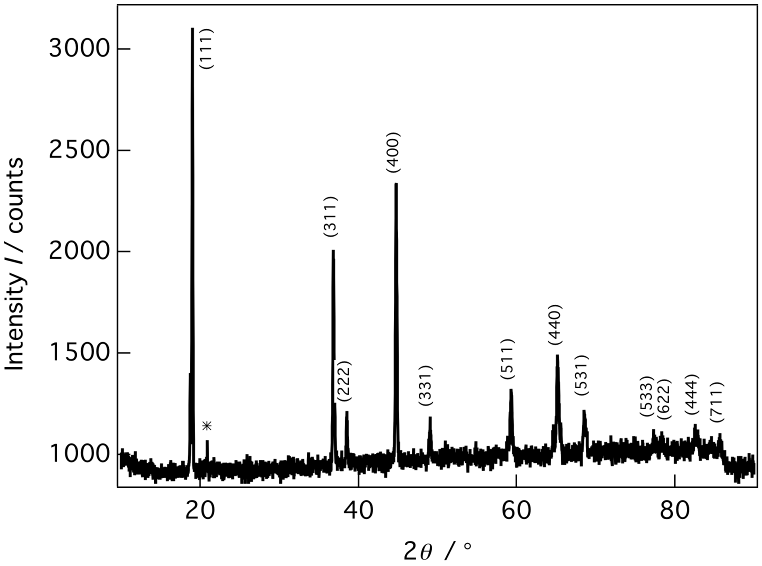

Figure 4.2 XRD patterns of $Li_{0.92}Co_{0.65}Mn_{1.35}O_4$ target for PLD. Asterisk indicates impurity phase of Li_2MnO_3.

4.2.2 Characterization of each layer for layer-by-layer deposition

Layer-by-layer deposition was progressed with $LiMn_2O_4$ and $LiCoO_2$ epitaxial thin films. For comparison with a new electrode synthesized by layer-by-layer deposition process, characteristics of each material film were analyzed. The respective $LiMn_2O_4$ and $LiCoO_2$ thin films were deposited on $SrTiO_3$ (111) substrate where $SrRuO_3$ current collector is pre-deposited.

4.2.2.1 Characterization of the epitaxial $LiMn_2O_4$ thin film

Figures 4.3(a) and 4.3(b) show XRD patterns for the $LiMn_2O_4$ / $SrRuO_3$ thin film, out-of-plane and in-plane along [1-10] direction of $SrTiO_3$ (111) substrate. Indexing of the $LiMn_2O_4$ thin film was performed based on cubic spinel structure with space group of *Fd*-3*m*. The out-of-plane XRD displays 111, 222, 333 and 444 diffraction lines, which indicates the thin film has a

(111) orientation on the $SrTiO_3$ (111). The $SrRuO_3$ buffer layer is confirmed as a 222 diffraction peak at 85° in the out-of-plane patterns, which has a (111) orientation based on a pseudo cubic structure: space group *Pm*-3*m* [30]. In the in-plane XRD pattern, the diffraction peak was indexed as 4-40, showing a (1-10) orientation of the $LiMn_2O_4$ thin film along the [1-10] direction of the $SrTiO_3$ (111) substrate. Figure 4.3(c) shows the rotational symmetry of the crystal structure identified with a ϕ scan at a fixed $2\theta\chi$ value for 4-40 diffraction line. A six-fold symmetry along [111] direction was confirmed by six diffraction peaks at intervals of 60°. The XRD analysis demonstrates the epitaxial $LiMn_2O_4$ films are successfully synthesized on the $SrRuO_3$ buffer layer [31]. The lattice parameter of the $LiMn_2O_4$ thin film is calculated from the detected diffraction peaks in out-of-plane and in-plane XRD. The lattice parameter was obtained to be 8.2638 Å, which is comparable value of the conventional $LiMn_2O_4$ spinel structure [32].

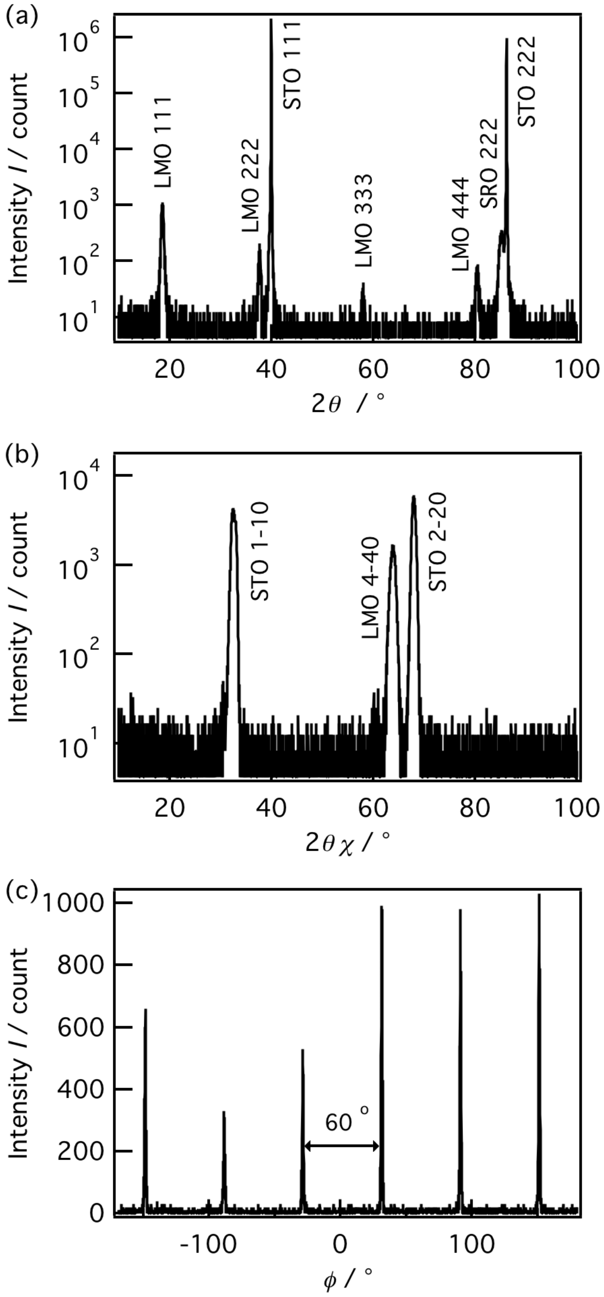

Figure 4.3 XRD patterns for the $LiMn_2O_4$ / $SrRuO_3$ epitaxial thin film, (a) out-of-plane and (b) in-plane along [1-10] direction of $SrTiO_3$ (111) substrate. (c) ϕ scan XRD pattern of 4-40 reflection of the $LiMn_2O_4$.

Figure 4.4 shows the observed XRR spectra and its calculated curve for the $LiMn_2O_4$ / $SrRuO_3$ epitaxial thin film. The refined parameters, thickness, density and roughness (R_a), for the each layer were exhibited in table 4.1. The density of $SrTiO_3$ substrate was fixed as 5.12 g cm^{-3} for the fitting process. The fitting was performed with a four-layer model including surface layer/$LiMn_2O_4$/$SrRuO_3$/$SrTiO_3$ substrate, which provided the best fitting curve for the observed spectrum. The surface impurity layer having a density of 2.11 g cm^{-3} is expected to be Li_2CO_3 and/or LiOH, attributed to a side reaction between the film surface and ambient air [33-35]. The thicknesses of the $LiMn_2O_4$ and $SrRuO_3$ thin films were determined as 21.0 and 25.4 nm, respectively. The thickness of $SrRuO_3$ thin film is a sufficient thickness that deserves to support electric conduction between the $LiMn_2O_4$ electrode and $SrTiO_3$ substrate. Furthermore, the determined densities of $LiMn_2O_4$ and $SrRuO_3$ were well coincident with those of conventional $LiMn_2O_4$ and $SrRuO_3$, indicating the thin films were synthesized without compositional distortion.

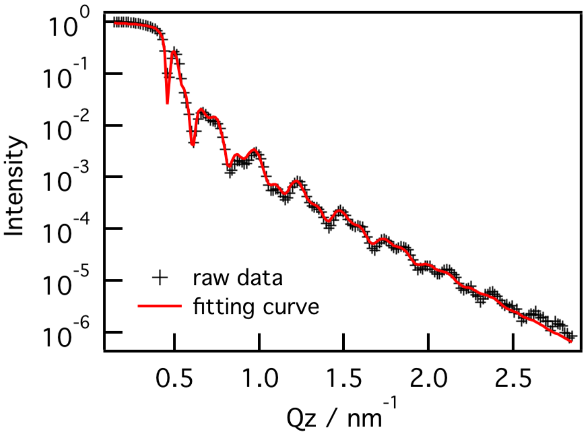

Figure 4.4 XRR spectrum with a fitting curve for $LiMn_2O_4$ / $SrRuO_3$ / $SrTiO_3$ (111) substrate.

Table 4.1 XRR analysis results for the $LiMn_2O_4$ / $SrRuO_3$ / $SrTiO_3$ (111) thin film.

	Thickness *l* (nm)	Density ρ (g cm^{-3})	Roughness *r* (nm)
Surface layer	0.9	2.11	0.5
$LiMn_2O_4$	21.0	4.30	0.6
$SrRuO_3$	25.4	6.33	1.2
$SrTiO_3$	-	5.12	1.2

4.2.2.2 Characterization of the epitaxial $LiCoO_2$ thin film

Figures 4.5(a) and 4.5(b) show out-of-plane and in-plane XRD patterns for the $LiCoO_2$ / $SrRuO_3$ epitaxial thin film on the $SrTiO_3$ (111) substrate. Indexing for the $LiCoO_2$ thin film was carried out based on the layered rock salt structure with space group of R-3m. The out-of-plane XRD shows 003, 006, 009, 0012 diffraction lines, indicating the $LiCoO_2$ thin film was grown with a (001) orientation. The $SrRuO_3$ thin film is identified from 222 diffraction peak detected at around 85°. In-plane XRD was measured along the [1-10] direction of the $SrTiO_3$ (111) substrate. A 110 diffraction line of $LiCoO_2$ is observed, which indicates the $LiCoO_2$ has a (110) orientation along the [1-10] direction of the substrate. The rotational symmetry of the crystal structure was investigated by the ϕ scan with fixing a $2\theta\chi$ value for the 110 reflection. Figure 4.5(c) shows the ϕ scan XRD pattern for $LiCoO_2$ thin film on the $SrRuO_3$ / $SrTiO_3$, illustrating six diffraction lines with an interval of 60°. Although the layered rock salt type structure of $LiCoO_2$ has two-fold rotation symmetry, the six diffraction peaks of ϕ scan XRD pattern are ascribed to three different orientations with two-fold symmetry. Among the six diffraction lines, two diffraction lines with an interval of 180° correspond to the 110 reflection. However, the other two pairs of diffraction lines with two-fold symmetry are caused by 2-10 and 1-20 reflections, respectively. This is because the 110, 2-10 and 1-20 reflections of $LiCoO_2$ are detected at comparable $2\theta\chi$ values. As a result, the XRD analysis indicates that the epitaxial $LiCoO_2$ thin film with layered rock salt structure was successfully synthesized.

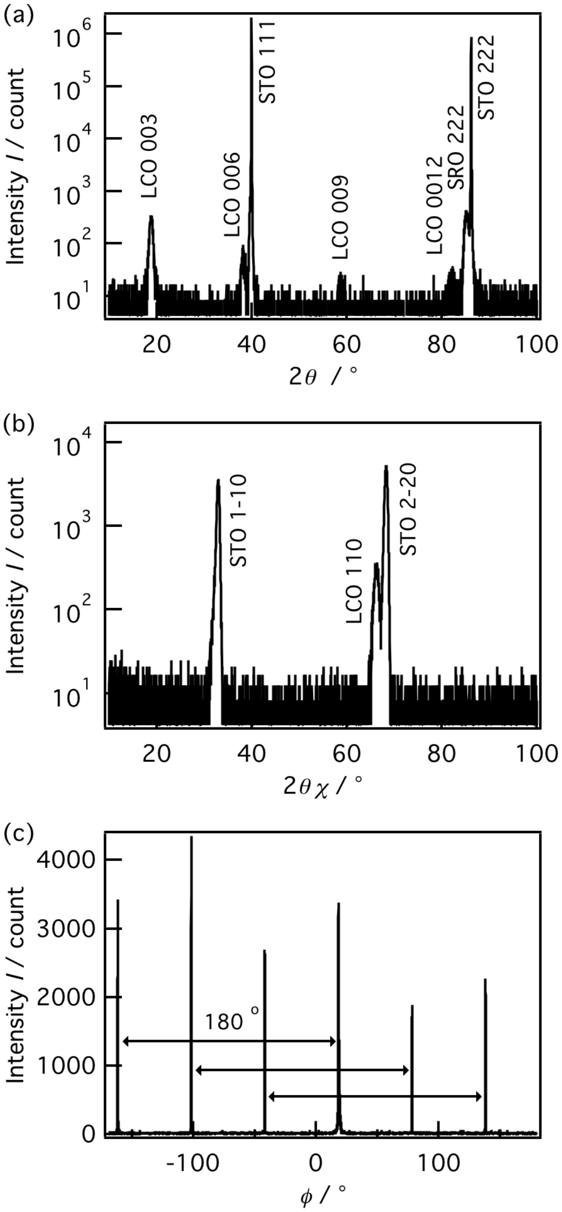

Figure 4.5 XRD patterns for the $LiCoO_2$ / $SrRuO_3$ epitaxial thin film, (a) out-of-plane and (b) in-plane along [1-10] direction of $SrTiO_3$ (111) substrate. (c) ϕ scan XRD pattern of 110 reflection of the $LiCoO_2$.

Figure 4.6 shows the observed XRR spectrum and calculated curve for the $LiCoO_2$ / $SrRuO_3$ epitaxial thin film deposited on the $SrTiO_3$ (111) substrate. The obtained film information including thickness, density and roughness (R_a) are contained on table 4.2. A four-layer model, surface layer/$LiCoO_2$/$SrRuO_3$/$SrTiO_3$ was applied for the fitting, which represents the best fitting curve. The surface layer with a density of 2.11 g cm^{-3} is supposed to be Li_2CO_3 and/or LiOH, which is created on surface of the thin film by the side reaction to ambient air [33-35]. The thicknesses were determined as 12.4 and 20.6 nm for $LiCoO_2$ and $SrRuO_3$ thin films, respectively. The determined density of $LiCoO_2$ indicates the $LiCoO_2$ with layered rock salt structure was well synthesized.

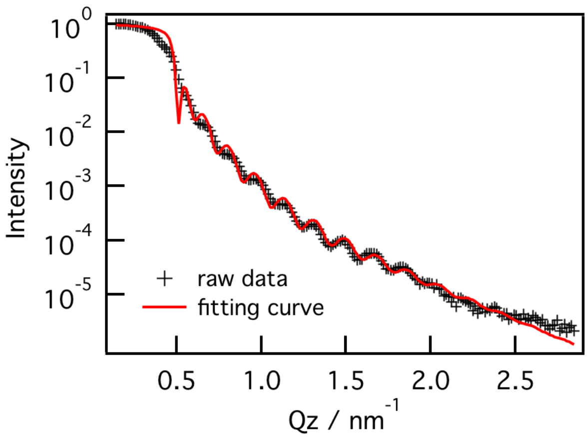

Figure 4.6 XRR spectrum with a fitting curve for $LiCoO_2$ / $SrRuO_3$ / $SrTiO_3$ (111) substrate.

Table 4.2 XRR analysis results for the $LiCoO_2$ / $SrRuO_3$ / $SrTiO_3$ (111) thin film.

	Thickness l (nm)	Density ρ (g cm^{-3})	Roughness r (nm)
Surface layer	1.6	2.11	1.5
$LiCoO_2$	12.4	5.10	0.5
$SrRuO_3$	20.6	6.33	5.0
$SrTiO_3$	-	5.12	1.1

4.2.3 Layer-by-layer deposition effects on composition and element distribution

$LiMn_2O_4$ and $LiCoO_2$ were deposited on the $SrRuO_3$ / $SrTiO_3$ (111) using layer-by-layer process. Although the $LiMn_2O_4$ and $LiCoO_2$ have different crystal structures and electrochemical properties each other, the two materials were supposed to be suitable ingredients that can form a novel structure through the layer-by-layer deposition since both crystal structures are constituted by identical oxygen arrays of cubic closed packing. In the previous part, the XRR analysis revealed that the $LiMn_2O_4$ deposited on $SrRuO_3$ has a flat interface in comparison with that of the $LiCoO_2$ synthesized on the $SrRuO_3$. Therefore, the $LiMn_2O_4$ is firstly deposited on the $SrRuO_3$ then the $LiCoO_2$ is deposited on the $LiMn_2O_4$. It is examined that a composition, element distribution and structure of the 2-step film synthesized by layer-by-layer process.

4.2.3.1 HR-TEM measurement for 2-step film

Figure 4.7(a) shows a cross-sectional HAADF-STEM image of the entire 2-step film. Although two separate layers are deposited, there is no significant contrast change or any obvious interface. Figure 4.7(b) shows a Fourier transform of the lattice image in Fig. 4.7(a); the resulting diffraction pattern indicates that the entire film has a cubic crystal structure. Therefore, the original layered rock-salt structure of the $LiCoO_2$ becomes transformed to a cubic structure when it is deposited on $LiMn_2O_4$.

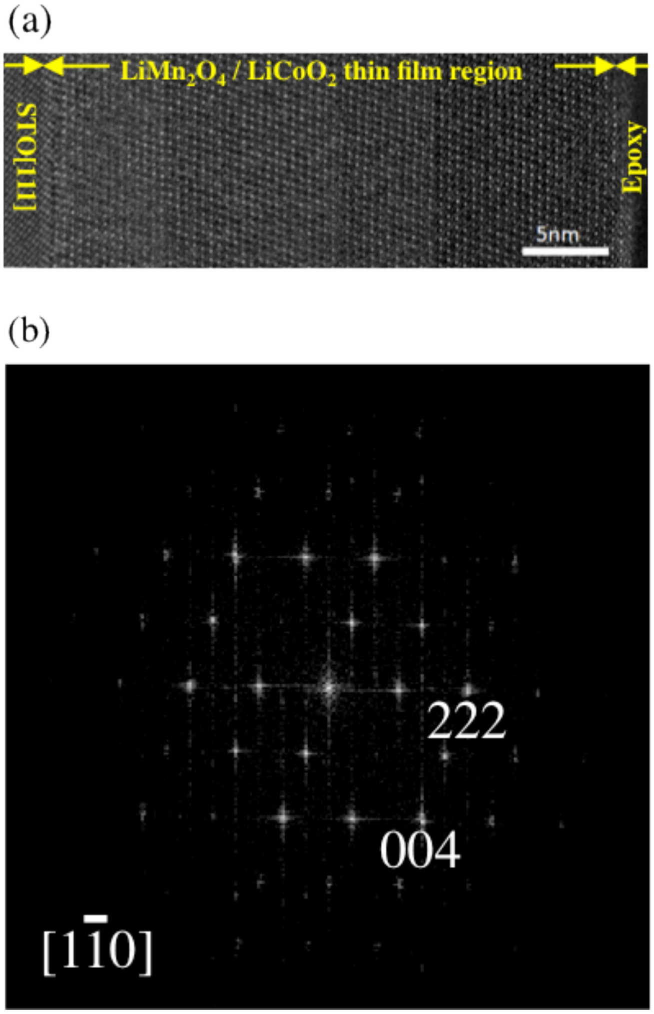

Figure 4.7 (a) Cross-sectional HAADF image of entire 2-step film, observed along [1-10] substrate direction. (b) Fast Fourier transform of the HAADF image in (a).

4.2.3.2 EELS measurement for 2-step film

Figure 4.8 shows the results of cross-sectional EELS mapping for the 2-step film. For each element, the brightness indicates the local concentration of that element. It can be seen that Co, Mn and O are uniformly distributed throughout the entire thin film. A strong O signal is also seen from the $SrTiO_3$ substrate. The above results indicate that that the 2-step film has a homogeneous Li-Co-Mn-O single-phase composition, in addition to a cubic crystal structure. It is considered that during deposition, the $LiCoO_2$ and $LiMn_2O_4$ react and atomic interdiffusion occurs. Same phenomenon is also expected to be the case for the 4-step thin film because the layers are thinner and should react more easily.

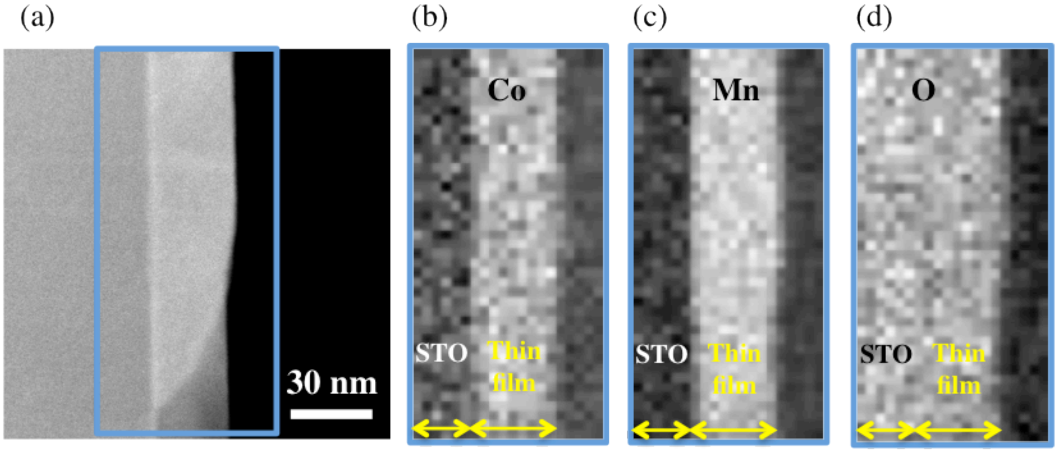

Figure 4.8 (a) TEM image of EELS mapping region in 2-step film. Corresponding EELS mapping results for (b) Co, (c) Mn and (d) O.

4.2.3.3 HAXPES measurement for 2-step film

Hard X-ray photoelectron spectroscopy (HAXPES) was performed to evaluate the electronic structures of thin film electrodes using a hemispherical electron analyzer VG-SIENTA R-4000 installed on the in-vacuum undulator beamline BL46XU at SPring-8. The X-rays were monochromated by a Si(111) double crystal system. The X-ray spot size was 20 mm x 2 mm on the surface of the samples. An X-ray energy of 7940 eV was selected to enhance its prove depth, which is determined by the IMFP from the surface of the thin films. The larger energy of the incident X-ray can provide the larger kinetic energy of photoelectron, which increases IMFP of the electrons within the thin films. In addition, a prove depth can be controlled by regulating the photoelectron take-off-angle (TOA) from the surface of the thin films to the analyzer [36]. The TOA of 80° was selected to obtain electronic structural information of whole region for the thin films. The spectra were recorded under a pressure of 2.0×10^{-5} Pa. At first, the HAXPES measurements were performed to investigate the electronic structure of wide energy regions in the kinetic energy from 7000 to 7940 eV. After that, photoelectron spectra of Co 3s and Mn 3s core levels were investigated to determine oxidation state of Co and Mn in the 2-step thin film. The core level spectra were recorded for 7 times, and then merged to obtain enhanced signals for detailed analysis. The obtained spectra were analyzed by software CasaXPS using the calibrated binding energy based on the Au $4f_{7/2}$ level at 84.0 eV. A background of each spectrum was subtracted by Shirley method.

The electronic structure analysis provides information with regard to oxidation state of cobalt and manganese, which assists to determine the composition and oxygen deficiency of the 2-step film. Figure 4.9 displays Co 3s and Mn 3s XPS core peaks for as-prepared 2-step film. 3s core peaks of transition metals *M* are susceptible to a metal spin state. When the 3d spin is not zero, the energy splitting occurs in *M* 3s core peak due to an exchange interaction of 3s and 3d electrons. The energy splitting phenomena results in 3s core peaks separated into two peaks [37, 38]. Therefore, the 3s core level can be a significant criterion to evaluate the electronic structure of transition metals. The Mn 3s core peaks are identified at 88.85 and 84.12 eV of binding energy with energy splitting, which is attributed to electron exchange interaction. The gab of energy splitting is proportional to the number of unpaired electrons in the d orbital of manganese [38]. The energy split gap of Mn 3s measured in the 2-step film is 4.73 eV, which indicates the oxidation state of manganese could be determined as 3.8^+. The Co 3s core level exhibits a main peak at 102.48 eV and satellite peaks in a region from 106 to 115 eV of binding energy. In contrast with the Mn 3s core level, the main peak of Co 3s core level does not show obvious energy splitting, which explains the low spin configuration of cobalt in 2-step film [37, 39]. If the Co^{3+} has a high spin state, the Co is in a high-spin configuration: $e_g^2 t_{2g}^4$ and contains four unpaired electrons, which can strongly result in splitting of 3s core peaks. On the other hand, when it has a low-spin state, the Co is in a low-spin configuration: t_{2g}^6. The Co of low-spin state has no unpaired electron and does not show energy splitting for 3s core level. A full width at half maximum (FWHM) of the Co 3s main peak is 3.04 eV, supporting that there is no energy splitting [37]. The above HAXPES analysis for Co 3s core level demonstrates that cobalt in 2-step film exists in 3^+ of oxidation state.

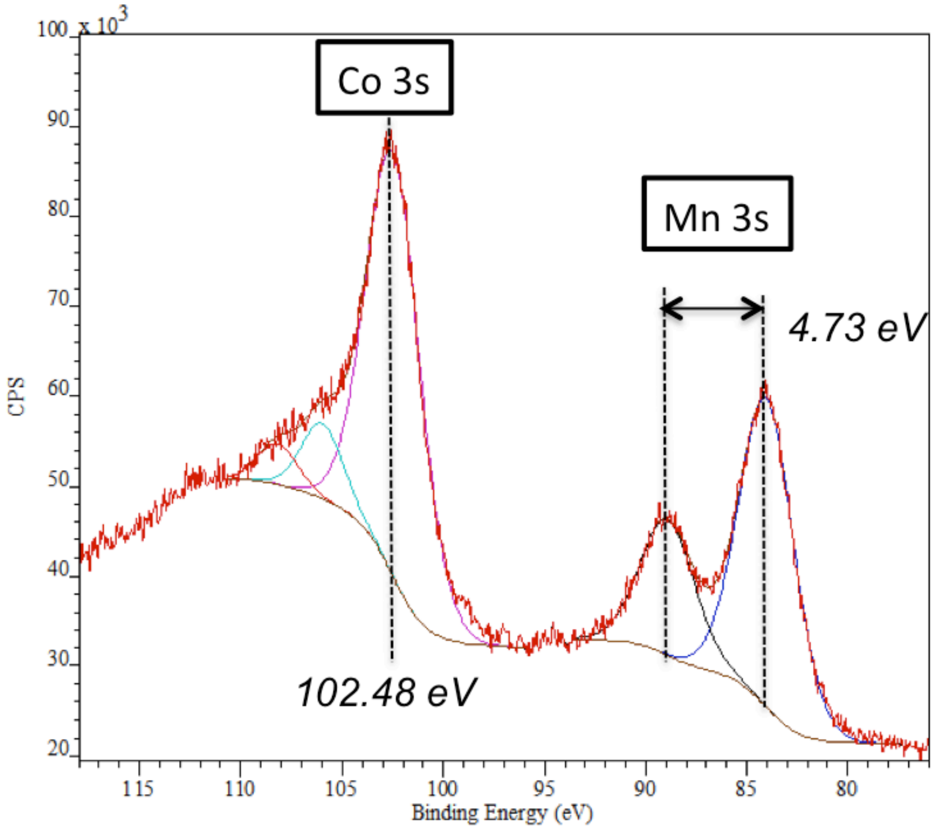

Figure 4.9 Co 3s and Mn 3s XPS core peaks of 2-step film.

4.2.3.4 Composition analysis of 2-step film

In order to identify any differences between 1-step and 2-step deposition, the 1-step film with same composition to that of the 2-step film is required. Therefore, the chemical composition of the 2-step film was first evaluated by ICP-MS. As shown in table 4.3, the Li:Co:Mn molar ratio for the 2-step film is determined to be 0.678:0.482:1. Based on the ICP-MS and STEM results, the chemical composition of the 2-step film can be described as $Li_{0.92}Co_{0.65}Mn_{1.35}O_4$. In addition, the oxidation states of cobalt and manganese, Co $^{3+}$ and Mn $^{3.8+}$, obtained from HAXPES results reveal that the 2-step film would has no oxygen deficient composition. Therefore, the 1-step film is deposited using a PLD target with the same composition of $Li_{0.92}Co_{0.65}Mn_{1.35}O_4$.

Table 4.3 Molar ratio and chemical composition for 2-step Li-Co-Mn-O thin film.

Sample	Li	Co	Mn	Chemical composition
2-step Li-Co-Mn-O	0.678	0.482	1	$Li_{0.92}Co_{0.65}Mn_{1.35}O_4$

4.2.4 Layer-by-layer deposition effects on structural properties

4.2.4.1 Orientations and symmetry of 1-step, 2-step and 4-step films

The detailed structural characteristics provided by the layer-by-layer deposition were investigated by XRD measurements. Figures 4.10(a) and 4.10(b) show out-of-plane and in-plane XRD patterns along the [1-10] substrate direction for the 1-step, 2-step, and 4-step Li-Co-Mn-O films, in addition to the $LiMn_2O_4$ epitaxial film. The pseudo cubic $SrRuO_3$ bottom layer is identified as having a (111) orientation based on the 222 diffraction peak at 85° in the out-of-plane patterns [31]. Peak indexing is carried out based on a cubic spinel structure with a space group of *Fd*-3*m* since the XRD patterns for the synthesized films show no significant differences to that for $LiMn_2O_4$, which is known to have this structure [6, 31]. No diffraction peaks that could not be indexed using this approach are found for any of the Li-Co-Mn-O films.

In the out-of-plane XRD patterns, the diffraction peaks are indexed as *hhh*, which indicates that all of the films have a (111) orientation. In the in-plane patterns, the peaks are indexed as *h*-*h*0, indicating a (1-10) orientation of the thin films along the [1-10] direction of the $SrTiO_3$ (111) substrate. The rotational symmetry of the crystal structure is confirmed by ϕ scans with a fixed $2\theta\chi$ value for the 4-40 diffraction peak, as shown in figure 4.10(c). For all of the films, six diffraction peaks are observed at intervals of 60°, indicating sixfold symmetry along the [111] direction. Thus, the XRD results reveal that all of the Li-Co-Mn-O films grow epitaxially on the $SrTiO_3$ (111) substrate.

The lattice parameter for the films is calculated using the 111, 222, 333, 444, 2-20 and 4-40 diffraction peaks. The 1-step, 2-step and 4-step films are found to have a lattice parameter of 8.191, 8.204 and 8.236 Å, respectively. The fact that the lattice parameter increases with the layer-by-layer deposition indicates that the layer-by-layer deposition causes an expansion of the lattice of the Li-Co-Mn-O spinel structure. One reason for the lattice expansion may be the presence of oxygen defects, which increase the ionic radius of the transition metals Co and Mn [40]. Another possibility is disordering between 8*a* and 16*d* sites. If transition metal atoms partially occupy Li 8*a* sites, and same number of Li atoms occupy transition-metal 16*d* sites, the lattice parameter can increase [41]. The lattice expansion could also be the result of a change in film composition. It is possible that evaporation of Li during the PLD process could generate the M_3O_4 (M = Co, Mn) spinel phase, which has a larger lattice constant. However, since the ICP-MS results reveal that the Li content in the 2-step film is almost the same as the stoichiometric value, the effect of composition changes can be ignored.

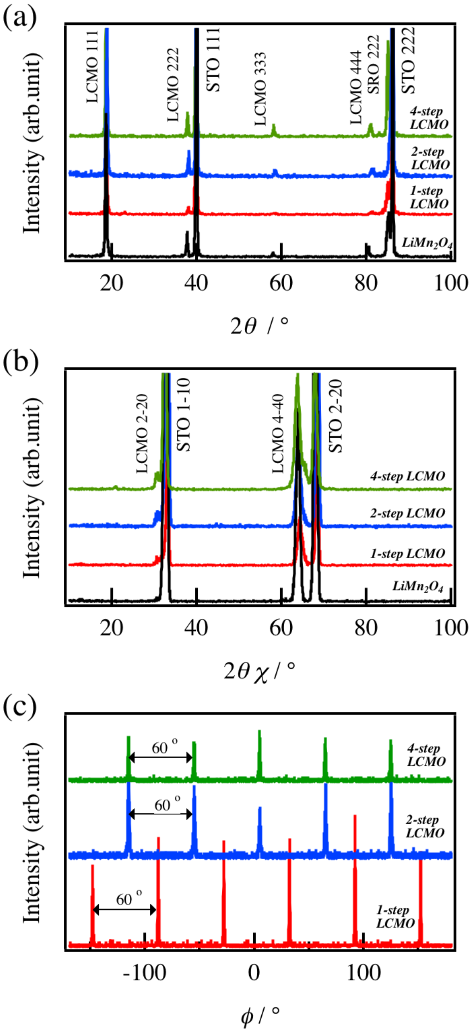

Figure 4.10 XRD patterns for 1-step, 2-step, 4-step $Li_{0.92}Co_{0.65}Mn_{1.35}O_4$ and $LiMn_2O_4$ films, (a) out-of-plane and (b) in-plane along the [1-10] direction of the $SrTiO_3$ (111) substrate. (c) ϕ scan XRD patterns for the 4-40 reflection for 1-step, 2-step and 4-step $Li_{0.92}Co_{0.65}Mn_{1.35}O_4$ films.

4.2.4.2 Thickness and density of 1-step and 2-step films

Based on the lattice parameters and the film composition, the theoretical density of the 1 step, 2 step and 4-step films is calculated to be 4.42, 4.40 and 4.35 g cm^{-3}, respectively. To verify these results, the film density is also evaluated by the XRR analysis results for the 1 step and 2-step films. Figures 4.11(a) and 4.11(b) show the observed XRR spectra and the fitted curves for the 1 step and 2-step films, respectively. The reflectivity spectra are plotted as a function of the scattering vector $Q_z = 4\pi\sin\theta/\lambda$, where λ is the wavelength (1.541 Å) and θ is the incident angle of the X-rays. The refined parameters for the thickness, density and roughness are summarized in table 4.4. The fitting process is performed using a value of 5.12 g cm^{-3} for the $SrTiO_3$ substrate density. The best fits are obtained using a four-layer model, involving a surface impurity layer, a Li-Co-Mn-O spinel layer, a $SrRuO_3$ layer, and a $SrTiO_3$ substrate. The surface impurity layer has a density of 2.11 g cm^{-3} and may be composed of Li_2CO_3 and/or LiOH produced by reaction with ambient air [33, 34]. The roughness of the interface between the $SrRuO_3$ and Li-Co-Mn-O spinel layers is very low, which is consistent with the fact the Li-Co-Mn-O spinel layer grows epitaxially. The thickness of the 1-step and 2-step films is determined to be 25.5 and 33.4 nm, respectively, and the density is 4.42 and 4.38 g cm^{-3}. These densities are consistent with those calculated based on the lattice parameters and compositions. It can therefore be concluded that the difference in density between the 1-step and 2-step films is due to the difference in lattice parameters rather than a difference in compositions. The XRR results also indicate that the surface roughness (R_a) for both films is less than 2 nm.

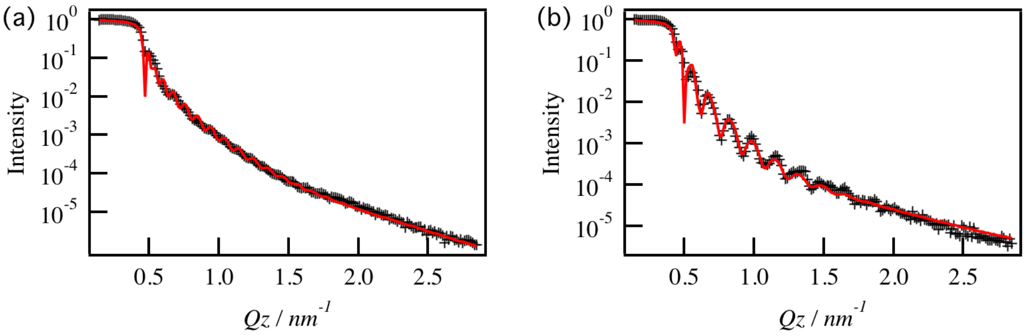

Figure 4.11 XRR spectra and fitting curves for (a) 1-step and (b) 2-step $Li_{0.92}Co_{0.65}Mn_{1.35}O_4$ films.

Table 4.4 XRR analysis results for different layers in (a) 1-step and (b) 2-step $Li_{0.92}Co_{0.65}Mn_{1.35}O_4$ thin films.

	Layer	Thickness l (nm)	Density ρ (g cm^{-3})	Roughness r (nm)
(a)	Impurity	1.3	2.11	1.2
	$Li_{0.92}Co_{0.65}Mn_{1.35}O_4$	25.5	4.42	0.5
	$SrRuO_3$	30.8	6.33	9.4
	$SrTiO_3$	-	5.12	1.6
(b)	Impurity	1.6	2.11	0.5
	$Li_{0.92}Co_{0.65}Mn_{1.35}O_4$	33.4	4.38	1.5
	$SrRuO_3$	36.0	6.50	1.6
	$SrTiO_3$	-	5.12	3.3

4.2.4.3 Relative intensity ratio analysis

To consider the effect of site disordering, the $I_{2\text{-}20}/I_{4\text{-}40}$ intensity ratio was evaluated for the 1-step, 2-step, 4-step Li-Co-Mn-O films and the $LiMn_2O_4$ thin film with almost no site disordering. This relative intensity ratio is a good indicator of the degree of site disordering because it is significantly sensitive to the location of atoms. Figure 4.12 shows the $I_{2\text{-}20}/I_{4\text{-}40}$

values determined from the XRD diffraction peaks for the thin films. Also shown is the theoretical value for an ideal $Li_{0.92}Co_{0.65}Mn_{1.35}O_4$ film as a function of the mixing rate for lithium and transition metal atoms, based on diffraction simulations performed using CrystalMaker (CrystalMaker Software Ltd.). The theoretical curve increases exponentially from 0 to 0.5 with increasing mixing rate. The determined intensity ratios for the $LiMn_2O_4$, 1-step, 2-step and 4-step films are 0.03, 0.10, 0.21 and 0.18, respectively. The value for the 1-step thin film is comparable to that for $LiMn_2O_4$, indicating a small amount of site disordering. On the other hand, for the 2-step and 4-step films, the ratios are about 0.2, corresponding to about 40% disordering. The most critical factor results in cation site disordering in a structure is generally known as heat energies, which increases potential energies of sites and moves the cations to form a mixing state for a stabilization of the sites. Since all the thin films were synthesized with a same temperature condition of 650 °C, the other component supporting to realize the site disordering is expected. Much site disordering for the 2-step and 4-step thin films are expected to be due to an interdiffusion among different crystal structures. The $LiCoO_2$ with layered rock salt structure is transformed into a spinel structure during the diffusion process. It is suppose that the force to stabilize the crystal structure stimulates the cation mixing and site disordering when a structure is transformed into a relatively stable structure. This result supports the idea that site disordering is responsible for the lattice expansion in the 2-step and 4-step films. Although it is still possible that the lattice expansion is also associated with oxygen defects, since the same PLD conditions are used for all films, particularly the temperature and oxygen partial pressure, it is unlikely that there is any significant difference among the films with regard to oxygen content.

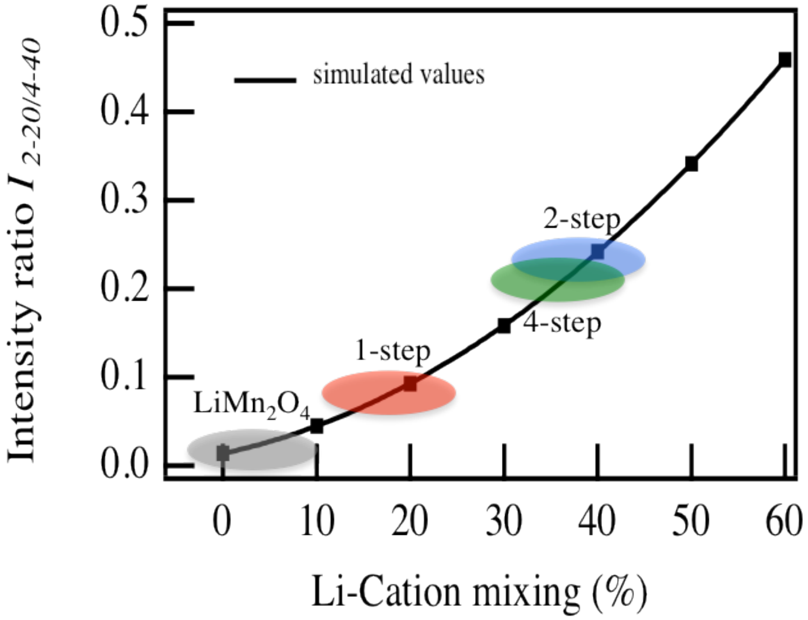

Figure 4.12 Intensity ratio $I_{2\text{-}20}/I_{4\text{-}40}$ for 1-step, 2-step, 4-step $Li_{0.92}Co_{0.65}Mn_{1.35}O_4$ and $LiMn_2O_4$ films. The solid curve shows the calculated intensity ratio as a function of the Li-cation mixing ratio.

4.2.4.4 Observation of site disordering for 2-step film

To obtain a direct evidence for site disordering, atomic image of the 2-step film was observed using HR-STEM. Figure 4.13(a) shows a cross-sectional HAADF STEM image of the 2-step film, observed along [1-10] direction of the $SrTiO_3$ substrate. The HAADF image shows a diamond shape configuration of transition metal atoms associated with the normal spinel structure (Figure 4.13(b)) with a space group of *Fd*-3*m*, in which Li, transition metal atoms and O are located at 8*a*, 16*d* and 32*e* site, respectively. However, bright spots are seen at the 8*a* site in the HAADF image, which is unexpected in ideal cubic spinel structure. The intensity (*I*) associated with a specific column in the HAADF image depends on the atomic number (Z) for the atoms located in that column, as $I \propto Z^{1.7}$ [42]. It means that light elements such as Li (Z=3) will be invisible when relatively heavy elements such as Co and Mn are simultaneously present in a structure [43]. Therefore, the bright spot at the 8*a* site is attributed to a transition metal atom from a 16*d* site, thus providing direct evidence for site disordering in the 2-step film. A larger amount of site disordering is observed in the 2-step film than could be achieved using conventional synthesis methods [7]. Such site disordering can be considered as a unique characteristic of layer-by-layer deposition.

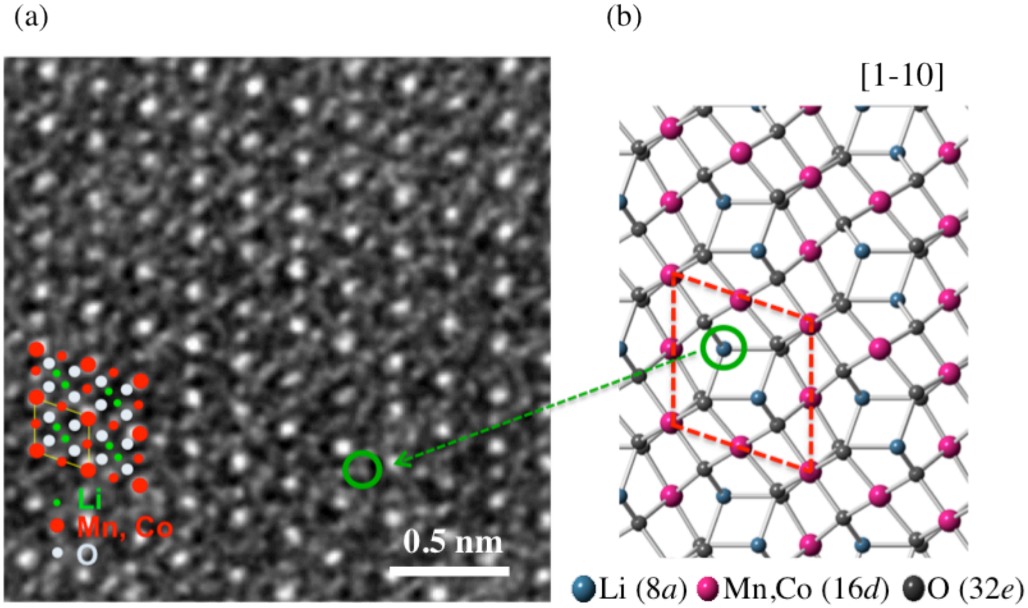

Figure 4.13 (a) HAADF image of 2-step $Li_{0.92}Co_{0.65}Mn_{1.35}O_4$ film, observed along [1-10] direction. (b) Schematic of atomic arrangement in conventional spinel structure viewed along [1-10] direction.

4.2.5 Layer-by-layer deposition effects on electrochemical properties

Electrochemical performances for the 2-step film electrode were examined and compared to that for the 1-step film synthesized using a conventional deposition method. Electrochemical reaction mechanism was evaluated using *in situ* XAFS measurement for the 2-step film electrode. Effects of the layer-by-layer deposition on electrochemical properties, cycle retention and rate capability, were investigated.

4.2.5.1 Charge-discharge measurement

Charge-discharge measurements are next carried out in order to examine the effect of site disordering on battery performances. To extend a comprehension for electreochemical reaction of the spinel type Li-Co-Mn-O and to confirm effects of the novel structural property on electrochemical properties apparently, the charge-discharge measurements were performed in the voltage range from 1.6 to 4.5 V where conventional electrode materials with spinel structure show very unstable structural properties.

Figures 4.14(a) and 4.14(b) show charge-discharge curves for the 1 step and 2-step films, respectively. The charge-discharge capacities were determined based on the amount of material present, which is calculated from the film area (0.7 mm^2), density (4.42 g cm^{-3} for 1-step film, 4.38 g cm^{-3} for 2-step film) and thickness (25.5 nm for 1-step film, 33.4 nm for 2-step film). Both films electrodes show comparable discharge capacities of 324 and 340 mAh g^{-1} at the second cycle. Specific capacities of both films electrodes can be obtained by subtracting about 30 mAh g^{-1} of capacity of $SrRuO_3$ layer. The specific capacities are calculated to be 294 and 310 mAh g^{-1} for the 1-step and 2-step films electrodes, respectively, which indicates about 2 mol of Li are (de)intercalated. In addition, the charge-discharge curves have a similar shape for both films, indicating those have a similar reaction mechanism. As considering an electrochemical reaction of the conventional cubic spinel structure, a redox couple observed at about 3.9 V during charge and discharge process is expected to a redox of $Mn^{3+/4+}$ in cubic structure [44]. Further, reaction plateaus detected at 2.9 V during charge process and at 2.6 V during discharge process are known as a redox of $Mn^{3+/4+}$, involving a phase transition between cubic and tetragonal structure [45]. However, reactions detected at 3.7 V during charge process and at 2.0 V during discharge process are unknown although those show about 100 mAh g^{-1} of large capacity. A research is required to reveal a reaction mechanism of the Li-Co-Mn-O film electrode.

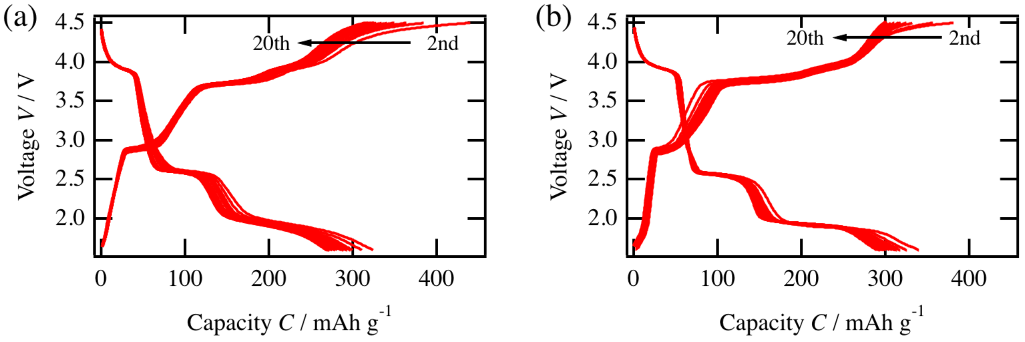

Figure 4.14 Charge-discharge curves for (a) 1-step and (b) 2-step $Li_{0.92}Co_{0.65}Mn_{1.35}O_4$ thin-film electrodes.

4.2.5.2 Analysis of reaction mechanism for 2-step film electrode

The electronic structure change of the 2-step film was investigated by XAS measurements to confirm the reaction mechanism. The Mn and Co K-edge spectra were obtained in fluorescence mode using a germanium 19-elements solid state detector (Ge SSD) installed on the hard X-ray bending magnet beamline BL14B2 at Spring-8. XANES data were collected under 4° of incident angle by using θ - 2θ stage equipped on the beamline to examine electronic structure in the thin film electrode bulk [28]. The cell voltage was raised up from the open circuit voltage to 4.5 V then decreased to 1.6 V. Once the cell voltage reaches to a destination voltage, the voltage was maintained for 0.5 hours to release an over-potential, which is exhibited in the *in situ* electrochemical cell, before the XANES measurements.

Above all, the electronic structure of as-prepared 2-step film was examined to identify an initial state. Figures 4.15(a) and 4.15(b) show Co and Mn K-edge XANES spectra of the 2-step thin film. The absorption edge E_0, where μ becomes 0.5, for Co is identical to that for $LiCoO_2$, indicating that the 2-step film contains Co^{3+}. On the other hand, E_0 for Mn is located between the values for $LiMn_2O_4$ and Li_2MnO_3. Therefore, the oxidation state for Mn is expected to be between 3.5^+ and 4^+. This result is in good agreement with the average Mn oxidation state of 3.8^+ estimated based on the HAXPES results and chemical composition $Li_{0.92}Co_{0.65}Mn_{1.35}O_4$. As a result, the chemical composition of the 2-step film is calculated to be $Li_{0.92}Co^{3+}{}_{0.65}Mn^{3+}{}_{0.27}Mn^{4+}{}_{1.08}O_4$. This agreement also provides evidence that oxygen defects do not have a substantial effect on the structural characteristics of the film.

The electrochemical reaction mechanism of the 2-step film was investigated by *in situ* XANES measurement. The measurements were performed at 4.5 V during charge process and 1.6 V during discharge process. Figures 4.15(c) and 4.15(d) show Co and Mn K-edge XANES spectra for first cycle of charge-discharge process. Figure 4.15(e) displays dQ/dV curves of 2-step film for first cycle. The Co XANES spectrum measured at 4.5 V shows that there is no spectrum shift in comparison with that of $LiCoO_2$, indicating Co does not participate in electrochemical reaction during the first charge process. On the other hand, the Mn spectrum moved toward higher energy, which is illustrating the reaction at 4.0 V involving $Mn^{3+/4+}$ redox in cubic structure. At 1.6 V during first discharge process, both Mn and Co XANES spectra shifted toward lower threshold energies than those of as-prepared $LiMn_2O_4$ and $LiCoO_2$, respectively. The change reflects that both Mn and Co are reduced and those oxidation states are approaching to about 3^+ and 2^+, respectively. The reduction of $Mn^{4+/3+}$ is attributed to the electrochemical reaction at 2.6 V, which accompanies the phase transition from cubic to tetragonal structure. At last, the plateau at 1.8 V is revealed as electrochemical reduction process of Co; the oxidation state is varied from 3^+ to 2^+. The Co redox showed the very large polarization. The large polarization characteristic of $Co^{2+/3+}$ redox was also confirmed in powder Li-Co-Mn-O and 1-step Li-Co-Mn-O film, indicating the phenomenon is not attributed to thin film characteristics or site disordering structure. These results indicate the $Co^{2+/3+}$ redox is slow reaction in kinetics. One possible reason for the slow reaction can be suggested with variation of spin states of Co ions during redox process. It is well reported that Co^{3+} and Co^{2+} respective show low spin and high spin states. Therefore, spin states of Co should be changed during the redox process. It is considered that the Co passes intermediate states when the spin states are changed between low and high spin states. As a result, the variation of spin states increases the activation energy and results in large polarization. The *in situ* XANES results confirm that the electrochemical reactions of 2-step film electrodes are contributed by not only Mn but also Co.

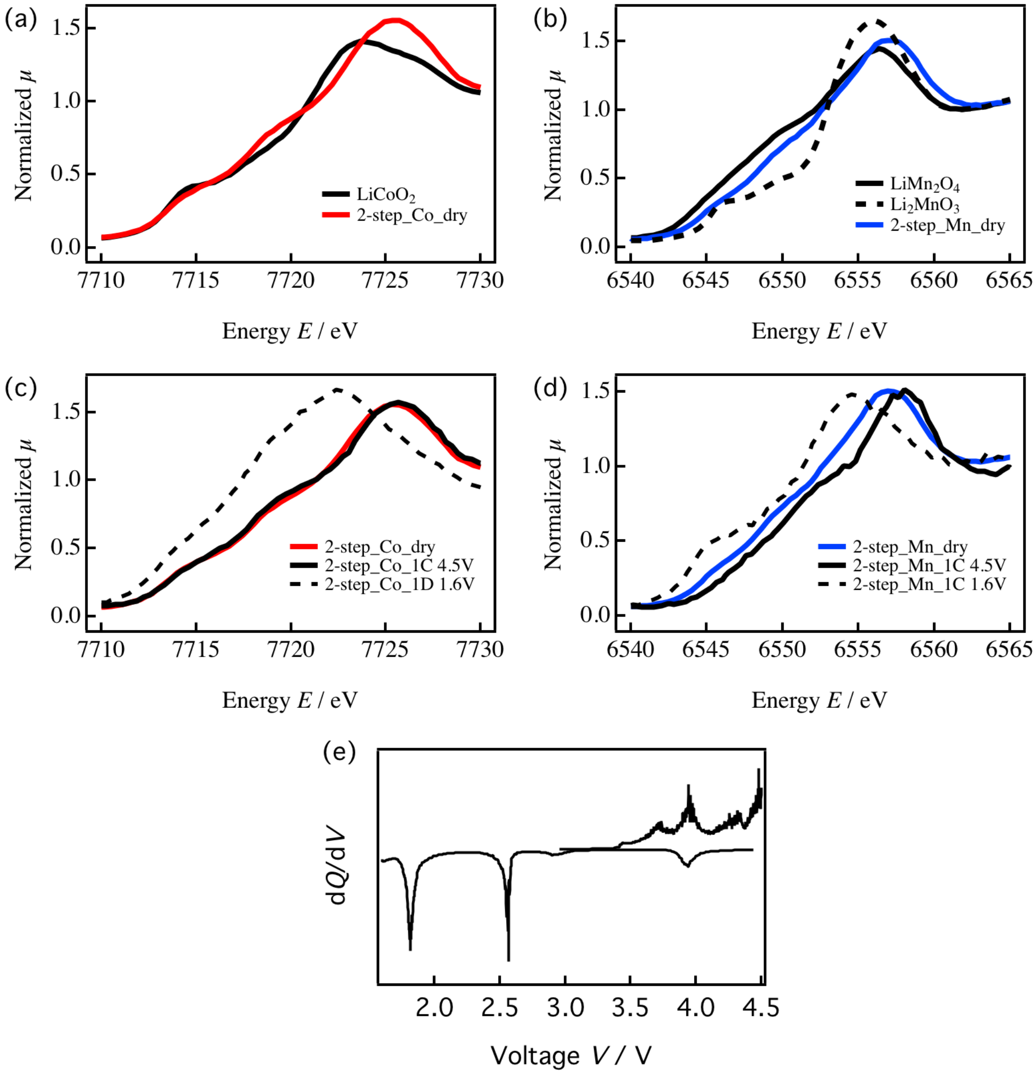

Figure 4.15 K-edge XANES spectra of (a) Co and (b) Mn for as-prepared 2-step film. XANES spectra change of (c) Co and (d) Mn for 2-step film during first cycle of charge-discharge process. (e) dQ/dV curve of first cycle for 2-step film.

4.2.5.3 Cycle retention and rate capability

Figure 4.16(a) illustrates normalized discharge capacities of the thin film electrodes as function of cycle number during 20 cycles. The discharge capacity of the 2-step thin film was maintained for 80 % after 20 cycles while the 1-step thin film showed capacity degradation to 68 %. This indicates the 2-step thin film has higher reversibility of charge discharge reactions than that of the 1-step thin film. Figure 4.16(b) displays rate capability of the 1-step and 2-step thin film electrodes. The thin film electrodes showed relatively larger degradation at initial few cycles in cycle test (figure 4.16(a)). After the 5th cycle, the degradation was moderated both in 1-step and 2-step film electrodes. Therefore, to remove the cycle dependence from *C*-rate test, we measured 5 cycles for each *C*-rate test and the capacities of final cycle for each *C*-rate were plotted to investigate the rate capability. That is, all the rate capability results were obtained after 5 cycles of charge-discharge measurement. The discharge capacity of the 1-step thin film electrode decreased significantly according to the increase of *C*-rate; only 60 % of discharge capacity was maintained at 10 *C*-rate. On the other hand, the 2-step thin film showed gradual decrease of the capacity with increase of *C*-rate and 79 % of discharge capacity was still maintained at 10 *C*-rate. Taking into account the difference of the film thickness, the 1-step thin film could expect to show higher rate capability; the thickness of the 1-step thin film is thinner than that of the 2-step thin film thus nano-effect on rate property is implied. Several times of charge-discharge tests to confirm the reproducibility showed that the 2-step film electrode has obviously higher *C*-rate and cycle retention properties than those of 1-step film. Although the cycle retention test for the 1-step film is performed one time, it could be concluded the higher cycle retention properties of the 2-step film electrode by taking into account error bars of the 2-step film electrode.

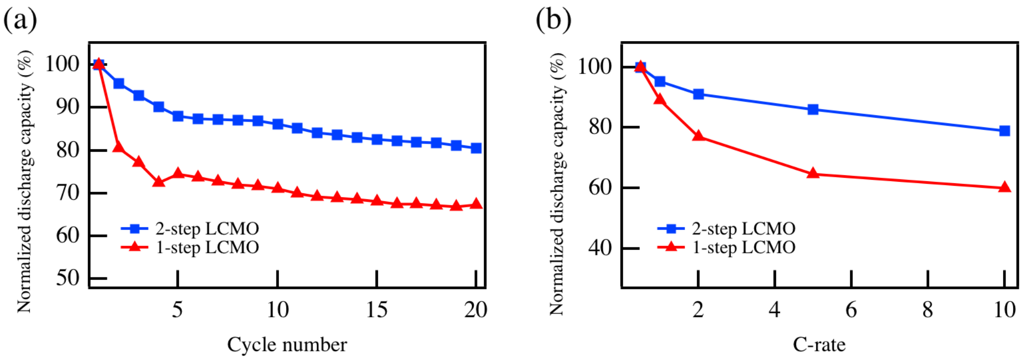

Figure 4.16 (a) Cycle retention curves and (b) rate properties for discharge of 1-step and 2-step electrodes.

4.2.6 Discussion on effect of layer-by-layer deposition

The cycle retention and rate capability measurements demonstrate that the 2-step film electrode, synthesized by layer-by-layer deposition process, has unexpected excellent electrochemical properties. The effects of layer-by-layer deposition on the electrochemical properties were discussed. It is confirmed the 2-step film has unique structural properties, the extended lattice parameter and site disordering. The relation between the unique structural properties and electrochemical performances was investigated.

Recently, it has been reported that when $LiMn_2O_4$ is undergoing electrochemical reactions, a Mn_3O_4 phase is formed on its surface in the fully delithiated state, which leads to structural degradation at the surface [1]. This surface phase transition is related to oxygen desorption from the surface, which accompanies Mn migration from 16*d* to 8*a* sites. However, in the 2-step film in the present study, transition metal atoms already occupy 8*a* sites and form a stable framework. Therefore, site disordering could prevent cation migration and oxygen desorption.

The excellent rate capability is induced by the larger lattice parameter. The larger lattice parameter for the 2-step film could expand the bottleneck size for Li diffusion in the spinel structure, leading to a superior rate capability. The expanded lattice parameter in the 2-step film could be explained with crystal field stabilization energy (CFSE). Most transition metals prefer to form octahedral or distorted octahedral coordination due to their large CFSE in octahedral sites. However, the site disordering of 2-step film contains the transition metal in tetrahedral site, inducing a low CFSE and unstable structure. Therefore, the unstable energy would be released by increasing the bond length between a transition metal and oxygen, leading a lattice expansion.

4.3 Conclusion

A novel Li-Co-Mn-O epitaxial thin-film (2-step film) electrode was synthesized on a $SrTiO_3$ single-crystal substrate by sequential PLD of $LiMn_2O_4$ and $LiCoO_2$ layers with different crystal structures. The film had a uniform chemical composition of $Li_{0.92}Co_{0.65}Mn_{1.35}O_4$ and a cubic spinel structure. The lattice parameter for the 2-step film was larger than that for a 1-step thin film directly deposited using the $Li_{0.92}Co_{0.65}Mn_{1.35}O_4$ target. In addition, the 2-step film exhibited considerable site disordering, in that there was a significant exchange of Li and transition metal atom sites, which does not occur in films produced using conventional synthesis methods. These unique structural properties led to greatly enhanced electrochemical characteristics such as high cycle and rate capabilities. The proposed layer-by-layer deposition method is therefore highly promising for developing lithium battery electrode materials with excellent electrochemical performance.

References

[1] D. Tang, Y. Sun, Z. Yang, L. Ben, L. Gu, X. Huang, Chem Mater, 26 (2014) 3535-3543.

[2] B.C. Melot, J.M. Tarascon, Accounts of chemical research, 46 (2013) 1226-1238.

[3] J.B. Goodenough, Accounts of chemical research, 46 (2013) 1053-1061.

[4] R. Koksbang, J. Barker, H. Shi, M.Y. Saidi, Solid State Ionics, 84 (1996) 1-21.

[5] J.M. Tarascon, M. Armand, Nature, 414 (2001) 359-367.

[6] M. Hirayama, H. Ido, K. Kim, W. Cho, K. Tamura, J. Mizuki, R. Kanno, J Am Chem Soc, 132 (2010) 15268-15276.

[7] H. Shigemura, M. Tabuchi, H. Kobayashi, H. Sakaebe, A. Hirano, H. Kageyama, J Mater Chem, 12 (2002) 1882-1891.

[8] K. Sakamoto, M. Hirayama, H. Konishi, N. Sonoyama, N. Dupre, D. Guyomard, K. Tamura, J. Mizuki, R. Kanno, Phys Chem Chem Phys, 12 (2010) 3815-3823.

[9] K. Kubota, T. Kaneko, M. Hirayama, M. Yonemura, Y. Imanari, K. Nakane, R. Kanno, J Power Sources, 216 (2012) 249-255.

[10] K.F. Chiu, H.C. Lin, K.M. Lin, C.C. Chen, J Electrochem Soc, 153 (2006) A1992-A1997.

[11] S. Shiraki, H. Oki, Y. Takagi, T. Suzuki, A. Kumatani, R. Shimizu, M. Haruta, T. Ohsawa, Y. Sato, Y. Ikuhara, T. Hitosugi, J Power Sources, 267 (2014) 881-887.

[12] H.W. Chan, J.G. Duh, S.R. Sheen, J Power Sources, 115 (2003) 110-118.

[13] M. Okubo, E. Hosono, J. Kim, M. Enomoto, N. Kojima, T. Kudo, H.S. Zhou, I. Honma, J Am Chem Soc, 129 (2007) 7444-7452.

[14] M. Jo, Y.S. Hong, J. Choo, J. Cho, J Electrochem Soc, 156 (2009) A430-A434.

[15] M. Okubo, Y. Mizuno, H. Yamada, J. Kim, E. Hosono, H.S. Zhou, T. Kudo, I. Honma, Acs Nano, 4 (2010) 741-752.

[16] A. Caballero, L. Hernan, J. Morales, E.R. Castellon, J. Santos, J Power Sources, 128 (2004) 286-291.

[17] R. Mishra, Y.M. Kim, J. Salafranca, S.K. Kim, S.H. Chang, A. Bhattacharya, D.D. Fong, S.J. Pennycook, S.T. Pantelides, A.Y. Borisevich, Nano letters, 14 (2014) 2694-2701.

[18] B.B. Chen, P.F. Chen, H.R. Xu, X.L. Tan, F. Jin, Z. Guo, B.W. Zhi, W.B. Wu, Appl Phys Lett, 104 (2014).

[19] N. Sata, K. Eberman, K. Eberl, J. Maier, Nature, 408 (2000) 946-949.

[20] R.V.K. Mangalam, J. Karthik, A.R. Damodaran, J.C. Agar, L.W. Martin, Adv Mater, 25 (2013) 1761-1767.

[21] S. Das, A. Herklotz, E.J. Guo, K. Dorr, J Appl Phys, 115 (2014).

[22] A. Gupta, Curr Opin Solid St M, 2 (1997) 23-31.

[23] D.P. Norton, D.H. Lowndes, J.D. Budai, B.C. Chakoumakos, Mat Sci Eng B-Solid, 41 (1996) 374-378.

[24] B. Mercey, P.A. Salvador, W. Prellier, T.D. Doan, J. Wolfman, J.F. Hamet, M. Hervieu, B. Raveau, J Mater Chem, 9 (1999) 233-242.

[25] C. Bhardwaj, B.S.S. Daniel, D. Kaur, Mater Lett, 87 (2012) 172-175.

[26] M. Hirayama, N. Sonoyama, M. Ito, M. Minoura, D. Mori, A. Yamada, K. Tamura, J. Mizuki, R. Kanno, J Electrochem Soc, 154 (2007) A1065-A1072.

[27] K. Kim, T. Toujigamori, K. Suzuki, S. Taminato, K. Tamura, J. Mizuki, rsquo, ichiro, M. Hirayama, R. Kanno, Electrochemistry, 80 (2012) 800-803.

[28] Y. Zheng, S. Taminato, Y. Xu, K. Suzuki, K. Kim, M. Hirayama, R. Kanno, J Power Sources, 208 (2012) 447-451.

[29] C.R. Brown, E. McCalla, J.R. Dahn, Solid State Ionics, 253 (2013) 234-238.

[30] A. Ito, H. Masumoto, T. Goto, S. Sato, J Eur Ceram Soc, 30 (2010) 435-440.

[31] K. Suzuki, K. Kim, S. Taminato, M. Hirayama, R. Kanno, J Power Sources, 226 (2013) 340-345.

[32] A. Karim, S. Fosse, K.A. Persson, Phys Rev B, 87 (2013).

[33] M. Hirayama, K. Sakamoto, T. Hiraide, D. Mori, A. Yamada, R. Kanno, N. Sonoyama, K. Tamura, J. Mizuki, Electrochim Acta, 53 (2007) 871-881.

[34] M. Hirayama, N. Sonoyama, T. Abe, M. Minoura, M. Ito, D. Mori, A. Yamada, R. Kanno, T. Terashima, M. Takano, K. Tamura, J.i. Mizuki, J Power Sources, 168 (2007) 493-500.

[35] M. Hirayama, M. Yonemura, K. Suzuki, N. Torikai, H. Smith, E. Watkinsand, J. Majewski, R. Kanno, Electrochemistry, 78 (2010) 413-415.

[36] D. Kosemura, M. Takei, K. Nagata, H. Akamatsu, M. Hattori, D. Katayama, T. Nishita, Y. Hirota, M. Machida, J.Y. Son, T. Koganezawa, I. Hirosawa, A. Ogura, Jpn J Appl Phys, 49 (2010).

[37] L. Daheron, R. Dedryvere, H. Martinez, M. Menetrier, C. Denage, C. Delmas, D. Gonbeau, Chem Mater, 20 (2008) 583-590.

[38] H. Xia, Y.H. Wan, F. Yan, L. Lu, Mater Chem Phys, 143 (2014) 720-727.

[39] R. Dedryvere, S. Laruelle, S. Grugeon, P. Poizot, D. Gonbeau, J.M. Tarascon, Chem Mater, 16 (2004) 1056-1061.

[40] M. Yonemura, T. Kamiyama, Y. Kawamoto, R. Kanno, Mater Trans, 45 (2004) 2048-2055.

[41] F. Meducin, S.A.T. Redfern, Y. Le Godec, H.J. Stone, M.G. Tucker, M.T. Dove, W.G. Marshall, Am Mineral, 89 (2004) 981-986.

[42] D.E. Jesson, S.J. Pennycook, P Roy Soc Lond a Mat, 441 (1993) 261-281.

[43] S.Y. Chung, S.Y. Choi, T. Yamamoto, Y. Ikuhara, Angew Chem Int Edit, 48 (2009) 543-546.

[44] M.Y. Saidi, J. Barker, R. Koksbang, Electrochim Acta, 41 (1996) 199-204.

[45] R. Koksbang, J. Barker, M.Y. Saidi, K. West, B. ZachauChristiansen, S. Skaarup, Solid State Ionics, 83 (1996) 151-157.

Chapter 5: Summary

Electrochemical performance of lithium battery is strongly dependent on crystal structures and compositions of the electrode materials. To develop noble electrodes of new structures and compositions with enhanced electrochemical properties are very crucial. Although there have been a lot of conventional studies to develop the electrode materials, those methods provide limited phases, structures and compositions. A new synthesis technique is required to obtain noble electrodes. A new materials synthesis approach, layer-by-layer process, using pulsed laser deposition provides new structures and compositions such as super-lattice, gradation and metastable structure. In particular, the new structures show noble properties unexpected from structures synthesized by the conventional methods. The most critical point is that a variety kind of structures and compositions are designed by stacking conventional electrode materials with various deposition ways. Further, it is expected as a noble method to directly obtain a desired structure.

This thesis contains a synthesis process of the new epitaxial thin film electrode material using layer-by-layer deposition and an investigation for its structural and electrochemical properties. The results in present study are summarized as follow;

In chapter 3, effects of $SrTiO_3$ substrate, $SrRuO_3$ and gold current collector on battery performances were examined to analyze specific capacities and reactions of epitaxial thin film electrodes. Epitaxial thin films, are used in the layer-by-layer deposition process, could show nano scale effects on capacities. Nano scale effects on various electrode materials have been investigated but the effects of substrates and current collectors have not been researched. A main phenomena dominating reactions of the $SrTiO_3$ substrate and $SrRuO_3$ current collector was investigated by cyclic voltammetry in a range between 1.6 and 4.5 V. Capacitive contributions of the substrate and current collector to battery capacities were also confirmed by charge-discharge measurements. Four kind of samples, $SrTiO_3$ substrate, $SrTiO_3$ substrate with gold deposition, $SrRuO_3$ / $SrTiO_3$ and $LiCoO_2$ / $SrRuO_3$ / $SrTiO_3$ were prepared. Cyclic voltammetry measurement revealed that the $SrTiO_3$ substrate is mainly influenced by surface-controlled reaction. When the gold current collector is deposited on the back and lateral side of the $SrTiO_3$ substrate, the electrochemical reactions were stimulated. However, the charge-discharge measurement demonstrated that capacitive contributions of the substrates were insignificant. A $SrRuO_3$ layer played a bridge role between a semiconducting substrate and electrode. In addition, the deposition of $SrRuO_3$ layer restrained the surface reaction of substrates. However, the $SrRuO_3$ it self showed reaction system dominated by bulk diffusion at entire voltage range. Especially, a considerable capacity of 30 mAh g^{-1} was identified under 3.0 V. The capacity contribution of $SrRuO_3$ should be considered when a charge-discharge measurement is performed at below 3.0 V for an electrode where the $SrRuO_3$ is introduced as buffer layer.

In chapter 4, a new electrode material was developed with the layer-by-layer deposition process and its structural and electrochemical properties were examined. A novel Li-Co-Mn-O epitaxial thin-film electrode (2-step film) was synthesized on the $SrTiO_3$ single-crystal substrate by the deposition of $LiCoO_2$: space group *R-3m* and $LiMn_2O_4$: space group *Fd-3m*. Although two materials with different structures were deposited in sequence, the synthesized film had a uniform chemical composition of $Li_{0.92}Co_{0.65}Mn_{1.35}O_4$ and a cubic spinel structure. The 2-step film showed larger lattice parameter than that of a 1-step film directly synthesized using a $Li_{0.92}Co_{0.65}Mn_{1.35}O_4$ target. HR-STEM observation indicated the 2-step film has a unique structure of considerable site disordering that Li (8*a*) and transition-metal (16*d*) sites are significantly exchanged. The unique structure could not be obtained from conventional synthesis methods. Charge-discharge measurement showed the 2-step and 1-step films electrodes have a similar reaction mechanism with comparable capacities of 310 and 294 mAh g^{-1}, respectively. *In situ* XANES measurement indicated both Mn and Co are involved in electrochemical reactions for the 2-step film in a range from 1.6 and 4.5 V. In particular, a $Co^{2+/3+}$ redox couple was observed at 3.7 V during charge process and at 1.8 V during discharge process, which has not been reported ever in Li-Co-Mn-O systems. Cycle retention tests illustrated that the discharge capacity of the 2-step film was kept for 80 % after 20 cycles while the 1-step film showed 68 % of remaining discharge capacity. Rate capability tests showed only 60 % of discharge capacity was maintained at 10 C-rate for the 1-step film while the 2-step film showed 79 % of discharge capacity was maintained at 10 C-rate. The electrochemical tests revealed the 2-step film has higher reversibility of reactions with better rate capability. These greatly enhanced electrochemical characteristics were induced by the unique structural properties of the site disordering and extended lattice parameter.

The layer-by-layer deposition process is a new synthesis concept that has never been applied for lithium battery field. This approach provided the new structure with excellent electrochemical characteristics that could not be obtained from conventional methods. The relation between the unique structural properties and the enhanced electrochemical properties are discussed. The proposed layer-by-layer deposition method can provide an expanded range of compositional and structural variations for lithium battery electrode materials.